Sensitivity enhanced methods for solid state NMR

Deni Mance

Sensitivity enhanced methods for solid state NMR

Gevoeligheid verhogende methoden voor vaste stof NMR

(met een samenvatting in het Nederlands)

PROEFSCHRIFT

ter verkrijging van de graad van doctor aan de Universiteit Utrecht op gezag van de rector magnificus, prof. dr. G.J. van der Zwaan, ingevolge het besluit van het college voor promoties in het openbaar te verdedigen op woensdag 28 juni 2017 des middags te 12.45 uur

door

Deni Mance

geboren op 17 december 1986 te Rotterdam

PROMOTOR:

Prof. dr. M. Baldus

CONTENTS

CHAPTER 1

General Introduction

Nuclear Magnetic Resonance (NMR)

What makes Nuclear Magnetic Resonance (NMR) spectroscopy such an interesting tool is that most nuclei possess a property called spin. These spins have a magnetic moment and when they are placed in an external applied magnetic field, they will start to precess around the axis of the applied magnetic field. The precession of spins is referred to as resonance frequency and is specific for each type of nucleus[1]. Early NMR experiments were done on paraffin and water from which ^{1}H signals could be detected[2,3]. These first experiments showed that not only was it possible to identify the type of nucleus present based on the resonance frequency but that the NMR signal could also be used to infer the chemical environment of this nucleus. However, these experiments suffered from low sensitivity which is a typical limitation of the NMR technique. Nonetheless with the development of higher magnetic fields and new methods enhancing the polarization it is possible to overcome this limitation.

Sensitivity in NMR

A vast number of nuclei possess a property called spin (I), where I can take values of 0, 1/2, 1, 3/2, 2, etc. A nucleus with spin I can have 2I+1 energy states in a magnetic field, allowing the magnetic spin quantum number (m) to take on values between: -I, -(I+1), .., (I-1), I. The splitting in different energy states is referred to as the Zeeman interaction and is caused by an externally applied magnetic field. The Zeeman interaction is given by eq. 1.1.

$$\Delta E = -\mu * B_0 \qquad (1.1)$$

Where ΔE is the energy difference between the states, μ is the magnetic moment of the atom and B_0 the externally applied magnetic field. The energy of an individual states (E_m) can by calculated by equation (1.2) that depends on the gyromagnetic ratio (γ), the applied magnetic field (B_0) and where h is the Planck's constant.

$$E_m = -\gamma m \frac{h}{2\pi} B_0 \qquad (1.2)$$

The nuclear spins would precess with a frequency around the magnetic field which is called the Larmor frequency (1.3).

$$\omega_0 = 2\pi * \Delta E/h \tag{1.3}$$

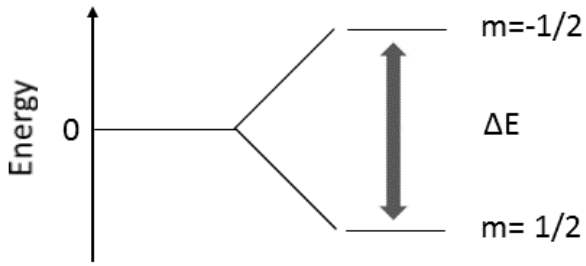

Figure 1.1. Zeeman energy levels for a spin=1/2 nucleus in and externally applied magnetic field

In the case of spin I=1/2 in an externally applied magnetic field, there would be 2 energy levels as shown in Figure 1.1. In a typical NMR experiment an ensemble of spins needs to be considered of which each spin can either align with or against the applied magnetic field and would thus occupy one of these 2 states. Each state can be populated (n_1 and n_2) to a different degree therefore causing the ensemble of spins to have a polarization (p) that is given by the Boltzmann equation:

$$\frac{n_1}{n_2} = \exp\left(\frac{-\Delta E}{kT}\right),\ p = \frac{n_1 - n_2}{n_1 + n_2} = tanh\left(\frac{h\gamma B_0}{2kT}\right) \tag{1.4}$$

The population difference between these states gives a net magnetization. The net magnetization determines the signal intensity and is orientated along the magnetic field. Assuming the case of having in total $1*10^6$ spins in a magnetic field of 9.4 Tesla at 298 K, the net magnetization would only be generated by 32 spins and would thus dictate the sensitivity. This is the reason why in NMR sensitivity is of critical relevance. The sensitivity can be increased for a certain nucleus by increasing the magnetic field strength or by decreasing the temperature. In the most general form the sensitivity can be calculated from equation (1.5). This equation shows that the signal to noise ratio S/N depends on various parameters such as the gyromagnetic ratio (γ), the externally applied magnetic field (B_0), the number of scans (n), the transverse relaxation time T_2 and the temperature (T).

$$\frac{S}{N} \approx \gamma^{5/2} B_0^{3/2} \sqrt{n} \cdot T_2 \cdot \frac{1}{T} \tag{1.5}$$

Note that some factors can be difficult to change such as going to higher field or changing sample temperature if the sample is temperature sensitive. Certain other parameters such as the nuclei to be detected (γ) can be easier to change in order to increase the sensitivity. Such a strategy will be shown in **chapter 2** using ^{1}H-detection instead of the generally applied ^{13}C-detection in ssNMR on proteins.

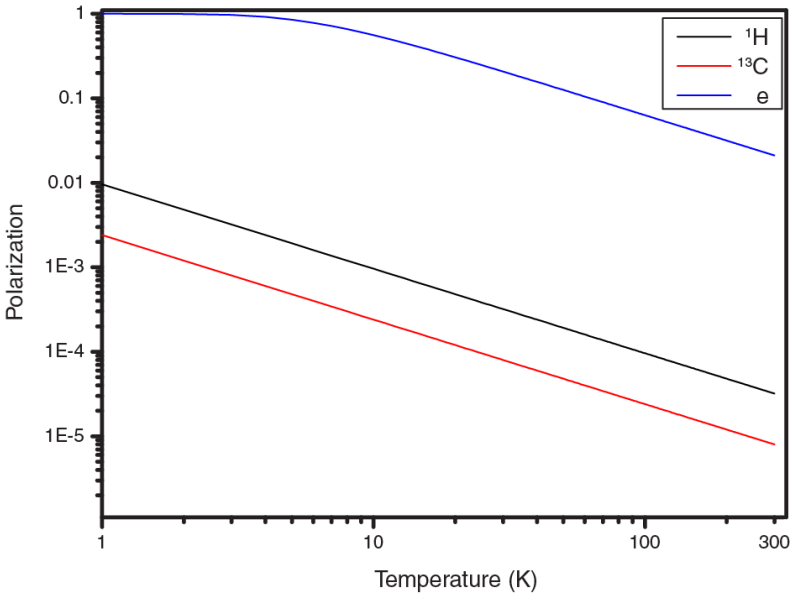

Figure 1.2. Temperature dependent Polarization at 9.4T for different spins: Hydrogen (^{1}H), Carbon (^{13}C) and electron (e).

In Figure 1.2 the polarization (as defined in eq. 1.4) is shown at different temperatures for different types of spins. Note that the ratio of polarization between the ^{1}H and ^{13}C spins is approximately a factor 4. The polarization difference can be exploited in the context of cross-polarization as introduced by Pines et al. [4], for example, in order to transfer the polarization from ^{1}H to ^{13}C and thereby increase the sensitivity of ^{13}C NMR spectroscopy. As is visible from Figure 1.2, the polarization of an electron is far larger (658 times larger) than that of a ^{1}H and can be transferred by Dynamic Nuclear Polarization (DNP) discussed further below.

Nuclear spin interactions in NMR

In NMR, there are various types of interactions between spins allowing information to be obtained about the chemical environment of the observed nuclei. The strength of these interactions may vary depending on the phase of the sample such as in solution or solid, but it may also be influenced by the atomic structure and dynamics. In general, the strongest interaction present is the Zeeman-interaction, shown above.

As a general example, we can define a Hamiltonian containing all interactions present (H_{total}), shown in equation (1.6). Usually these interactions are expressed as a tensor containing an isotropic and anisotropic component and they can be approximated as a combination of a rank 0, rank 1 and rank 2 tensors shown below in equation (1.7).

$$H_{total} = \begin{pmatrix} H_{xx} & H_{xy} & H_{xz} \\ H_{yx} & H_{yy} & H_{yz} \\ H_{zx} & H_{zy} & H_{zz} \end{pmatrix} \tag{1.6}$$

$$H_{total} \cong H_{iso}\begin{pmatrix} 1 & 0 & 0 \\ 0 & 1 & 0 \\ 0 & 0 & 1 \end{pmatrix} + \begin{pmatrix} 0 & h_{xy} & h_{xz} \\ -h_{yx} & 0 & h_{yz} \\ -h_{zx} & -h_{zy} & 0 \end{pmatrix} + \begin{pmatrix} \delta_{xx} & \delta_{xy} & \delta_{xz} \\ \delta_{yx} & \delta_{yy} & \delta_{yz} \\ \delta_{zx} & \delta_{zy} & \delta_{zz} \end{pmatrix} \tag{1.7}$$

The first matrix is the rank 0 tensor containing isotropic elements and is essentially the only matrix that determines the observed NMR spectrum in liquids. The second matrix is the rank 1 tensor and usually doesn't contribute to the NMR spectrum. The last matrix is the rank 2 tensor and is especially important for solids as it defines the anisotropic interactions (and are thus orientation dependent). In Table 1.1, the Hamiltonians of the interactions generally present in a solid-state NMR experiment are shown and will be discussed further below.

Interactions	Hamiltonian
Chemical shift	$H_{cs} = \gamma \hat{\mathbf{I}} \cdot \boldsymbol{\sigma} \cdot \hat{\mathbf{B}}_0$
Dipole-Dipole	$H_D = \left(\frac{\mu_0}{4\pi} \frac{\gamma_I \gamma_S h}{r_{IS}^3} \right) \left(\hat{\mathbf{I}} \cdot \hat{\mathbf{S}} - \frac{3\left(\hat{\mathbf{I}} \cdot \hat{r}_{IS} \right)\left(\hat{\mathbf{S}} \cdot \hat{r}_{IS} \right)}{r_{IS}^2} \right) = \hat{\mathbf{I}} \cdot \mathbf{D} \cdot \hat{\mathbf{S}}$
J-coupling	$H_J = \hat{\mathbf{I}} \cdot \mathbf{J} \cdot \hat{\mathbf{S}}$

Table 1.1. Hamiltonians of common spin interactions present in NMR. Where I and S represents the vector components of the spins, σ is the chemical shift tensor, γ the gyromagnetic ratio, B_0 is the externally applied magnetic field, the distance between the spins is r_{IS}, **D** is the dipolar coupling tensor and **J** is the J-coupling tensor.

Chemical shift

The magnetic field experienced by a nucleus will differ depending on its position in the magnetic field and is caused by the interaction of the nucleus with the surrounding electrons. The interaction of the nucleus with the electrons alters ("shields", B_s) the nucleus from the externally applied magnetic field (B_0) leading to a change of the local magnetic field (B_{local}) causing a shift of the signal in the NMR spectrum.

$$\mathbf{B}_{\text{local}} = \mathbf{B}_0 + \mathbf{B}_s \tag{1.8}$$

The magnitude of shielding is in principle linearly dependent on the magnetic field applied and is given by eq. 1.9.

$$\mathbf{B}_s = \boldsymbol{\sigma} B_0 = \begin{pmatrix} \sigma_{xx} & \sigma_{xy} & \sigma_{xz} \\ \sigma_{yx} & \sigma_{yy} & \sigma_{yz} \\ \sigma_{zx} & \sigma_{zy} & \sigma_{zz} \end{pmatrix} \begin{pmatrix} 0 \\ 0 \\ B_0 \end{pmatrix} = \begin{pmatrix} \sigma_{xz} B_0 \\ \sigma_{yz} B_0 \\ \sigma_{zz} B_0 \end{pmatrix} \tag{1.9}$$

Eq. (1.9) assumes that the magnetic field is along de z-axis and thus $\sigma_{xz}B_0$ and $\sigma_{yz}B_0$ represent the corresponding component into the x or y direction. Correspondingly, the small field caused by the electrons is not necessarily parallel with the applied magnetic field, but depends on the orientation of the molecule itself. The consequence of this interaction can be seen in

Figure 1.4a where the chemical shift changes for a single crystal depending on the orientation. In a typical powder sample, there will be numerous orientations present. Hence the observed spectra would be the result of the summation of the NMR spectra of the different individual orientations as shown in Figure 1.4b, leading to what is called a "Powder spectrum".

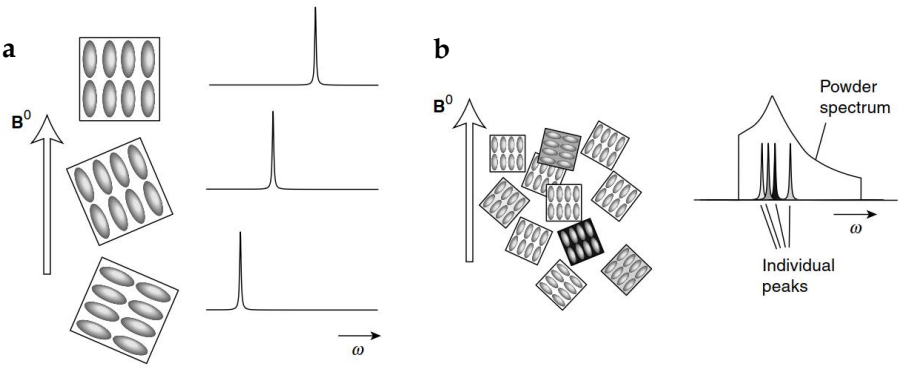

Figure 1.4. a) Influence of the orientation on chemical shift of a single crystal in a static magnetic field. b) Formation of the powder pattern observed for static samples. Image taken from ref[1].

However, in liquids anisotropic interactions are usually averaged out and only isotropic interactions contribute to the NMR spectrum. Experimentally this effect can be seen on, for example, fullerene shown in Figure 1.5. At room temperature fullerene is mobile and thus leads to averaging out anisotropic interactions. In contrast, when cooled to 100K under static conditions the NMR spectrum shows a broad signal which is indicative of additional (anisotropic) interactions contributing to the spectrum.

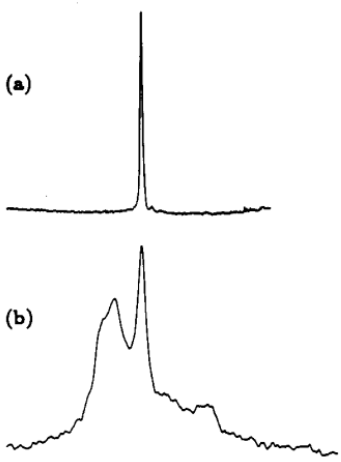

Figure 1.5. a) ^{13}C NMR spectrum of C_{60} powder at 296K, without sample spinning. The narrowness of the line indicates rapid rotation of C_{60} molecules in the solid state. b) Spectrum of C_{60} at 100K. Image reproduced from ref[5].

Dipolar coupling

Other than influencing the chemical shift, the molecular orientation also influences spin-spin interactions such as the dipole-dipole coupling between 2 spins. The strength of the dipole-dipole coupling for a spin pair under high magnetic field conditions is given by:

$$H_D = \left(\frac{\mu_0}{4\pi}\frac{\gamma_I \gamma_S h}{r_{IS}^{\,3}}\right)\left(\mathbf{I}^{\uparrow}\cdot\mathbf{S}^{\uparrow} - \frac{3\left(\mathbf{I}^{\uparrow}\cdot r_{IS}^{\uparrow}\right)\left(\mathbf{S}^{\uparrow}\cdot r_{IS}^{\uparrow}\right)}{r_{IS}^{\,2}}\right) \tag{1.10}$$

Following the approach as describe by Abragam[6], changing from Cartesian coordinates to polar coordinates and using the raising and lowering operators:

$$\begin{aligned} r_x &= r\sin\theta\cos\varphi \\ r_y &= r\sin\theta\sin\varphi \\ r_z &= r\cos\theta \\ I_+ = I_x + iI_y \quad &\text{and} \quad I_- = I_x - iI_y \end{aligned} \tag{1.11}$$

leads to eq. 1.12.

$$H_D = \left(\frac{\mu_0}{4\pi}\frac{\gamma_I\gamma_S h}{r_{IS}^{\ 3}}\right)\left(\begin{array}{l}\mathbf{I}^{\uparrow}\cdot\mathbf{S}^{\uparrow} - 3\left[I_z\cos\theta + \sin\theta(I_x\cos\varphi + I_x\sin\varphi)\right]\times \\ \left[S_z\cos\theta + \sin\theta(S_x\cos\varphi + S_x\sin\varphi)\right]\end{array}\right) \quad (1.12)$$

Eq. 1.12 can be written in a form known as the "dipolar alphabet" shown in eq. 1.13.

$$\begin{aligned} H_D &= \left(\frac{\mu_0}{4\pi}\frac{\gamma_I\gamma_S h}{r_{IS}^{\ 3}}\right)(A+B+C+D+E+F) \\ A &= \left(1-3\cos^2\theta\right)I_zS_z \\ B &= \frac{1}{2}\left(1-3\cos^2\theta\right)\left(I_zS_z - \vec{\mathbf{I}}\cdot\vec{\mathbf{S}}\right) \\ C &= -\frac{3}{2}\sin\theta\cos\theta e^{-i\varphi}\left(I_zS_+ + I_+S_z\right) \\ D &= -\frac{3}{2}\sin\theta\cos\theta e^{i\varphi}\left(I_zS_- + I_-S_z\right) \\ E &= -\frac{3}{4}\sin^2\theta e^{-i2\varphi}I_+S_+ \\ F &= -\frac{3}{4}\sin^2\theta e^{i2\varphi}I_-S_- \end{aligned} \quad (1.13)$$

Since a magnetic field (B_0) is applied along the z-axis it will influence the dipolar Hamiltonian and will cause certain terms to become negligible when a time-averaging is performed.

$$H_{D,ave} = \frac{1}{\tau}\int_0^t H_D\, dt \quad (1.14)$$

When the time-averaging is performed, it will cause terms C to F to vanish in all cases, since these terms are time-dependent and will hence be averaged out. Term A is independent of rotations along the z-axis and will therefore remain as it is time-independent. However, term B will dependent on the type of nuclei considered for the coupling. In the case of a homonuclear interaction (when spin I and S are of the same nuclear type) the frequency of each nucleus in the magnetic field will be similar and would therefore result in term B being time-independent

and will thus not be averaged out. Therefore, in the homonuclear case both terms A and B need to be taken into account. However, in the heteronuclear case term B is time-dependent, since there will be a frequency difference between the two nuclear spins and term B will hence be averaged out. Apart of nuclear spins we can also consider two electron spins that can be coupled to each other by a direct dipole-dipole interaction. The result will be essentially the same equation as 1.13.

Hyperfine interactions involving electrons

Hyperfine interactions are any type of interaction between a nucleus and electron other than the Coulombic interactions between their charges. We will limit the discussion only to magnetic interactions. The magnetic interaction can be separated into two types: Dipolar coupling and Fermi contact interactions. The Hamiltonian of the dipolar interaction has the familiar form as shown in 1.13, substituting the nuclear gyromagnetic ratio with the gyromagnetic ratio of the electron. The second hyperfine interaction is the Fermi contact. Typically, we use point dipoles to treat a magnetic field caused by a nucleus, however this approximation is only valid for the case when the observed particles are far away. Therefore, this approximation is valid for all electrons occupying the orbitals surrounding the nucleus since they are never at the nucleus except for the s-orbital. This effect results in an average magnetic field from the nucleus experienced by the electron in the s-orbital that is not equal to zero. In the EPR spectra the Fermi contact would result into additional splitting being present, shown for example in Figure 3.1 (**chapter 3**) where an EPR spectra of a nitroxide radical is shown and in the region of 9.84 Tesla the signal is split into additional lines due to the interaction with a spin=1 nitrogen.

J-coupling

Similar to the dipolar interaction J-couplings can be present between nuclei and electrons, since this interaction is mediated by the electrons. As described above the nucleus is interacting with a nearby electron due to the Fermi contact. This results into an interaction with one of the orientations possible of the electron spin. However, the electron can interact with another electron in a bond and following the Pauli principle the second electron should have an opposite spin compared to the first electron. The second electron will have a hyperfine interaction with a second nucleus (from the bond) and can have its spin orientated either along or against the magnetic field (assuming spin=1/2). The spin orientations will result in a small energy

difference due to nuclear orientations in these bonds. The resulting Hamiltonian can be written as:

$$H_J = \vec{\mathbf{I}} \cdot \mathbf{J} \cdot \vec{\mathbf{S}} \qquad (1.15)$$

Unlike the anisotropic dipolar interaction, the J-coupling is isotropic and will thus be present in liquids despite the tumbling of the molecules.

Magic Angle Spinning

It was shown in Figure 1.5 that when the sample is allowed to tumble that the anisotropic interaction would average out and therefore lead to a spectrum with a higher resolution. However, since the molecules do not tumble in the solid state these anisotropic interactions would be present reducing the resolution of the spectrum. Therefore, the samples are usually spun in solid-state NMR in order to perform averaging. By spinning the sample at an angle of θ=54.74° (referred to as the magic angle) allows for averaging of the dipolar interaction as well (see eq. 1.13). Magic Angle spinning (MAS) can hence remove such anisotropic interaction effectively leading to a spectrum with improved resolution. The first MAS experiment performed with sample spinning was by Andrew et al[7] in 1958 on a single crystal of sodium chloride. Nowadays much higher spinning rates can be employed allowing the averaging of ^{13}C-^{13}C and ^{13}C-^{1}H dipolar couplings, having a coupling strength on the order of ~7.5kHz and ~30kHz respectively. However as mentioned above (eq. 1.5) there is a benefit on detecting on a nucleus with a higher Larmor frequency in terms of sensitivity. For this reason, NMR signal detection usually occurs in solution NMR on ^{1}H nuclei and the same is preferred in solid-state NMR. However due to strong ^{1}H-^{1}H couplings (~120kHz) being present and the spinning rate being limited, it is not possible to fully average out the interaction. Note that these interactions are averaged out in solution NMR due to the tumbling of the molecules. Therefore, detection in solid-state NMR is usually performed on nuclei like ^{13}C while the ^{1}H-spins are being decoupled during detection in order to improve the resolution in the spectrum. Despite the ^{1}H-^{1}H coupling not being fully averaged out, performing ^{1}H-detection on increasingly faster spinning samples does lead to a significant improved resolution in the spectrum as shown in Figure 1.6 on a glycine sample. The combination of fast spinning with spin-dilution however will lead to a on average reduced ^{1}H-^{1}H coupling, allowing high resolution ^{1}H-detected spectra

to be obtained as shown in **chapter 2**. Currently commercial probes are able to achieve spinning speeds up to 110kHz and achieving such speeds allows for obtaining better resolved ^{1}H-detected spectra and even of fully protonated samples[8–11].

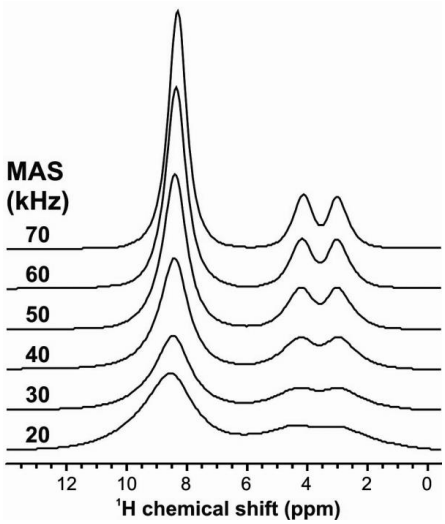

Figure 1.6. ^{1}H detected NMR spectra of a glycine powder sample at different spinning frequencies. Image taken from ref[12].

Dynamic Nuclear Polarization (DNP)

As was shown in Figure 1.2 the electron polarization is much larger than the nuclear polarization of ^{1}H- and ^{13}C-spins under similar experimental conditions. With DNP, the much larger electron polarization is exploited by transferring this polarization to a nuclear spin. The first DNP experiment was performed by Carver and Slichter[13] in 1953 on Lithium where an NMR enhancement of the Lithium signal was visible after irradiation on the electron frequency. One of the first applications of DNP with solid-state MAS NMR was shown by Wind et al[14] enhancing the ^{13}C NMR signal intensity of coal by using the radicals present in the sample. Later on, a more generally applicable method was developed by the Griffin group[15] which made it possible to conduct DNP experiments at higher magnetic fields using high frequency microwaves generated by a gyrotron[15]. These experiments made use of doping the sample with mono- or bi-radicals[15–18]. Depending on the choice of the radical this would allow the polarization transfer to occur through the solid-effect or cross-effect mechanism which are discussed below.

Level anti-crossing (LACs)

LACs are a phenomenon where different energy states are allowed to mix when the energy level slowly changes. The importance of these crossings is best shown for the case of a two-level system. Therefore, assume that we have a system with a Hamiltonian H_0 as shown in eq. 1.16.

$$H_0 = \begin{pmatrix} E_1 t & 0 \\ 0 & E_2 t \end{pmatrix} \tag{1.16}$$

The eigenstates of the system are |1>= $\begin{pmatrix} 1 \\ 0 \end{pmatrix}$ and |2>= $\begin{pmatrix} 0 \\ 1 \end{pmatrix}$, and eigenvalues E_1t and E_2t, such a system can be representative for a spin=1/2 in a magnetic field. As there are no elements coupling the 2 states (since there are no off-diagonal elements) it would have the following consequence that if a state is prepared in state |1> it will remain in |1> despite changes in energy. Assume that the Hamiltonian is exposed to a perturbation (W) consisting of only off-diagonal elements as shown in eq. 1.17.

$$H = H_0 + W = \begin{pmatrix} E_1 t & 0 \\ 0 & E_2 t \end{pmatrix} + \begin{pmatrix} 0 & W \\ W & 0 \end{pmatrix} \tag{1.17}$$

Due to the perturbation, the eigenvalues are no longer given by the diagonal elements of H_0. Rather, the eigenvalues of eq. 1.17 are now given in eq. 1.18.

$$E_+ = \frac{1}{2}\left(E_1 t + E_2 t + \sqrt{(E_1 t - E_2 t)^2 + 4W^2}\right) \tag{1.18}$$
$$E_- = \frac{1}{2}\left(E_1 t + E_2 t - \sqrt{(E_1 t - E_2 t)^2 + 4W^2}\right)$$

Plotting the eigenvalues of eq. 1.16 and 1.17 reveals the influence of the perturbation applied, as shown in Figure 1.7. Here, it is assumed that the eigenvalues change with respect to time. For the case when no perturbation is applied the eigenvalues cross, but if the initial state was |1> then it will remain in |1> likewise for |2>. However, when a perturbation is included in the Hamiltonian the eigenvalues no longer cross and starting from |1> may lead to a final state |2>.

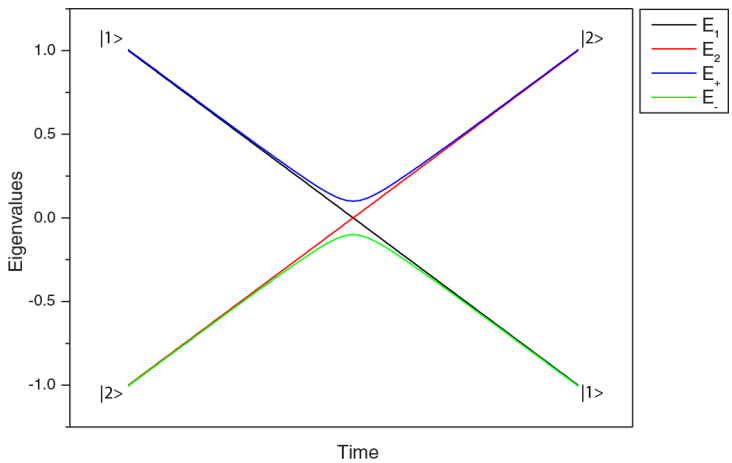

Figure 1.7. Eigenvalues of equations 1.16 and 1.17 plotted for arbitrary parameters, assuming that E_2=-E_1.

Thus, the perturbation allows the different states to mix through these level anti-crossings (LACs) and as will be shown further below as well as in **chapter 3** LACs play an important role in the cross-effect DNP mechanisms. The 'mixing efficiency' at these type of crossings consisting of two levels can be analysed by the Landau-Zener equation[19]. In the case of the

Hamiltonian given in eq. 1.17 (and the example shown) we obtain eq. 1.19 where P_{LAC} represents the mixing probability.

$$P_{LAC} = 1 - e^{\left(-\frac{\pi W^2}{E_{1,2}}\right)} \approx \frac{\pi W^2}{E_{1,2}} \qquad (1.19)$$

Solid-effect

Solid-effect DNP is a mechanism used for transferring polarization from an electron to a nucleus. This process was one of the first mechanisms to be employed in combination with solid-state NMR[15]. This mechanism requires the use of mono-radicals such as TEMPO where interactions between the unpaired electrons are negligible. The solid-effect mechanism can be understood by considering a 2-spin system consisting of an electron and a nucleus. Irradiating this spin system with a microwave frequency ω_{SE} which matches the condition given by eq. 1.20 allows for a so called "flip-flop" transitions to occur.

$$\omega_{SE} = \omega_e \pm \omega_n \qquad (1.20)$$

Irradiating with frequency ω_{SE} allows transfers of polarization to occur from the electron to the nucleus. As shown in Figure 1.8 in total there are 4 energy levels present and irradiating the sample with a microwave frequency ω_{SE} leads to equalization of the population between 2 states, which increases the net nuclear polarization[20].

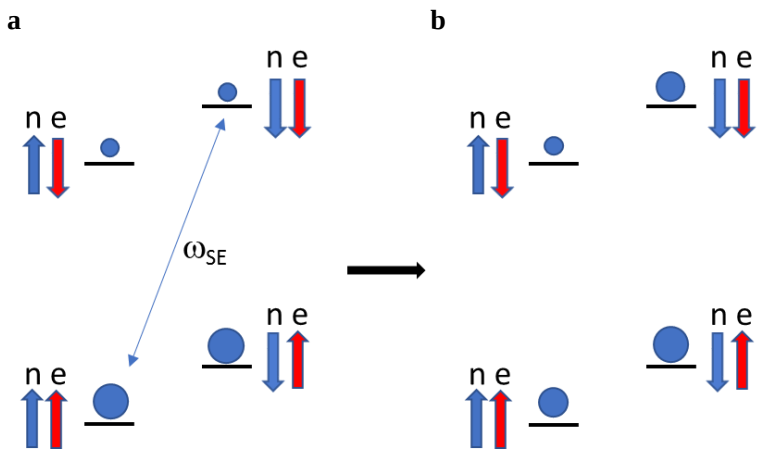

Figure 1.8. Solid-effect energy level diagram. Where the blue spheres indicate the polarization of the nuclei in each state. a) Shows the polarization before irradiation and b) the polarization distribution after irradiation.

Cross-effect

Unlike the solid-effect the cross-effect relies on a 3-spin mechanism[21] involving 2 electrons and a nucleus. An early demonstration involved tethering 2 TEMPO molecules together[17] which resulted in an increase in the observed DNP enhancement by a factor of 4 compared to the solid-effect. These observations led to the development of biradicals such as TOTAPOL and AMUPol (shown in Figure 1.9) which performed better in terms of enhancement and were synthesized with more favourable properties such as water-solubility allowing these types of radicals to be broadly used as polarizing agents for biomolecules. The cross-effect mechanism relies on transferring the polarization from the electrons to nuclei with level anti-crossings. Essentially there are a total of 8 energy levels, shown in Figure 1.10. When the frequency difference between the electrons matches the frequency of a nuclei (eq. 1.21) polarization transfer is able to occur.

$$\omega_{e1} \pm \omega_{e2} = \omega_n \qquad (1.21)$$

An unpaired electron has similar anisotropic interactions as the nuclei mentioned before, therefore depending on the molecular orientation the EPR resonance frequency of the electron will be modulated (similar to the chemical shift).

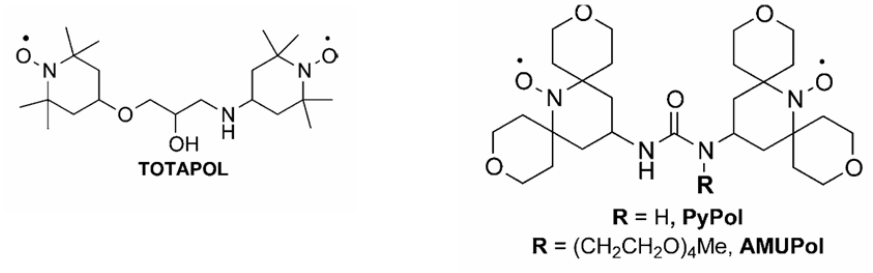

Figure 1.9. Examples of biradicals used as polarizing agents for cross-effect DNP[16][18].

This essentially means that under static conditions only a small ensemble of the orientations present will fulfil the matching condition allowing the polarization transfer to occur. However, in solid-state NMR the sample is typically spun under MAS conditions for the reasons mentioned above. MAS will hence modulate the EPR resonance frequency of each electron, allowing the energy levels to fluctuate[21]. This is shown in Figure 1.10b where the 4 central energy levels are shown fluctuating under sample spinning. At certain positions during the rotation the energy levels show level anti-crossing allowing these levels to mix and therefore exchange polarization, eventually leading to signal enhancement. There are different types of level anti-crossing conditions that can occur[21]. The first one requires that the microwave frequency ω_m matches the frequency of one of the electrons (ω_{e1} or ω_{e2}), indicated by (1) in Figure 1.10b. This will lead to a polarization difference between the electrons. The other crossing that can occur is the matching condition for the cross-effect where the difference between the electron frequencies matches the nuclear frequency, $\omega_{e1} \pm \omega_{e2} = \omega_n$, indicated by (2) in Figure 1.10b. This level anti-crossing allows transfer to occur from the electrons to the nuclei. Though it is not the predominant effect there is also a solid-effect level crossing that might occur when the sum or difference of an electron- and nuclear-frequency matches the microwave frequency, $\omega_{e1,2} \pm \omega_n = \omega_m$. The last crossing that can occur is an electron-electron crossing, $\omega_{e1} = \omega_{e2}$ and cause the polarization to be exchanged between the 2 electrons, indicated by (3) in Figure 1.10b.

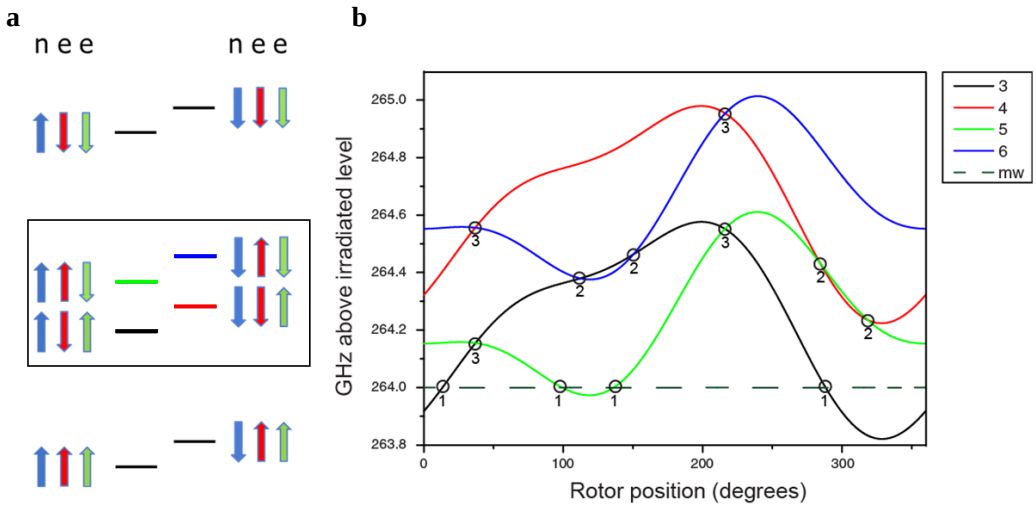

Figure 1.10. a) Energy levels present in the cross-effect mechanisms where to box highlights the 4 central energy levels. b) Shows the modulation of the central energy levels under sample spinning

In **chapters 3** we will discuss parameters influencing the cross-effect DNP mechanism concerning the field dependence. Furthermore, applications of the cross-effect DNP mechanism to enhance NMR signals in life (**chapter 4**) and material science (**chapter 5**) will be shown. In **chapter 6** new radicals will be presented which are particularly interesting for high-field applications.

References

[1] M. H. Levitt, *Spin Dynamics : Basics of Nuclear Magnetic Resonance*, John Wiley & Sons, **2001.**

[2] F. Bloch, W. W. Hansen, M. Packard, *Phys. Rev.* **1946**, *70*, 474–485.

[3] E. M. Purcell, H. C. Torrey, R. V. Pound, *Phys. Rev.* **1946**, *69*, 37–38.

[4] A. Pines, M. G. Gibby, J. S. Waugh, *J. Chem. Phys.* **1972**, *56*, 1776–1777.

[5] R. Tycko, R. C. Haddon, G. Dabbagh, S. H. Glarum, D. C. Douglass, A. M. Mujsce, *J. Phys. Chem.* **1991**, *95*, 518–520.

[6] A. Abragam, *The Principles of Nuclear Magnetism*, London: Oxford Univ. Press **1961**.

[7] E. R. Andrew, A. Bradbury, R. G. Eades, *Nature* **1958**, *182*, 1659–1659.

[8] J. Stanek, L. B. Andreas, K. Jaudzems, D. Cala, D. Lalli, A. Bertarello, T. Schubeis, I. Akopjana, S. Kotelovica, K. Tars, et al., *Angew. Chemie Int. Ed.* **2016**, *55*, 15504–15509.

[9] L. B. Andreas, K. Jaudzems, J. Stanek, D. Lalli, A. Bertarello, T. Le Marchand, D. Cala-De Paepe, S. Kotelovica, I. Akopjana, B. Knott, et al., *Proc. Natl. Acad. Sci. U. S. A.* **2016**, *113*, 9187–92.

[10] S. Penzel, A. A. Smith, V. Agarwal, A. Hunkeler, M.-L. Org, A. Samoson, A. Böckmann, M. Ernst, B. H. Meier, *J. Biomol. NMR* **2015**, *63*, 165–186.

[11] A. Böckmann, M. Ernst, B. H. Meier, *J. Magn. Reson.* **2015**, *253*, 71–79.

[12] nmr900.ca/testspectra_e.html

[13] T. R. Carver, C. P. Slichter, *Phys. Rev.* **1953**, *92*, 212–213.

[14] R. A. Wind, M. J. Duijvestijn, C. van der Lugt, A. Manenschijn, J. Vriend, *Prog. Nucl. Magn. Reson. Spectrosc.* **1985**, *17*, 33–67.

[15] L. R. Becerra, G. J. Gerfen, R. J. Temkin, D. J. Singel, R. G. Griffin, *Phys. Rev. Lett.* **1993**, *71*, 3561–3564.

[16] C. Song, K.-N. Hu, C.-G. Joo, T. M. Swager, R. G. Griffin, *J. Am. Chem. Soc.* **2006**, *128*, 11385–90.

[17] K.-N. Hu, H. Yu, T. M. Swager, R. G. Griffin, *J. Am. Chem. Soc.* **2004**, *126*, 10844–5.

[18] C. Sauvée, M. Rosay, G. Casano, F. Aussenac, R. T. Weber, O. Ouari, P. Tordo, *Angew. Chemie Int. Ed.* **2013**, *52*, 10858–10861.

[19] C. Zener, *Proc. R. Soc. London A Math. Phys. Eng. Sci.* **1932**, *137*.

[20] A. Abragam, M. Goldman, *Reports Prog. Phys.* **1978**, *41*, 395–467.

[21] K. R. Thurber, R. Tycko, *J. Chem. Phys.* **2012**, *137*, 1-14.

CHAPTER 2

An Efficient Labelling Approach to Harness Backbone and Side-Chain Protons in ^{1}H-Detected Solid-State NMR Spectroscopy

This chapter is based on the following publication:

D. Mance, T. Sinnige, M. Kaplan, S. Narasimhan, M. Daniëls, K. Houben, M. Baldus, and M. Weingarth, "An Efficient Labelling Approach to Harness Backbone and Side-Chain Protons in 1H-Detected Solid-State NMR Spectroscopy," *Angew. Chemie - Int. Ed.*, vol. 54, no. 52, pp. 15799–15803, Dec. 2015.

Introduction

The recent advent of ^{1}H-detection in biological ssNMR can greatly increase spectral sensitivity,[1] and thereby bears the potential to critically broaden the scope of ssNMR. The prevailing method to detect ^{1}H in solid proteins is perdeuteration, i.e., the complete deuteration and subsequent reintroduction of exchangeable ^{1}H in protonated buffers. This labelling scheme largely removes line-broadening ^{1}H–^{1}H dipolar couplings and can provide spectra of extremely high quality.[2] Moreover, it allows for automated backbone assignments[3] and probing contacts between backbone amino ^{1}H (H^{N}), important to define protein fold.[4]

However, the absence of aliphatic side chain ^{1}H in perdeuterated proteins curtails the potential of ^{1}H-detection, given that side chains are important factors for protein structure and function. In addition, the availability of side chain ^{1}H could facilitate the assignment of complex proteins. In general, to assign and harness side chain ^{1}H has remained a major difficulty for ^{1}H-detected ssNMR. In principle, fully protonated proteins in combination with magic angle spinning (MAS) frequencies >100 kHz[2d] could provide a future avenue to side chain ^{1}H, as put into perspective with soluble and membrane proteins.[5] However, it can be envisaged that the residual ^{1}H linewidth and spectral crowding will remain a challenge for larger proteins. Moreover, for proteins such as membrane proteins with a substantial inhomogeneous contribution to the ^{1}H linewidth, >100 kHz MAS may not compensate for the sensitivity loss due to comparably small sample volumes. Excellent resolution and assignments of aliphatic ^{1}H have been reported with residual adjoining protonation (RAP) that relies on the random incorporation of ^{1}H in a deuterated protein matrix.[6] Moreover, approaches such as ILV-, ^{1}H cloud- or SAIL-labelling can be used to probe contacts between side chain ^{1}H of specific types of amino acids.[7] Yet, such approaches employ isolated labels that may be very difficult to assign *de-novo* and only give access to a selection of side chain ^{1}H. To assign side chain ^{1}H and exploit them for structural studies, even in larger proteins, a labelling scheme that i) provides a high global ^{1}H density and ii) mitigates spectral crowding nonetheless, could be very advantageous. This prompted us to explore 'fractional deuteration' in ^{1}H-detected ssNMR. This labelling scheme, based on protonated ^{13}C-glucose and D_2O in the growth medium, was previously proposed in solution NMR as alternative to ILV-labelling and in ^{13}C-detected ssNMR for spectral editing.[8] These studies reported that certain carbons such as Cα get highly deuterated in fractionally deuterated proteins, while many side chain carbons retain sizeable ^{1}H levels.

Herein we demonstrate that fractional deuteration provides access to well-resolved H^N and side chain ^1H of virtually all residues in one sample and allows assigning and harnessing these ^1H for structural studies. Importantly, even though our approach works at much higher ^1H levels, we observe an excellent resolution (0.07 ppm) for the H^N protons in fractionally deuterated (FD) membrane-embedded K^+ channel KcsA, which rivals the resolution in the perdeuterated channel. We outline our approach on ubiquitin and then use it to study KcsA including its membrane topology, dynamics, as well as important channel–water interactions.

Materials and Methods

Fractionally deuterated ubiquitin was produced in a D_2O based M9 medium supplemented with 2 g/L ^{13}C-glucose and 0.5 g/L $^{15}NH_4Cl$. The fully protonated sample was produced in a H_2O based M9 medium supplemented with 2 g/L ^{13}C-glucose and 0.5 g/L $^{15}NH_4Cl$. Purification and further sample preparation steps were done as described in (Ref. [7b]). The yield for the fractionally deuterated sample was 15 mg/l. Fractionally deuterated KcsA was expressed and purified as previously described,[15c] with the exception that D_2O instead of H_2O was used in the expression minimal medium. The yield for the FD channel was 11 mg/l. Reconstitution in E. coli polar lipids (Avanti) was performed at a 100/1 lipid/channel molar ratio using biobeads as previously described.[15c] After reconstitution, the fractionally deuterated channel was back-exchanged in fully protonated phosphate buffer (pH 7.0) and incubated for three weeks prior to the ssNMR measurements.

All experiments were carried out at 18.8 T static magnetic field (800 MHz ^1H frequency) and 52 kHz MAS if not indicated otherwise. The sample temperature was set to 300 K. Water suppression was achieved with the MISSISSIPPI[5a] scheme. Decoupling was performed with the PISSARRO[10] scheme during all direct and indirect acquisition periods. For all experiments and all nuclei, the decoupling amplitude was set to one quarter of the MAS frequency, i.e., 13 kHz. Decoupling times were optimized and set to 31.5 µs for ^1H decoupling, 47.6 µs for ^{13}C decoupling and 53 µs for ^{15}N decoupling. For all experiments, quadrature-detection in the indirect dimensions was achieved using TPPI. The pulse sequence used to acquire 2D $^{13}C/^{15}N$-^1H spectra was described in Ref. ([7b]).

Results

Figure 2.1 shows ^{1}H-detected 2D CH and NH spectra of FD [^{13}C,^{15}N]-ubiquitin in aqueous (100 % H_2O) buffers, acquired at 52 kHz MAS and 800 MHz ^{1}H-frequency using MISSISSIPI water suppression[9] and low-power PISSARRO decoupling.[10] These spectra are of remarkable quality and feature a resolution as high as 0.05 and 0.07 ppm for aliphatic and exchangeable ^{1}H, respectively. The absence of CαHα correlations, which typically appear around 50–65 ^{13}C ppm/3.0–5.0 ^{1}H ppm, is readily visible in the CH spectrum. A quantitative analysis using solution NMR revealed (see Table 2.1), next to the absence of Hα protons (<2 % population), an interesting pattern of ^{1}H depletion for the side chains in FD ubiquitin. The pyruvate-derived branched-chain amino acids (Ile, Leu, Val) exhibit very low (≤5 %) ^{1}H levels at the Cβ position, which is the same for the amino acids (Arg, Gln, Glu, Pro) derived from α-ketoglutarate (≤8 %). Amino acids that follow other pathways (such as Asn, Asp, His, Lys, Ser, Thr), however, retain much higher ^{1}H levels between 30–45 % (90 % for Ser) at Cβ, with slightly less values for aromatic amino acids (Phe, Tyr). Most other carbons, further away from the backbone, feature equally high ^{1}H levels. Our data are in good agreement with the original solution NMR study, which also provides detailed biochemical explanations.[8a] Hence, many sites remain robustly protonated in FD proteins and yet feature a narrow ^{1}H linewidth because the ^{1}H network is on average starkly diluted. However, we like to emphasize that the local and global ^{1}H density in FD proteins are much higher than in RAP-labelled proteins.[6] Broadening effects due to methylene isotopomers were not observed, probably because CH_2 signals are broadened beyond detection. Methyl groups showed slightly oval lineshapes due to isotopomers, which however did not significantly compromise the ^{1}H resolution (0.05–0.08 ppm), presumably because CH_3 signals are broader and less abundant than CHD_2 or CH_2D signals (see Box I in Figure 2.1A). Prominent features of the CH spectrum of FD ubiquitin are the unusually intense $C\alpha H^{N}$ signals. As it can be readily shown with simulations (Box II in Figure 2.1A), this beneficial effect is caused by the absence of Hα protons in FD proteins.[11]

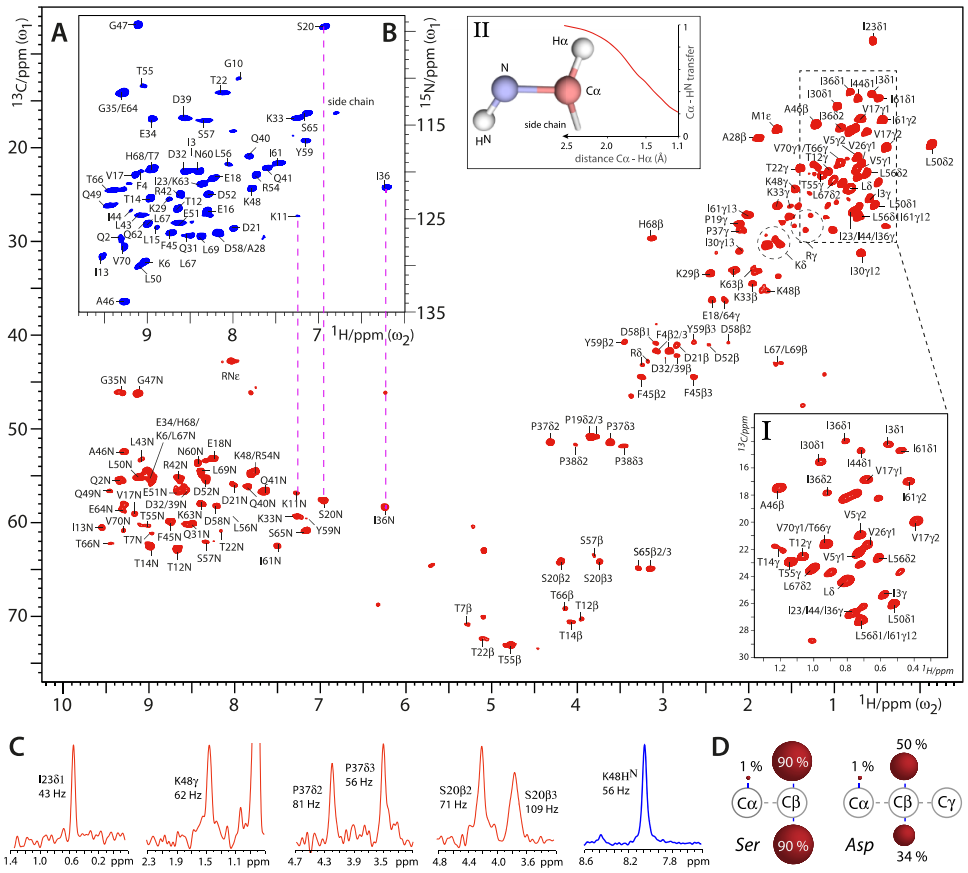

Figure 2.1. ^{1}H-detected ssNMR experiments in FD ubiquitin. A) 2D CH spectrum (in red). Box I shows a zoom in the methyl region. Box II shows simulations of the influence of CαHα dipolar couplings on the CP transfer from Cα to H^N. B) 2D NH spectrum (blue). C) t1 cross-sections from the 2D CH (in red) and NH (blue) experiments. D) Examples of the protonation pattern in FD amino acids. See Table 2.1 for the complete list. Red spheres illustrate the ^{1}H level at a given ^{13}C.

In Figure 2.2 and 2.3A we show assignments in FD ubiquitin, which are based on dipolar transfer. Backbone connectivity's were established with 3D CαNH, Cα(CO)NH and CCH experiments. In the 3D Cα(CO)NH, Cα polarization was prepared by a selective CP step.[2g, 12] These experiments were sufficient for backbone assignments, given that extensive chemical shift data are available for ubiquitin.[13] Side chain assignments were performed with a 3D CCH experiment that included a ^{13}C–^{13}C DREAM[14] mixing block, optimized for one-bond transfer.

	Hα	Hβ	Hγ	Hγ2	Hδ	Hδ2	Hε
Ala	**1**	**26**					
Arg	**1**	**7**	**38**		**31**		
Asp	**1**	**42**					
Asn	**1**	**41**					
Cys	*						
Gln	**1**	**8**	**29**				
Glu	**1**	**8**	**29**				
Gly	**1**						
His	**1**	**30**					
Ile	**1**	**3**	**18**	**40**		**37**	

	Hα	Hβ	Hγ	Hγ2	Hδ	Hδ2	Hε
Lys	**1**	**30**	**46**		**26**		**4**
Met	**8**	*	**56**		*		
Pro	**1**	**2**	**33**		**35**		
Leu	**1**	**5**	**0**		**40**	**40**	
Phe	**1**	**24**					
Ser	**1**	**90**					
Thr	**3**	**30**	**19**				
Trp	*						
Tyr	**1**	**21**					
Val	**1**	**0**	**40**	**44**			

Table 2.1. ^{1}H-populations [%] in FD ubiquitin in comparison to FP ubiquitin. The ^{13}C-^{1}H HSQC spectra were normalized (to account for different sample concentrations) and referenced to ^{15}N-^{1}H HSQC spectra. Subsequently, well-resolved signals (which was the majority of the signals) in the ^{13}C-^{1}H HSQC spectra were integrated in Topspin 3.2 (Bruker) and their intensities compared. Note that ubiquitin features no Cys nor Trp residues, which could hence not be analysed. However, Cys residues share a common metabolic pathway with Ser residues and therefore presumably feature a high degree of protonation at Cβ The Hβ population of Met could not be assessed due to spectral overlap. Hβ with populations above 20 % (in blue) could be readily assigned in 3D CCH experiments, while Hβ with populations below 8 % (in red) were either entirely absent or showed very weak signals.

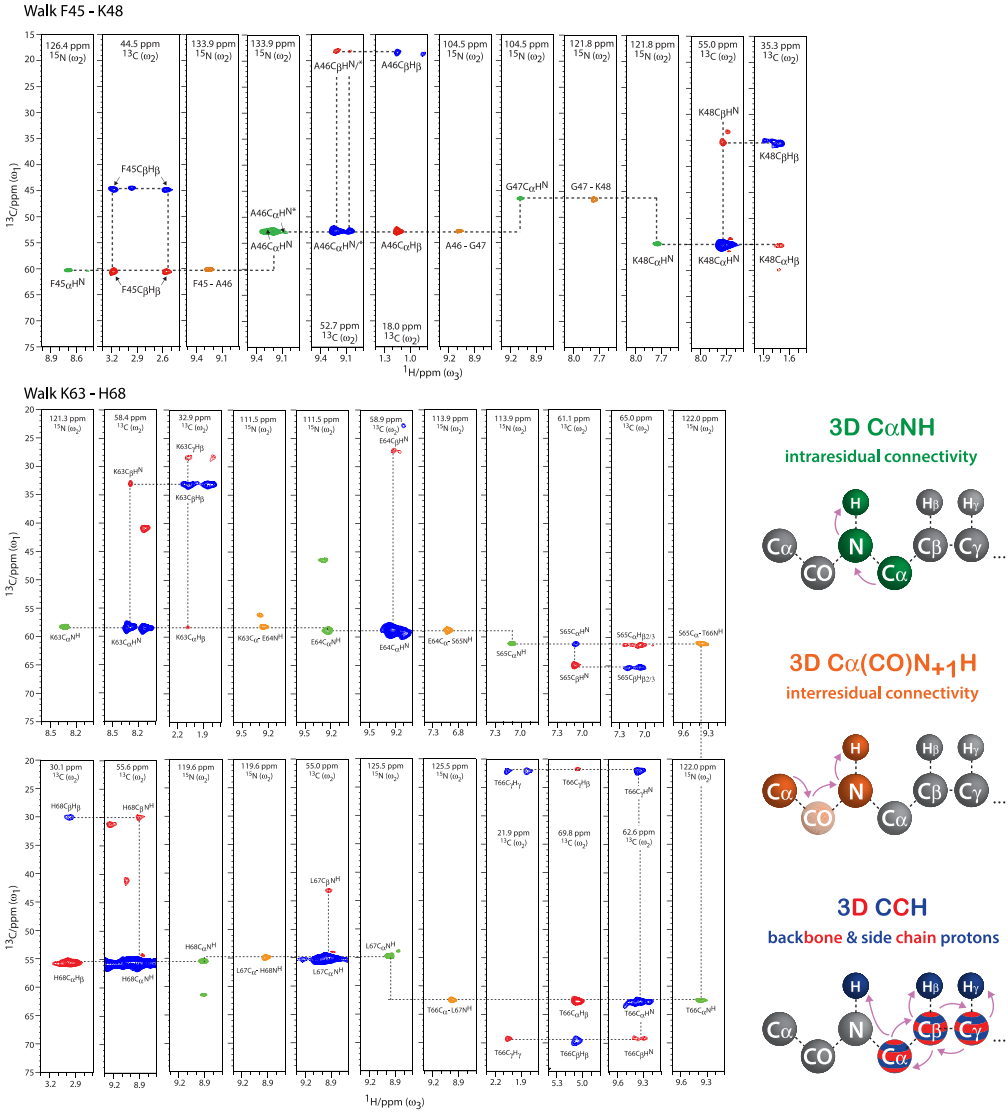

Figure 2.2. Backbone and side chain assignments in FD ubiquitin. Signals from 3D CαNH (green), 3D Cα(CO)NH (orange) and 3D CCH (blue for positive; red for negative signals) experiments, are color-coded. The transfer pathways in the 3D experiments are illustrated on the right. Double quantum DREAM CC transfer was used in the 3D CCH experiment.

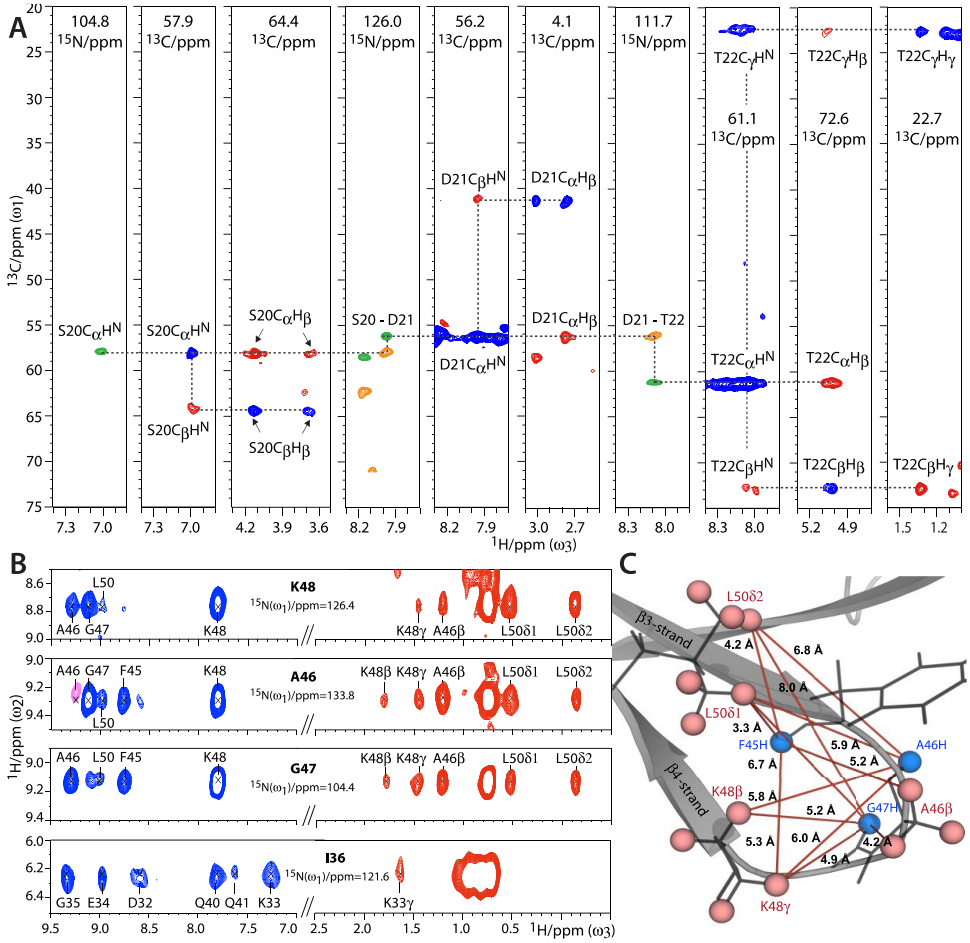

Figure 2.3. ^{1}H-detected assignments and structural studies in FD ubiquitin at 52 kHz MAS. A) Walk through S20–T22. Signals from 3D CαNH (green), Cα(CO)NH (orange) and CCH (blue for positive; red for negative signals) experiments, are color-coded. B) Strips from a 3D NHH experiment. H^N–H^N contacts and interresidual contacts between H^N and side chain ^{1}H are colored in blue and red, respectively. C) Illustration of the contacts shown in B). H^N-H^N contacts are not shown for clarity.

Importantly, the efficient transfer from Cα to H^N in CCH experiments, and hence the presence of intense CαCβHβ and CβCαH^N correlations, allow using the H^N as anchors to connect backbone and side chains, thereby greatly facilitating the assignment process. Moreover, the identification of side chain types is greatly simplified by the pattern of robustly protonated and deprotonated Cβ sites (Table 2.1). CαCβHβ correlations were only detectable for residues with Hβ levels >20 %, which much reduced ambiguity. In total, we could assign the Hβ for 24 of the 28 residues with ^{1}H levels >20 % (ignoring the mobile residues M1, T9, L27).[13b] Other inaccessible Hβ were from surface exposed and likely mobile residues (K11, N25, N60). Further side chain ^{1}H such as the Hγ of Thr or Lys could also be readily assigned. To identify the methyl groups of Leu, Ile, Val, and Met, we resorted to published assignments.[2d, 13a] Such side chain ^{1}H could also be assigned with longer 13C–13C mixing.

Thanks to the high ^{1}H density and resolution in FD proteins, the side chain assignments can be readily exploited for structural studies, which is shown in Figure 2.3B,C. We carried out a 3D NHH experiment with 1.5 ms ^{1}H-^{1}H DREAM mixing,[2d, 7a] in which we detected backbone–backbone H^N–H^N contacts as well as backbone–side chain contacts between H^N and aliphatic ^{1}H. Next to a large number of H^N–H^N contacts, many inter-residual backbone–side chain contacts of up to 8 Å distance could be assigned or identified (based on the Xray structure PDB: 1UBQ). This demonstrates that the high ^{1}H density in FD proteins does not impede long distance magnetization transfer. Unambiguous medium- and long-range ^{1}H–^{1}H contacts involved methyl groups and also methylene groups such as the CβHD and CγHD groups of Lys residues. Especially the latter contacts are noteworthy, since they are complementary to ILV-labelling.

In Figures 2.4 and 2.5, we show the potential of ^{1}H-detection in more complex FD proteins using the K^+ channel KcsA, a well-accepted model for ion channel gating,[15] as an example. FD [^{13}C,^{15}N]-KcsA in the closed-conductive state was reconstituted in *E.coli* lipids and aqueous (100 % H_2O) buffers. We acquired dipolar- based 2D NH and CH spectra of very high quality (Figures 2.4A, 2.5A), featuring a resolution as high as 0.06 and 0.07 ppm for aliphatic and exchangeable ^{1}H, respectively. Remarkably, the H^N resolution in FD KcsA is comparable to perdeuterated KcsA[5c] and the perdeuterated membrane protein OmpG[3a] (0.13–0.18 ppm). This strongly suggests that the availability of side chain ^{1}H in many FD membrane proteins comes at very low or no costs at fast MAS, because the residual ^{1}H linewidth is dominated by inhomogeneous contributions. Hence, fractional deuteration is highly advantageous for ^{1}H-detection in non-microcrystalline proteins.

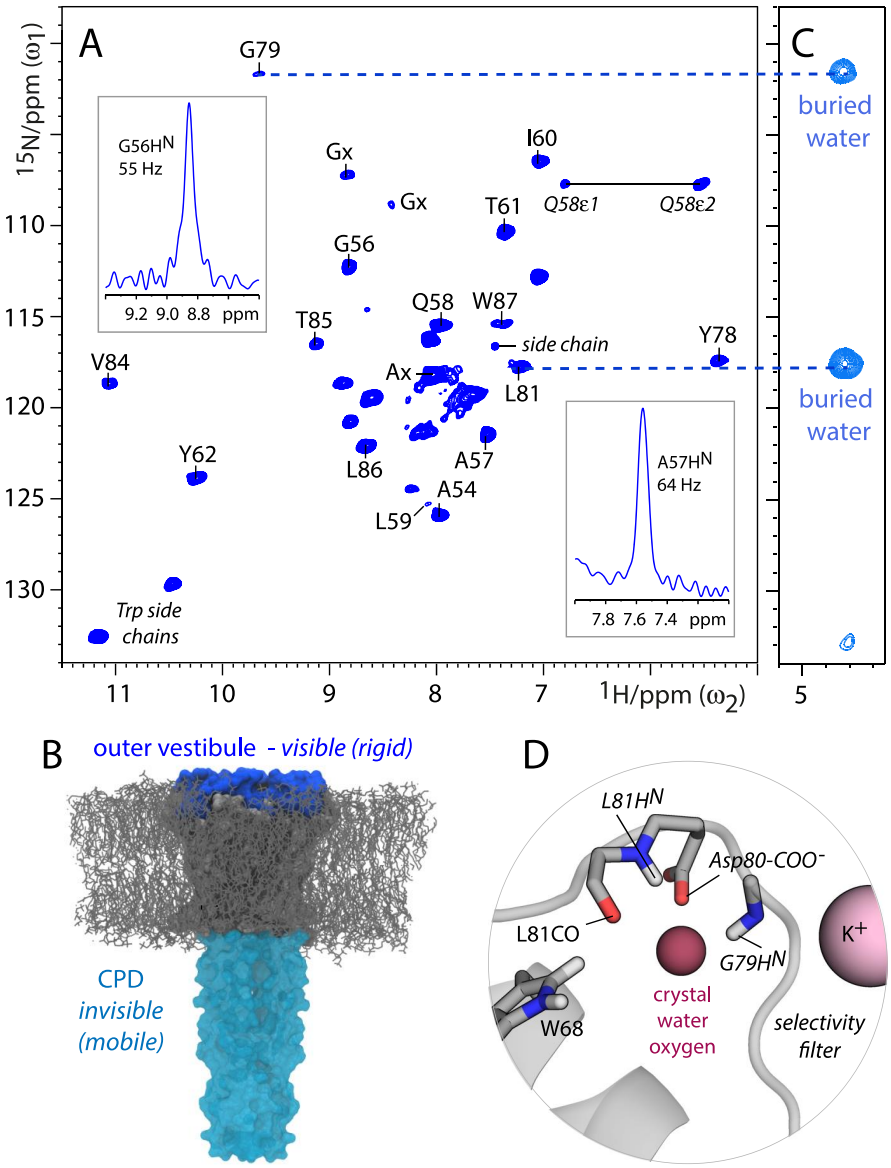

Figure 2.4. ^{1}H-detected studies with FD KcsA (closed-conductive). A) Dipolar-based 2D NH spectrum measured at 52 kHz MAS. B) The CPD is absent in this spectrum due to dynamics. C) Cut-outs of a 2D N(H)H spectrum showing transfer of G79H^{N} and L81H^{N} to buried water behind the selectivity filter, which is illustrated in D) a KcsA structure (PDB: 1K4C).

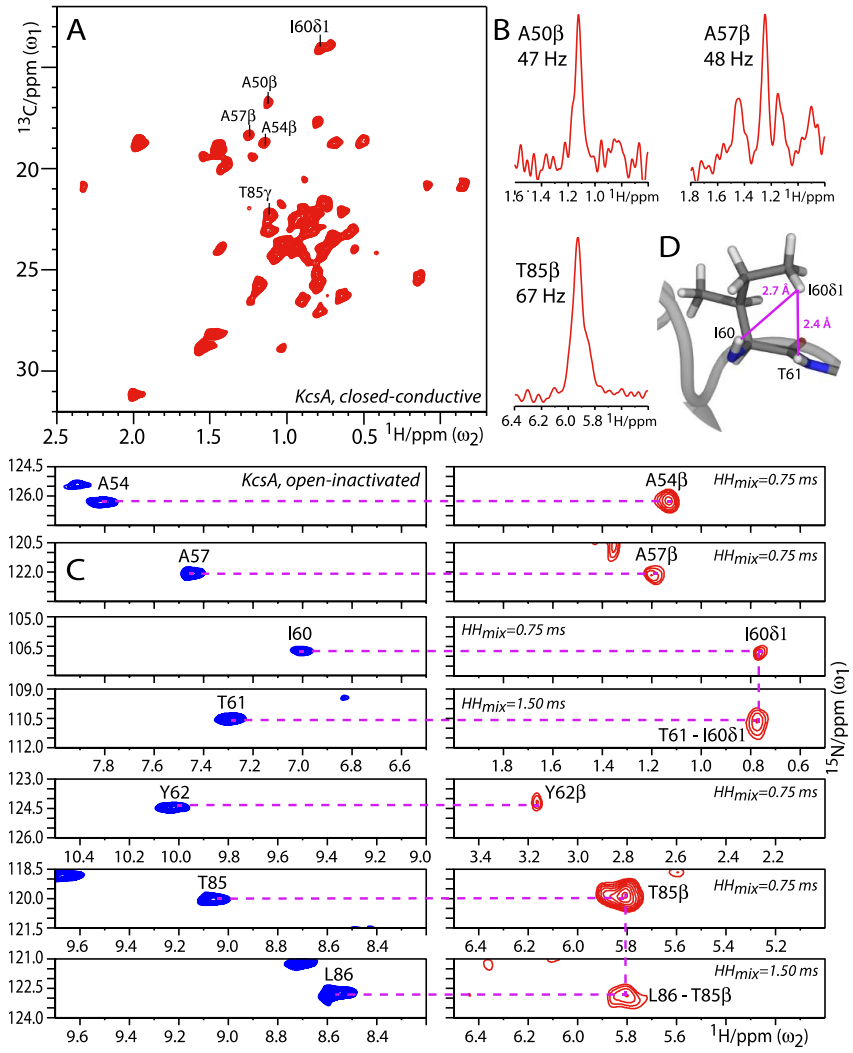

Figure 2.5. ^{1}H-detection of side chains in FD KcsA. A) Cut-out of a 2D CH spectrum measured at 58 kHz MAS with closed-conductive KcsA. Cross-sections are shown in B). C) *Left*: Cut-outs from a 2D NH spectrum (blue); *right*: Cut-outs of a 2D N(H)H spectrum (red); acquired with open-inactivated KcsA. The contact T61H^{N}-I60Hδ1 is illustrated in D), depicting a snapshot of a MD simulation.

FD KcsA was grown in D_2O and only water-exposed residues are visible in the NH spectrum, which we used to study the membrane topology.[2c, 5c] Intriguingly, the NH spectrum showed only around 25 signals, while KcsA features about 70 water-accessible residues, which, in particular, comprise the extracellular outer vestibule (residues 51–64 and 80–86) and the cytoplasmic domain (CPD; residues 118–160). To understand the composition of the NH spectrum, we performed 3D CαNH, 3D Cα(CO)NH, 3D NHH, 2D CH and 2D C(C)H, supported by ^{13}C and ^{15}N chemical shift data.[15c, 15d] We validated our sequential assignments by H^N-H^N contacts that we observed in a 3D NHH experiment. Moreover, by using a slightly longer ^{13}C to ^{1}H CP contact time (700 µs), we obtained many $C\alpha H^{N+1}$ contacts in the 2D CH, which also allowed validating sequential assignments. Altogether, we could assign about 70 % of the H^N signals, which all belonged to the outer vestibule, demonstrating that the CPD is too dynamic for dipolar transfer (Figure 2.4B).

Note that we did not observe marked sensitivity with scalar transfer, implying that CPD dynamics in lipid membranes are relatively slow (µs to ms). We neither observed the CPD in open-inactivated KcsA, where the CPD helices are loosely structured, excluding that the CPD is invisible in the 2D NH due to tight packing. This is a noteworthy finding, given that the conformational flexibility of the CPD is important for KcsA activation gating.[15b] Furthermore, in Figure 2.4C,D we used our ^{1}H assignments to study buried water behind the conductive selectivity filter, which is important for the gating mode.[5c, 15a] How this water is bound is not directly accessible in KcsA Xray structures, since ^{1}H are not resolved. By transferring magnetization from H^N to buried water in 2D and 3D NHH experiments using DREAM mixing, we see that G79H^N and L81H^N contact buried water, strongly suggesting that both coordinate the water oxygen while water ^{1}H contact the nearby Asp80-COO^- group and L81CO. The assignment of spectrum 2.4A was greatly simplified by the availability of side chain ^{1}H. As described for FD ubiquitin, we connected side chain and backbone information via H^N anchor protons (Figures 2.5C and 2.6).

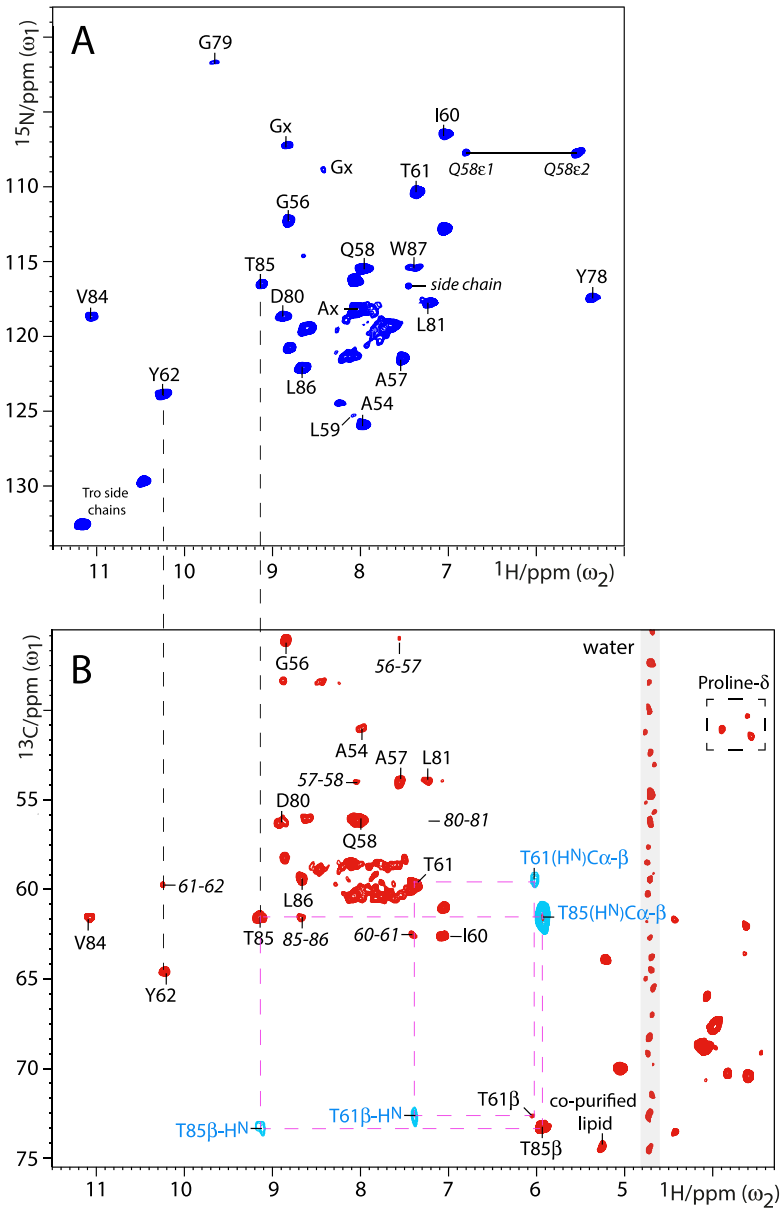

Figure 2.6. A) 2D NH spectrum of FD KcsA (closed-conductive). B) Cut-out of a 2D CH spectrum, which was measured with 700 µs CP contact time for the last ^{13}C to ^{1}H step.

Next to intense CαH^{N} signals, we obtained many weaker CαH^{N+1} signals, which was a simple and very efficient way to cross-validate our sequential assignments. A cut-out of the negative intensity of a 2D C(C)H experiments using ^{13}C–^{13}C DREAM DQ mixing is superimposed (in light blue), in which Thr correlations Cβ–H^{N} and (H^{N})Cα-Hβ are visible. Such intra-residual correlations allowed identifying amino acids types based on Cβ and Hβ chemical shifts and based on the sheer presence or absence of correlations (see Table 2.1). Note signals detected on the side chain of T61 are much weaker than for T85, presumably due to enhanced dynamics, which is in line with the weak intensity of the transfer to Y62Hβ (Figure 2.5C), which agrees with the 2D N(H)H experiment, in which we did not observe transfer to T61Hβ . Noteworthy, T85Cβ (73.2 ^{13}C ppm) is the most low-field ^{13}C signal of KcsA, which implies that the signal at 74.4 13C ppm corresponds to a lipid-head group, mostly likely of ^{13}C labeled co-purified lipids. We *de-novo* assigned side chains via a 2D C(C)H experiment as well as 2D and 3D NHH experiments that included a short (750 µs) ^{1}H-^{1}H DREAM transfer. Note that longer (1.5 ms) ^{1}H-^{1}H mixing also allowed for structural studies of side chain ^{1}H (Figures 2.5C,D). Only residues with Hβ levels >20 % showed (H^{N})CαHβ and NH^{N}Hβ correlations in these experiments, by which we readily assigned residues such as A54, A57, T61, Y62, and T85.

Conclusion

In conclusion, we have introduced a labelling approach for ^{1}H-detected ssNMR that provides a far-reaching access to very well resolved backbone and side chain ^{1}H. Most importantly, for non-microcrystalline samples, our method greatly expands the power of the formidable perdeuteration approach without sacrificing much, if any, ^{1}H resolution. We believe that our approach, which furthermore avoids the use of expensive deuterated glucose, will significantly increase the impact of solid-state NMR spectroscopy, especially for membrane proteins or peptide assemblies such as fibrils that usually cannot be obtained as microcrystalline preparations.

References

[1] Y. Ishii, R. Tycko, *Journal of magnetic resonance* **2000**, *142*, 199-204.

[2] a) V. Chevelkov, K. Rehbein, A. Diehl, B. Reif, *Angewandte Chemie* **2006**, *45*, 3878-3881;

b) R. Linser, M. Dasari, M. Hiller, V. Higman, U. Fink, J. M. Lopez del Amo, S. Markovic, L. Handel, B. Kessler, P. Schmieder, D. Oesterhelt, H. Oschkinat, B. Reif, *Angewandte Chemie* **2011**, *50*, 4508-4512;

c) L. Shi, I. Kawamura, K. H. Jung, L. S. Brown, V. Ladizhansky, *Angewandte Chemie* **2011**, *50*, 1302-1305;

d) V. Agarwal, S. Penzel, K. Szekely, R. Cadalbert, E. Testori, A. Oss, J. Past, A. Samoson, M. Ernst, A. Bockmann, B. H. Meier, *Angewandte Chemie* **2014**, *53*, 12253-12256;

e) J. M. Lamley, D. Iuga, C. Oster, H. J. Sass, M. Rogowski, A. Oss, J. Past, A. Reinhold, S. Grzesiek, A. Samoson, J. R. Lewandowski, *Journal of the American Chemical Society* **2014**, *136*, 16800-16806;

f) P. Schanda, S. Triboulet, C. Laguri, C. M. Bougault, I. Ayala, M. Callon, M. Arthur, J. P. Simorre, *Journal of the American Chemical Society* **2014**, *136*, 17852-17860;

g) V. Chevelkov, B. Habenstein, A. Loquet, K. Giller, S. Becker, A. Lange, *Journal of magnetic resonance* **2014**, *242*, 180-188.

[3] a) E. Barbet-Massin, A. J. Pell, J. S. Retel, L. B. Andreas, K. Jaudzems, W. T. Franks, A. J. Nieuwkoop, M. Hiller, V. Higman, P. Guerry, A. Bertarello, M. J. Knight, M. Felletti, T. Le Marchand, S. Kotelovica, I. Akopjana, K. Tars, M. Stoppini, V. Bellotti, M. Bolognesi, S. Ricagno, J. J. Chou, R. G. Griffin, H. Oschkinat, A. Lesage, L. Emsley, T. Herrmann, G. Pintacuda, *Journal of the American Chemical Society* **2014**, *136*, 12489-12497;

b) S. Q. Xiang, V. Chevelkov, S. Becker, A. Lange, *Journal of biomolecular NMR* **2014**, *60*, 85-90.

[4] a) R. Linser, B. Bardiaux, V. Higman, U. Fink, B. Reif, *Journal of the American Chemical Society* **2011**, *133*, 5905-5912;

b) M. J. Knight, A. L. Webber, A. J. Pell, P. Guerry, E. Barbet-Massin, I. Bertini, I. C. Felli, L. Gonnelli, R. Pierattelli, L. Emsley, A. Lesage, T. Herrmann, G. Pintacuda, *Angewandte Chemie* **2011**, *50*, 11697-11701.

[5] a) D. H. Zhou, G. Shah, M. Cormos, C. Mullen, D. Sandoz, C. M. Rienstra, *Journal of the American Chemical Society* **2007**, *129*, 11791-11801;

b) A. Marchetti, S. Jehle, M. Felletti, M. J. Knight, Y. Wang, Z. Q. Xu, A. Y. Park, G. Otting, A. Lesage, L. Emsley, N. E. Dixon, G. Pintacuda, *Angewandte Chemie* **2012**, *51*, 10756-10759;

c) M. Weingarth, E. A. van der Cruijsen, J. Ostmeyer, S. Lievestro, B. Roux, M. Baldus, *Journal of the American Chemical Society* **2014**, *136*, 2000-2007;

d) S. Wang, S. Parthasarathy, Y. Xiao, Y. Nishiyama, F. Long, I. Matsuda, Y. Endo, T. Nemoto, K. Yamauchi, T. Asakura, M. Takeda, T. Terauchi, M. Kainosho, Y. Ishii, *Chemical communications* **2015**.

[6] S. Asami, P. Schmieder, B. Reif, *Journal of the American Chemical Society* **2010**, *132*, 15133-15135.

[7] a) M. Huber, S. Hiller, P. Schanda, M. Ernst, A. Bockmann, R. Verel, B. H. Meier, *Chemphyschem : a European journal of chemical physics and physical chemistry* **2011**, *12*, 915-918;

b) T. Sinnige, M. Daniels, M. Baldus, M. Weingarth, *Journal of the American Chemical Society* **2014**, *136*, 4452-4455;

c) S. Wang, S. Parthasarathy, Y. Nishiyama, Y. Endo, T. Nemoto, K. Yamauchi, T. Asakura, M. Takeda, T. Terauchi, M. Kainosho, Y. Ishii, *PloS one* **2015**, *10*.

[8] a) M. K. Rosen, K. H. Gardner, R. C. Willis, W. E. Parris, T. Pawson, L. E. Kay, *Journal of molecular biology* **1996**, *263*, 627-636;

b) R. Otten, B. Chu, K. D. Krewulak, H. J. Vogel, F. A. Mulder, *Journal of the American Chemical Society* **2010**, *132*, 2952-2960;

c) D. Nand, A. Cukkemane, S. Becker, M. Baldus, *Journal of biomolecular NMR* **2012**, *52*, 91-101.

[9] D. H. Zhou, C. M. Rienstra, *Journal of magnetic resonance* **2008**, *192*, 167-172.

[10] M. Weingarth, G. Bodenhausen, P. Tekely, *Journal of magnetic resonance* **2009**, *199*, 238-241.

[11] M. J. Bayro, M. Huber, R. Ramachandran, T. C. Davenport, B. H. Meier, M. Ernst, R. G. Griffin, *The Journal of chemical physics* **2009**, *130*, 114506.

[12] M. Baldus, A. T. Petkova, J. Herzfeld, R. G. Griffin, *Mol Phys* **1998**, *95*, 1197-1207.

[13] a) M. Schubert, T. Manolikas, M. Rogowski, B. H. Meier, *Journal of biomolecular NMR* **2006**, *35*, 167-173;

b) P. Schanda, B. H. Meier, M. Ernst, *Journal of the American Chemical Society* **2010**, *132*, 15957-15967.

[14] R. Verel, M. Baldus, M. Ernst, B. H. Meier, *Chem Phys Lett* **1998**, *287*, 421-428.

[15] a) J. Ostmeyer, S. Chakrapani, A. C. Pan, E. Perozo, B. Roux, *Nature* **2013**, *501*, 121-124;

b) S. Uysal, L. G. Cuello, D. M. Cortes, S. Koide, A. A. Kossiakoff, E. Perozo, *Proceedings of the National Academy of Sciences of the United States of America* **2011**, *108*, 11896-11899;

c) E. A. van der Cruijsen, D. Nand, M. Weingarth, A. Prokofyev, S. Hornig, A. A. Cukkemane, A. M. Bonvin, S. Becker, R. E. Hulse, E. Perozo, O. Pongs, M. Baldus, *Proceedings of the National Academy of Sciences of the United States of America* **2013**, *110*, 13008-13013;

d) B. J. Wylie, M. P. Bhate, A. E. McDermott, *Proceedings of the National Academy of Sciences of the United States of America* **2014**, *111*, 185-190.

CHAPTER 3

The magnetic field dependence of cross-effect dynamic nuclear polarization under magic angle spinning

This chapter is based on the following publication:

D. Mance, P. Gast, M. Huber, M. Baldus, and K. L. Ivanov, "The magnetic field dependence of cross-effect dynamic nuclear polarization under magic angle spinning," *J. Chem. Phys.*, vol. 142, no. 23, p. 234201, Jun. 2015.

Introduction

Dynamic Nuclear Polarization (DNP) has become a popular method to boost Nuclear Magnetic Resonance (NMR) signals by orders of magnitude. To run DNP experiments it is usually necessary to dope the sample with an exogeneous paramagnetic polarizing agent and to exploit polarization transfer from the electronic to the nuclear spin reservoir via pumping of Electron Paramagnetic Resonance (EPR) transitions of the paramagnetic compound. Polarization stored in the electronic reservoir is much larger (a factor of γ_e/γ_n larger, where γ_e and γ_n are the electronic and nuclear gyromagnetic ratios, respectively), therefore DNP provides an efficient tool for increasing nuclear spin polarization. Since the signal intensity in magnetic resonance is directly proportional to nuclear spin polarization, DNP provides significant NMR signal enhancements. DNP methods are increasingly used in NMR spectroscopy [1, 2] and Magnetic Resonance Imaging [3, 4]; an important DNP application pioneered by Wind et al. [5, 6] and developed by the R. G. Griffin group [7] is MAS-DNP combining solid-state NMR detection under Magic Angle Spinning (MAS) conditions with DNP. MAS-DNP can be used for applications in material [8] and life sciences [9]. For example, low-temperature DNP under MAS has been used to study membrane-associated peptides [10, 11] as well as functionally relevant membrane protein states [12-15]. In addition, MAS-DNP has been successfully applied on cellular preparations [16-19].

Ideally, DNP studies, in particular, those related to MAS-DNP take place at high magnetic field strength where spectral resolution is maximized. This creates a problem for DNP because, while the NMR resolution is improved with the field, the DNP enhancement effect is expected to decrease [1]. Nonetheless, by using biradical paramagnetic dopants (instead of radicals) and relying on the cross-effect (instead of the solid-effect) it is possible to enhance NMR signals at 400 MHz by more than two orders of magnitude. Successful reports of DNP setup operating at 600 MHz and 700 MHz have appeared in the literature [20, 21] and, recently, the first results obtained at 800 MHz have been reported [14, 19]. These experiments demonstrated that the NMR spectral resolution can significantly improve compared to conducting DNP experiments at lower fields. However, the observed signal enhancements were smaller than expected from simple theoretical considerations on the basis of a static multi-spin system [1]. Hence, the theoretical description for understanding spin dynamics in MAS-DNP and, eventually, for optimizing the MAS-DNP performance at very high field should be improved. Specifically, the dependence of the DNP-derived signal enhancement (as well as the general polarization

transfer characteristics) on various experimental parameters should be taken into account. In this situation, the relevant experimental parameters are the microwave field strength, electron and nuclear spin relaxation rates, hyperfine and electron-electron dipolar coupling strengths as well as nuclear dipolar interactions. In addition, in MAS-DNP anisotropic magnetic interactions in solids are strongly modulated by fast sample spinning, which is a prerequisite for achieving high spectral resolution. Moreover, modulation of spin interactions changes the NMR signal even in the absence of microwave pumping [22]; spinning of the sample can also reduce the DNP effect as has been shown by Corzilius et al. [23]. Thus, an appropriate theoretical description should explicitly take these modulation effects into account and experimental parameters such as the electronic relaxation rates should be known at magnetic fields similar to conditions under which DNP experiments are performed.

Recently, Mentink-Vigier et al. [24] and independently Thurber and Tycko [22, 25] have developed a theoretical description of MAS-DNP in the cases of solid effect (when polarizing agents are radicals) and cross-effect (when polarizing agents are biradicals). In these works, the dependence of the MAS-DNP effect the MAS frequency, electron relaxation times, microwave field strength and frequency, electron-nuclear hyperfine interaction and electronic dipolar coupling strength was studied. Importantly, it has been revealed that under MAS conditions the DNP mechanism changes. The static DNP mechanisms require pumping of the forbidden double-quantum or zero-quantum transitions in the solid-effect case and fulfilling specific matching conditions in the cross-effect case. Under MAS conditions, nuclear polarization is generated in multiple passages through Level Anti-Crossings (LACs) during sample spinning. LACs are known [26, 27] to mediate efficiently polarization transfer in coupled spin systems. For instance, the cross-effect MAS-DNP is composed of two time-dependent LACs of the three-spin energy levels under MAS and microwave irradiation [22, 24, 25]. The first crossing, when the microwave frequency matches the EPR resonance frequency of one electron, reduces its polarization from the thermal equilibrium value, creating or altering the polarization difference between the electrons. The second LAC, when the difference of the EPR frequencies equals the NMR frequency, transfers some of the polarization difference between the two electrons to the nucleus. Additionally, there is a LAC corresponding to matching of the two electronic EPR frequencies, which results in redistribution of polarization in the electronic subsystem. Thurber and Tycko have also obtained analytical estimates for the spin mixing efficiency at LACs; an overview of these results can be found in Refs. [22]. It is also worth noting that in the static case only a very small fraction of the polarizing agents is excited by microwaves and contributes to

the DNP effect. In contrast, in spinning samples a much larger fraction of the paramagnetic agents is involved in the polarization process because they are excited by microwaves as the electron spin resonance condition is fulfilled for them during spinning. Thus, the previous theoretical treatment and experimental results [22-25, 28] show the pronounced effect of sample spinning on DNP formation.

The goal of this work is to study the dependence of MAS-DNP on relevant experimental parameters in order to (i) analyze the role of spin interactions and spin relaxation rates in the DNP formation and to (ii) explain the experimentally observed decrease of the enhancement at high magnetic field. In our analysis, we take sample spinning into account and investigate the magnetic field dependence of the DNP effect under MAS conditions. Our theoretical and numerical work is supported by experimental EPR studies that determined electron T_1 and T_2 relaxation times at 95 GHz and 275.7 GHz and DNP measurements conducted at both 400 MHz/263 GHz and 800 MHz/527 GHz.

Experimental methods and results

Samples were prepared using TOTAPOL [29] and AMUPol [30] as DNP agents. The biradical concentration of 1, 7 and 15 mM was used; as a solvent we used a D_8-glycerol/D_2O/H_2O mixture with a volume ratio of 60/30/10.

Solid-state NMR and DNP experiments were conducted using 3.2 mm triple-resonance (^1H, ^{13}C, ^{15}N) MAS probe heads at static magnetic fields of 9.4 and 18.8 T corresponding to the proton/electron resonance frequencies of 400 MHz/263 GHz and 800 MHz/527 GHz (Bruker BioSpin). Signal enhancements reported were used as published [31] or related to measurements in other biological systems such as the type-4 secretion complex (T4SScc) [19].

The EPR spectra at 275 GHz were recorded at 100 K, using a home-built spectrometer operating at 275.7 GHz [32, 33]. Field modulation amplitude was set to 0.2 mT at a frequency of 1.7 KHz. In Figure 3.1, EPR spectra measured at 275.7 GHz are shown for AMUPol [30] (A) and TOTAPOL [29] (B) with a biradical concentration of 15 mM in a D_8-glycerol/D_2O/H_2O mixture, volume ratio 60/30/10. The relaxation times T_{1e} and T_{2e} were obtained from inversion-recovery experiments (π-t-$\pi/2$-τ-π pulse sequence) and from spin echo decay experiments ($\pi/2$-t-π sequence), respectively, performed on the home-built 95 GHz and 275 GHz EPR spectrometers [34]. The time dependence of the T_1 and T_2 relaxation are presented in

Figure 3.2. In Table 3.1, the fit parameters of these measurements are given. The present data set suggests for TOTAPOL an increase in T_{1e} from 95 GHz EPR to values in the range of 100 µs at 275 GHz and a decrease in T_{2e} to the sub-microsecond regime at 275 GHz. For AMUPol, our data suggest a slight increase in T_{1e} and T_{2e} from 95 GHz to 275 GHz.

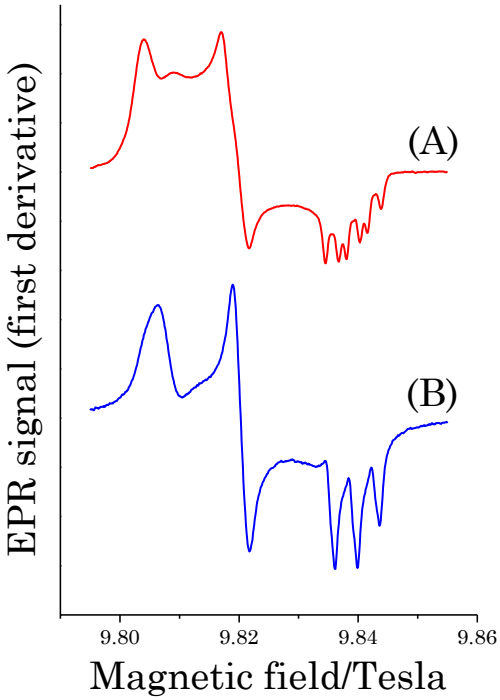

Figure 3.1. Continuous-wave 275 GHz EPR spectra at 100K for (A) AMUPol and (B) TOTAPOL. Both samples contained a biradical concentration of 15 mM in a solution of D_8-glycerol/D_2O/H_2O with a volume ratio of 60/30/10.

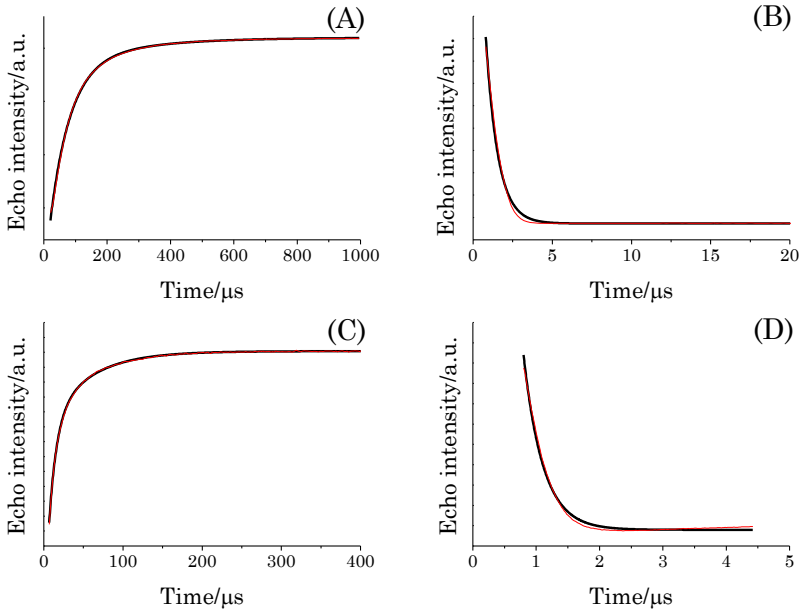

Figure 3.2. Determination of electronic relaxation parameters, T_{1e} and T_{2e} for AMUPol (A,B) and TOTAPOL (C,D) at 275 GHz using a biradical concentration of 15 mM in a D_8-glycerol/D_2O/H_2O with a volume ratio of 60/30/10. Thin (red) lines – (double) exponential fits; the fitting parameters are summarized in Table 3.1.

Compound	Relaxation parameter	95 GHz	275.7 GHz
TOTAPOL	T_{1e}/μs	50 (10)	9 (50)
	T_{2e}/μs	0.1 (0.4)	0.3
AMUPol	T_{1e}/μs	50 (160)	60 (230)
	T_{2e}/μs	0.7	0.8

Table 3.1. Relaxation parameters measured in our study for AMUPol and TOTAPOL by 95 GHz and 275 GHz EPR; the biradical is in a solution of D_8-glycerol/D_2O/H_2O with a volume ratio of 60/30/10. The relaxation parameters at 95 and 275 GHz have been measured using a biradical concentration of 15 mM at 100 K. The dominant component is specified, the values in parenthesis correspond to the second, less-pronounced, component in cases where fitting with a bi-exponential was necessary.

Theory

A. General description

Let us present the theoretical approach to the problem under study. We consider here cross-effect DNP, i.e., the spin system in our case comprises of two electrons, a and b, and N spin-1/2 nuclei. The solid-effect is usually very inefficient at high fields (as it requires very high microwave power to pump the forbidden EPR transitions) [1] and is not treated here. The Hamiltonian of such a system at high magnetic field B_0 and in the presence of the microwave field can be conveniently defined in the microwave rotating reference frame (in frequency units):

$$\begin{aligned}\hat{H}(t) = {} & \Delta\omega_a\hat{S}_{az} + \Delta\omega_b\hat{S}_{bz} + \sum_k \omega_n\hat{I}_{kz} + \omega_1\{\hat{S}_{ax}+\hat{S}_{bx}\} \\ & + D_{ab}\{2\hat{S}_{az}\hat{S}_{bz} - \hat{S}_{ax}\hat{S}_{bx} - \hat{S}_{ay}\hat{S}_{by}\} \\ & + \sum_k \{A_{zz,k}\hat{S}_{az}\hat{I}_{kz} + A_{zx,k}\hat{S}_{az}\hat{I}_{kx} + A_{zy,k}\hat{S}_{az}\hat{I}_{ky}\} \\ & + \sum_{k,m} d_{km}\{2\hat{I}_{kz}\hat{I}_{mz} - \hat{I}_{kx}\hat{I}_{mx} - \hat{I}_{ky}\hat{I}_{my}\}\end{aligned} \tag{3.1}$$

Here $\Delta\omega_{a,b} = \omega_{a,b} - \omega_{mw}$ is the electronic Zeeman interaction in the rotating frame ($\omega_{a,b}$ are the electronic Zeeman interactions in the laboratory frame, ω_{mw} is the microwave frequency); ω_n is the nuclear Zeeman interaction; ω_1 is the microwave field strength; D_{ab} is the electron-electron dipolar interaction; $A_{zz,k}$ is the secular hyperfine interaction (HFI) of the a-electron with the k-th nucleus; $A_{zx,k}$ and $A_{zy,k}$ are the corresponding pseudo-secular HFI terms; d_{km} is the dipole-dipole interaction between the k-th and m-th nuclei ($k, m = 1, \dots, N$). Other terms are not relevant at high magnetic fields. For the sake of simplicity, we here assume that the nuclei are coupled only to electron a. In rotating solids, all non-isotropic interactions are changing with time. To take this effect into account we calculate the time evolution of the electronic g-tensors, HFI and dipolar couplings during spinning. To do so, we assume arbitrary orientations of the biradical with respect to the rotor-fixed frame; the orientation of the Principal Axis System (PAS) of the g-tensor of the a-electron with respect to this frame is characterized by three Euler angles: $\{\alpha, \beta, \gamma\}$ (hereafter, following Mehring [35] we will always

give the Euler angles in the zyz-convention, i.e., we successively apply rotations by the angle α about the z-axis, by the angle β about the new y'-axis and by the angle γ about the new z''-axis). Then the interaction tensors are computed in the laboratory frame; the transition from the rotor-fixed frame to the lab frame is given by the following Euler rotation: $\{\omega_{MAS}t, \Theta_M, 0\}$; here ω_{MAS} is the MAS frequency and $\Theta_M = \arccos(1/\sqrt{3}) = 54.7°$ is the magic angle. Following Mentink-Vigier and coauthors [24] we assume a fixed geometry of the biradical; i.e., PAS_a and PAS_b (PASs of the two electronic g-tensors) have fixed orientation with respect to each other. The relative orientation of the vector connecting two radical centers (consequently, electronic dipolar coupling) is also fixed with respect to PAS_a. Such assumptions are consistent with the EPR data [36] for TOTAPOL. In our studies presented below, we always used the same orientation of the HFI tensor and nuclear dipolar interaction tensor with respect to PAS_a; in most cases, we specified the orientation of tensors of both kinds by the following sets of the Euler angles: $\{0, \pi/4, 0\}$ or $\{0,0,0\}$. We conducted calculations for each single orientation of PAS_a given by the $\{\alpha, \beta, \gamma\}$ sets of angles and then performed an averaging over the Euler angles. To calculate the time-dependent interactions we acted as follows. For instance, the g-tensor of the a-radical in the lab frame is:

$$\hat{g}_{a,lf}(t) = \hat{R}(\omega_{MAS}t, \Theta_M, 0)\hat{R}(\alpha, \beta, \gamma)\hat{g}_{a,pas}\hat{R}^{-1}(\alpha, \beta, \gamma)\hat{R}^{-1}(\omega_{MAS}t, \Theta_M, 0) \qquad (3.2)$$

Here $g_{a,pas}$ is the g-tensor in PAS_a; R is the Euler rotation matrix. Then the corresponding electron Zeeman interaction is expressed as:

$$\omega_a(t) = \{g_{a,lf}(t)\}_{zz}\beta B_0 \qquad (3.3)$$

where β is the Bohr magneton. Following Thurber and Tycko [25] we also added HFI of the electron spins with ^{14}N nuclei present in the radical center of nitroxide-based biradicals. Explicit expressions for $\omega_a(t)$ can be found, for instance, in Supplementary Materials of Ref. [25]. Other tensors and spin interactions can be calculated in a similar way. In addition to coherent spin dynamics in DNP it is necessary to take into account relaxation effects. To reduce the calculation time required for the calculation the full relaxation matrix $\hat{\hat{L}}$ (having a large dimensionality, for instance, 1024×1024 already for two electrons and three nuclei) we instead considered relaxation in the eigen-basis of the Hamiltonian $\hat{H}(t)$ at each instant of time

and left only the terms responsible for relaxation of state populations, i.e., $L_{ii,jj}$, and decay of coherences, i.e., $L_{ij,ij}$. These elements were computed in essentially the same way as shown previously [24, 25] at each instant of time because the eigen-states are time-dependent. For instance,

$$\begin{aligned} L_{ii,jj} &= \frac{f_{ij}}{T_{1e}}\left\{\left|\left(\hat{S}_{ax}\right)_{ij}\right|^2 + \left|\left(\hat{S}_{ay}\right)_{ij}\right|^2 + \left|\left(\hat{S}_{bx}\right)_{ij}\right|^2 + \left|\left(\hat{S}_{by}\right)_{ij}\right|^2\right\} \\ &+ \frac{f_{ij}}{T_{1n}}\sum_k\left\{\left|\left(\hat{I}_{kx}\right)_{ij}\right|^2 + \left|\left(\hat{I}_{ky}\right)_{ij}\right|^2\right\} \\ L_{ij,ij} &= \frac{1}{T_{2e}}\left\{\left|\left(\hat{S}_{az}\right)_{ii} - \left(\hat{S}_{az}\right)_{jj}\right|^2 + \left|\left(\hat{S}_{bz}\right)_{ii} - \left(\hat{S}_{bz}\right)_{jj}\right|^2\right\} \\ &+ \frac{1}{T_{2n}}\sum_k\left|\left(\hat{I}_{kz}\right)_{ii} - \left(\hat{I}_{kz}\right)_{jj}\right|^2 \end{aligned} \tag{3.4}$$

Here f_{ij} is the Boltzmann factor for the corresponding relaxation transition [24]; T_{1e} and T_{1n} are the longitudinal relaxation times of the electrons and the nuclei, respectively; T_{2e} and T_{2n} are the transverse electronic and nuclear relaxation times, respectively; all matrix elements are defined here in the eigenbasis of the Hamiltonian at the corresponding instant of time. When needed, the nuclear relaxation times can also be empirically corrected to take into account the presence of radical centers; furthermore, effect of sample spinning on the relaxation times can be included as has been done previously [37]. However, detailed consideration of such effects is beyond the scope of this work. The initial density matrix $\hat{\rho}_0$ describes two thermally polarized electrons and N thermally polarized nuclei; polarization of each spin is given by the corresponding Boltzmann factor, i.e., by $\hbar\gamma B_0/k_B T$ (here k_B is the Boltzmann constant and T is the absolute temperature). The numerical method of calculating spin evolution is described in the following subsection.

B. Numerical approach

Previously, there were two different methods suggested for calculating spin dynamics in MAS-DNP. Mentink-Vigier et al. [24] performed calculations in the Liouville space and calculated the evolution super-operator, $\hat{\hat{\Lambda}}_{ev}$, for a single rotor cycle of the duration $\tau_r = 2\pi/\omega_{MAS}$. In this situation, the evolution after N_c cycles can be computed by applying $\hat{\hat{\Lambda}}_{ev}$ to the initial density matrix N_c times. A disadvantage of such a method is that computing $\hat{\hat{\Lambda}}_{ev}$ is a relatively time consuming step because the dimensionality of this operator is very large. Thurber and Tycko [25] used a calculation method, which allows one to work in the Hilbert space (having a much smaller dimensionality); thus, spin evolution within a single rotor cycle could be calculated fast. At the same time, in their approach no evolution operator is introduced. Therefore the calculation the evolution after many cycles requires repeating the calculation procedure with small time steps. Consequently, for computing the stationary density operator after many cycles a lot of time is needed and this calculation method becomes slower than that proposed in Ref. [24] and requires running in parallel calculations for different orientations. Here, we used a method similar to that of Mentink-Vigier and co-authors [24] in order to gain from the possibility to go through the rotor cycle in N_s fine steps of a duration δt only once. For this purpose, we only slightly modified the procedure for evaluating the operator $\hat{\hat{\Lambda}}_{ev}$ to make the calculation less time-consuming. Specifically, we do not take explicitly the operation of computing the matrix exponent $\hat{\hat{\Lambda}}_n = \exp\left(\hat{\hat{R}}(t_n)\delta t\right)$ during the n-th time step; here $\hat{\hat{R}}(t_n)$ is the Liouville operator of the spin system at time t_n. In our method, we first set the evolution super-operator equal to the unity super-operator, $\hat{\hat{\Lambda}}_{ev} = \hat{\hat{E}}$, and then apply the following procedure for each step. First, for each time step, t_n, within the rotor cycle we diagonalize the Hamiltonian:

$$\hat{H}_d(t_n) = \hat{T}_n^{-1}\hat{H}(t_n)\hat{T}_n, \qquad E_i(t_n) = \left(\hat{H}_d(t_n)\right)_{ii} \tag{3.5}$$

Here $E_i(t_n)$ are the eigen-values of $\hat{H}(t_n)$ and $\hat{T}_n$ is a matrix composed of its eigen-vectors. Then the relaxation rates $W_{ij}(t_n) = L_{ii,jj}(t_n)$ and $R_{ij}(t_n) = L_{ij,ij}(t_n)$ (for $i \neq j$) and $W_{ii}(t_n) = -\sum_{j\neq i} W_{ji}\,(t_n)$ are computed. The rates $W_{ij}(t_n)$ constitute the matrix, $\hat{W}(t_n)$, of all transition rates; the rates $R_{ij}(t_n)$ give the decay of spin coherences. Afterwards, we introduce the following elements of $\hat{\hat{\Lambda}}_n$, as defined in the eigen-basis of $\hat{H}(t_n)$:

$$\left(\hat{\hat{\Lambda}}_{n,eb}\right)_{ii,jj} = \left(\exp\left(\hat{W}(t_n)\delta t\right)\right)_{ij}; \tag{3.6}$$

$$\left(\hat{\hat{\Lambda}}_{n,eb}\right)_{ij,ij} = \exp\left(i\{E_j(t_n) - E_i(t_n)\}\delta t - R_{ij}(t_n)\delta t\right)$$

These parameters are the only non-zero matrix elements in the eigenbasis. An advantage of this method is that all operations are performed without introducing $\hat{\hat{\Lambda}}_n$ explicitly. Since this is an operator with a very large number of elements, each operation explicitly performed with $\hat{\hat{\Lambda}}_n$ requires a lot of random-access memory. In our method this problem is avoided as much as possible. The only operation performed with large matrices is transformation of $\hat{\hat{\Lambda}}_{n,eb}$ to the original basis:

$$\hat{\hat{\Lambda}}_n = \hat{\hat{S}}_n \hat{\hat{\Lambda}}_{n,eb} \hat{\hat{S}}_n^{-1}, \qquad \text{where} \qquad \hat{\hat{S}}_n = \hat{T}_n \otimes \hat{T}_n \tag{3.7}$$

This is the most time-consuming step in our algorithm; nevertheless, it is still reasonably fast because all operations represent straightforward matrix multiplications. Thus, advantages of our method are: (i) non-zero elements of $\hat{\hat{\Lambda}}_n$ in the eigen-basis are calculated very quickly by avoiding operations with large matrices and (ii) transition from one basis to another is done only once per each step. With this algorithm we are able to make the calculation for single orientation of the system in about 1,000 seconds taking $1{,}25\times10^6$ steps per rotor cycle using a home-written Matlab code and a standard desktop computer (Intel core i5 at 3.5 GHz). The total evolution operator is given by the product of evolution operators for all individual steps:

$$\hat{\hat{\Lambda}}_{ev} = \hat{\hat{\Lambda}}_1 \hat{\hat{\Lambda}}_2 \ldots \hat{\hat{\Lambda}}_{N_s} \tag{3.8}$$

Typically, we take $N_c \ll N_s$; thus, most time is used to calculate $\hat{\hat{\Lambda}}_{ev}$, whereas propagation through subsequent rotor cycles is much faster. The density matrix changes in the following way within each rotor cycle:

$$\rho \rightarrow \hat{\hat{\Lambda}}_{ev}\hat{\rho} \tag{3.9}$$

After N_c cycles the density matrix is as follows:

$$\hat{\rho}(N_c\tau_r) = \hat{\rho}(2\pi N_c/\omega_{MAS}) = \left(\hat{\hat{\Lambda}}_{ev}\right)^{N_c}\hat{\rho}_0 \tag{3.10}$$

With this method we obtain the density matrix at the end of each rotor cycle and do not trace spin evolution during the cycle. This is acceptable because the DNP effect typically does not build up significantly within only one rotor cycle. In the case that spin evolution during the rotor cycle is of interest (for instance, for revealing the effects of LACs) it is straightforward to perform such a calculation by using our approach or any of the ones [24, 25] employed earlier. The expectation values of all spin operators, $\hat{F}$, are be calculated from $\hat{\rho}(N_c\tau_r)$ in the usual way by taking the trace operation: $\langle F\rangle = \mathrm{Tr}\{\hat{F}\hat{\rho}\}$. We compute the net magnetizations of all spins, i.e., $\langle S_{az}\rangle$, $\langle S_{bz}\rangle$ and $\langle I_{kz}\rangle$ and their time dependences. Polarization of the nuclear spins is related to the thermal nuclear polarization to obtain the enhancement factors, ε_k. In many cases we discuss the stationary nuclear polarizations, P_k (defined as $\langle I_{kz}\rangle \xrightarrow{t\to\infty} P_k$), and relate them to thermal electronic polarization, P_e, to obtain the stationary DNP enhancement factor, ε_{DNP}, as $\varepsilon_{DNP} = P_k/P_{eq}$ with P_{eq} being the nuclear spin polarization at equilibrium conditions. The outlined calculation scheme has been implemented in Matlab; the program can be obtained upon request from the authors. When running calculations, we carefully checked that the time step δt was sufficiently small so that the results do not depend on δt anymore.

Results

In Figure 3.3 we calculated the DNP effect at 400 MHz (A) and 800 MHz (B) with magnetic field sweep around 400 and 800 MHz, respectively. In line with previous theoretical studies [25] we find a bimodal shape, typical for cross-effect DNP where the positive and negative components correspond to the different matching conditions, $(\omega_a - \omega_b) = \pm\omega_n$. Hereafter, for the sake of clarity, we always performed calculations at microwave frequency and field strength corresponding exactly to the positive maximum. With the parameters chosen, the maximal polarization of the nucleus is ± 0.56 (at 400 MHz) and ± 0.39 (at 800 MHz) of the electron spin polarization, resulting in the maximal calculated enhancement of about 370 and

260, respectively. The values obtained by the calculation shown in Figure 3.3 are considerably higher than those usually found experimentally; the reason for this is given below.

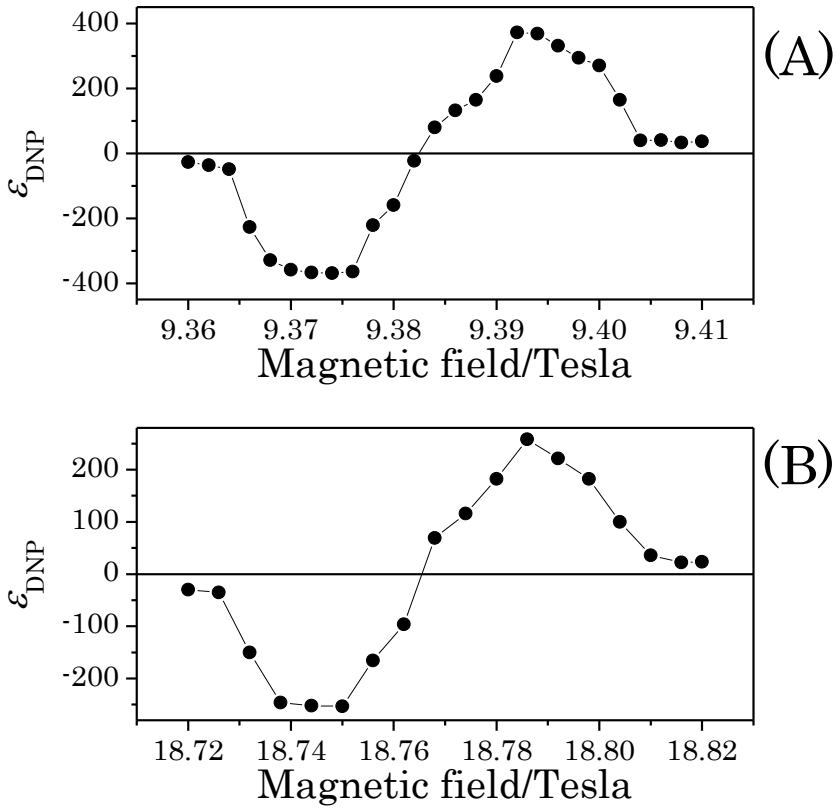

Figure 3.3. Calculated MAS-DNP effect with a field sweep around 400 MHz (B_0=9.4 T, A) and 800 MHz (B_0=18.8 T, B), which show a typical field profile expected for a nitroxide-based biradicals. Simulations were performed using a three spin model (two electrons and one nucleus, e-e-n) with averaging over 343 orientations and using a HFI of 3 MHz, the electronic dipole-dipole coupling is D_{ab} =23 MHz, T_{1e}=1 ms, T_{2e}=1 μs, T_{1n}=1 s.

Similar to the results shown in Figure 3.3, previous studies of MAS-DNP at high fields have revealed a decrease in the DNP effect, which is, however, much smaller than that found experimentally: Thurber and Tycko have found [25] a decrease in the enhancement, ε_{DNP}, of about 20% upon going from 9.4 T (400 MHz proton NMR frequency) to 18.8 T (800 MHz proton NMR frequency) at relatively strong microwave field strength, $\omega_1/2\pi$, of 2 MHz. For

a smaller microwave field strength of 80 kHz a decrease of about 50% has been reported. Such a decrease does not agree with that found experimentally upon increasing the field: the experimentally observed decrease in ε_{DNP} is, thus far, significantly larger, see below. Here, to account for the experimentally observed decrease we propose to consider the following factors: (i) HFI values should be limited only to those corresponding to nuclei outside the "core" around the electrons (vide infra) and (ii) DNP build-up time should be treated as an important factor, which affects the resulting enhancement. Let us explain these two assumptions in more detail. In solid-state DNP, polarization transfer from electrons polarizes only a limited fraction of nuclei, namely, those located near the electrons so that the electron-nuclear HFI is operative [39, 40]. The rest of the nuclei in the sample are polarized due to the nuclear spin diffusion. It is well known, that the nuclei closest to the electron are polarized most quickly and efficiently and $P_k \sim P_e$ can be achieved for them; however, their NMR signals cannot be detected due to strong paramagnetic effects; moreover, they do not contribute to polarization of the sample. The reason for that is that nuclear spin diffusion is operative between the k-th and m-th nuclear spins when the dipolar coupling, d_{km}, is larger than or comparable to the difference, $\delta\omega_{km}$, in their NMR frequencies. For the nuclei located very close to the electrons the paramagnetic shift of NMR lines results in $\delta\omega_{km} \gg d_{km}$ and suppresses spin diffusion. Consequently, to polarize the sample it is required to polarize the nuclei at the "edge" of the "core" around the electrons (for such nuclei $\delta\omega_{km} \approx d_{km}$) and to rely on nuclear-nuclear polarization transfer by spin diffusion. As a result, the build-up times of the observed DNP effect is much longer than the build-up time of the DNP for the core nuclei, which are not detected. Detailed studies of polarization transfer in systems with several nuclear spins in the static case has been performed by Hovav et al. [41]. When the build-up times are comparable to the nuclear T_1-relaxation times the existence of the "spin diffusion barrier" limits the DNP enhancement: when the build-up is slow nuclear spin polarization will be saturated at $t \sim T_{1n}$ and maximal theoretically expected enhancement will not be reached. Previously, Thurber and Tycko [25] and also Mentink-Vigier et al. [24] assumed rather strong HFI of at least a few MHz, whereas a HFI (dipolar coupling of the electron and proton spins) of 3 MHz corresponds to an electron-nuclear distance of about 3 Å, i.e., to the "core" nuclei. By running calculations for four-spin systems, two electrons and two protons, and assuming the proton-proton distance of 3 Å we have found that nuclear spin diffusion becomes operative only at electron-nuclear distances of about 10 Å (see Figure 3.4).

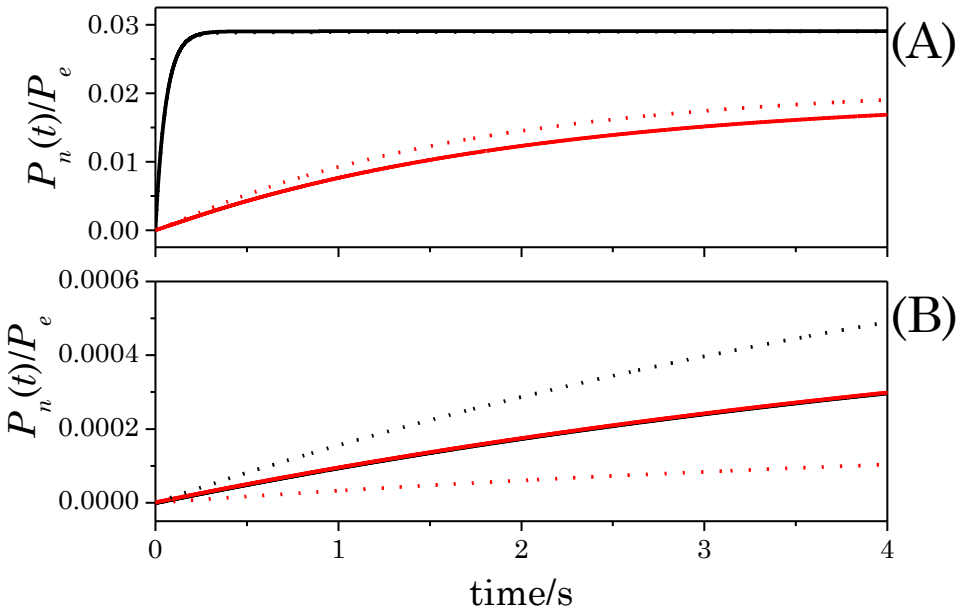

Figure 3.4. Buildups of nuclear spin magnetization (normalized to the equilibrium electron polarization) for nucleus 1 (black curves) and nucleus 2 (red curves) at magnetic field of 9.395 Tesla for different distances between the electron and the nuclei. Solid lines give the calculation result for the coupling, which corresponds to the inter-nuclear distance of 3 Å and dotted lines give the calculation result for zero nuclear dipole-dipole coupling. Results are shown for a single sample orientation. The electron-nuclear distances are $r_{e1n1} = 2$ Å and $r_{e1n2} = 2$ Å (A) and $r_{e1n1} = 10$ Å and $r_{e1n2} = 13$ Å (B).

At such distances the HFI is considerably lower, namely, it is only 0.08 MHz. Such HFI values result in slower DNP build-up times and, consequently, in a decrease of the DNP effect itself. In solid-state DNP, electron spectral diffusion originating from inter-molecular electron-electron dipolar couplings is also of great importance: at high concentration of paramagnetic species such processes become efficient changing the DNP mechanism from solid-effect or cross-effect to the so-called thermal mixing, which is described in using thermodynamic arguments, specifically, heat exchange between different spin reservoirs [42]. Recently Hovav et al. [43] have shown by double-resonance EPR experiments that in the presence of spectral diffusion a significant part of the EPR line can be excited by microwave irradiation: this has a strong effect on the DNP enhancement. However, in the present work we neglect electron

spectral diffusion because we are working at lower concentrations of paramagnetic species and also higher fields and higher temperature: at such conditions the spectral diffusion process is expected to be less efficient. Extension of our treatment to account for this process is a separate task, which is beyond the scope of the present work.

Parameter	**Value**
Microwave frequency, $\omega_m/2\pi$	263.45 GHz or 526.9 GHz
Microwave strength, $\omega_1/2\pi$	0.85 MHz
^{1}H NMR frequency, $\omega_n/2\pi$	400 MHz or 800 MHz
Temperature	100 K
MAS frequency, $\omega_r/2\pi$	8 kHz
Electron dipolar coupling, D_{ab}	35 MHz
HFI	0.08 MHz
g-tensor principal values	2.00614, 2.00194, 2.00988
^{14}N HFI principal values	18.8, 92.4, 18.2 MHz
T_{1e}	60 µs
T_{2e}	770 ns
T_{1n}	2 s
T_{2n}	1 ms

Table 3.2. Typical parameters used in simulation. Unless specified otherwise, these parameters were used to calculate the MAS-DNP effect.

The effect of HFI is demonstrated by Figure 3.5, typical parameters of our calculations from here on are given in Table 3.2. In this calculation, we changed B_0 and ω_{mw} proportionally ensuring that for any magnetic field the DNP effect as a bimodal function of the field swept around B_0 and that the DNP enhancement is determined on top of the positive field component. Lower HFI values result is slower build-ups; when the build-up is fast (i.e., when HFI is the highest, see Figure 3.5 [38]) the stationary nuclear polarization, P_n, reaches about 0.4 of the P_e value, see Figure 3.5a. However, when the build-up times are longer than or comparable to T_{1n} the stationary enhancement, ε_{DNP}, significantly decreases; the field dependence of the build-up rate is shown in Figure 3.5b.

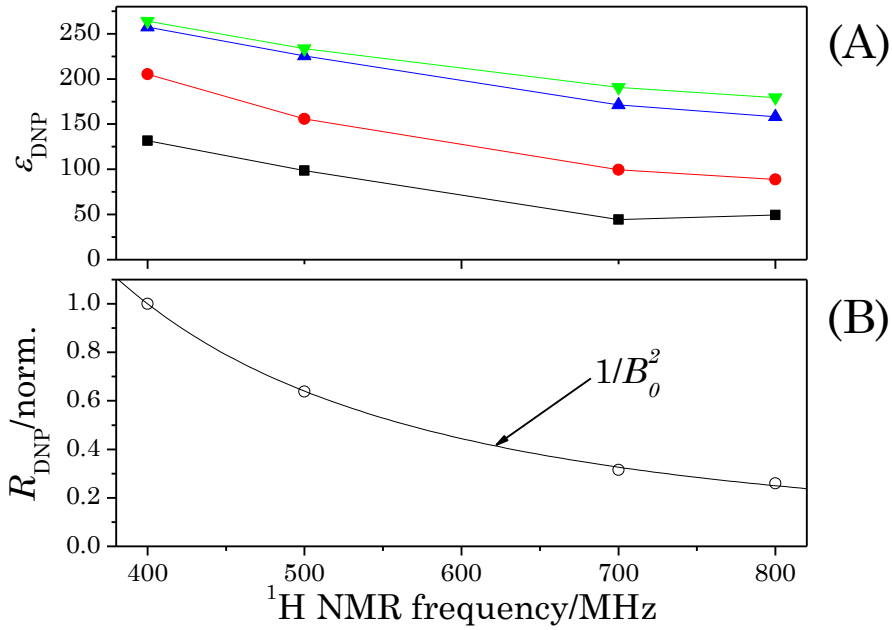

Figure 3.5. (A) Calculated MAS-DNP field dependence with different HFI values: 0.023 MHz (black squares), 0.08 MHz (red circles), 0.632 MHz (blue up-triangles) and 3 MHz (green down-triangles) using a three-spin model (e-e-n). The magnetic field was varied from 400 to 800 MHz with the following parameters: T_{1n}=2 s, T_{2n}=1 ms, T_{1e}=60 µs, T_{2e}=0.77 µs, D_{ab}=35 MHz; results are averaged over 125 orientations. (B) shows the field dependence of the normalized DNP build-up rates following approximately the $1/B_0^2$ law.

There is a strong decrease of the build-up rate upon the field increase from 400 to 800 MHz, accompanied by the decrease in the enhancement. Consequently, whereas for the nuclei close by the electrons the stationary enhancement, ε_{DNP}, reduces with the field by a factor of 1.5 (which is in agreement with the result of Thurber and Tycko [25]); for more remote nuclei we find a decrease by a factor of up to 2.7 for the enhancement. As has been explained above these are the nuclei at the edge of the core, which contribute to the overall enhancement. These findings therefore suggest that a separation of the "core" nuclei and "bulk" nuclei is important for understanding the decrease of the DNP efficiency at higher fields. Thus, at large HFI, i.e., for the "core" nuclei, there is only a rather moderate decrease of ε_{DNP} with the field. However, when more remote nuclei are considered, the decrease becomes stronger. Thus, the build-up rates are of importance for the observed MAS-DNP effects. This idea has been supported by

earlier experiments [14]: a strong correlation was found between the experimentally observed enhancement and the DNP build-up rate.

The DNP effect is sensitive not only to the static field strength and HFI but also to other interactions and relaxation times. Figures 3.6 and 3.7 show the theoretically the predicted MAS-DNP effect as a function of the static magnetic field at variable T_{1e} (see Figure 3.6) and electron-electron dipolar coupling, D_{ab} (see Figure 3.7). The DNP effect is reduced at shorter T_{1e} times; the normalized enhancement decreases with the field in a similar way for different T_{1e} values, see Figure 3.6. The decrease of the enhancement is due to the lower degree of EPR saturation at shorter T_{1e}; however, one should note that in the presence of EPR spectral diffusion opposite behaviour can be observed as reported by Lumata et al. [44] and reproduced theoretically by Colombo Serra et al. [45]. The DNP effect is also sensitive to the D_{ab} value. The dependence is not very pronounced at 400 MHz when the enhancement is high; however, it becomes significant when the magnetic field increases and ϵ decreases: at 800 MHz the DNP effect is considerably smaller for D_{ab}=20 MHz than for 55 MHz. The normalized field dependence shows that for higher D_{ab} the DNP effect is not only higher at any field strength but it also decreases slower, see Figure 3.7.

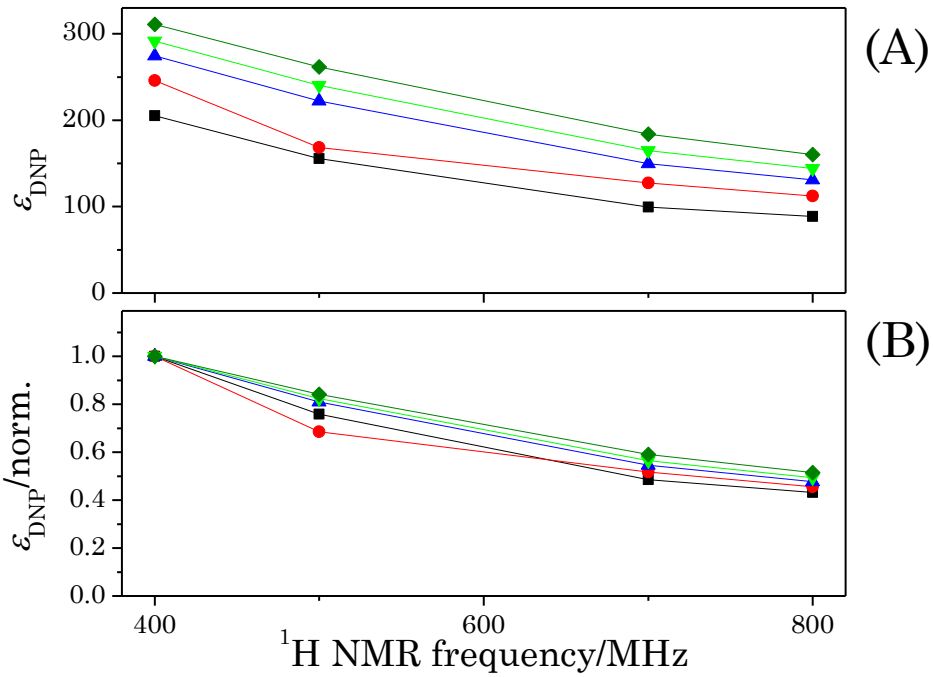

Figure 3.6. MAS-DNP field dependence using a three spin model (e-e-n) and averaging over 125 orientations with the following parameters: HFI is 0.08 MHz, T_{1n}=2 s, T_{2n}=1 ms, T_{2e}=0.77 µs, D_{ab}=35 MHz and different T_{1e} values: 60 µs (black squares), 100 µs (red circles), 150 µs (blues up-triangles), 200 µs (green down-triangles) and 300 µs (dark-green diamonds) while varying the magnetic field from 400 to 800 MHz. (A) shows the data with respect to the thermal nuclear polarization and in (B) each curve is normalized to the enhancement at 400 MHz and the change can be seen with respect to the increase in the magnetic field.

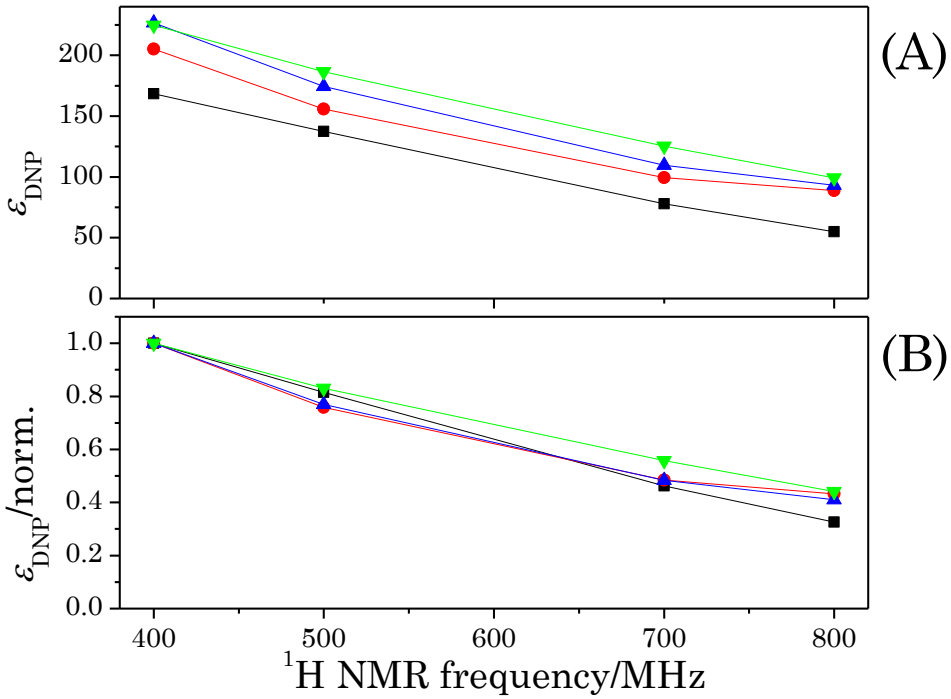

Figure 3.7. MAS-DNP field dependence averaged over 125 orientations using a three spin model (e-e-n) with the following parameters: HFI is 0.08 MHz, T_{1n}=2 s, T_{2n}=1 ms, T_{1e}=60 µs T_{2e}=0.77 µs; different D_{ab} values are used: 20 MHz (black squares), 35 MHz (red circles), 45 MHz (blue up-triangles) and 55 MHz (green down-triangles). The magnetic field was varied from 400 to 800 MHz. (A) shows the data with respect to the thermal nuclear polarization and in (B) each curve is normalized to the enhancement at 400 MHz and the change can be seen with respect to the increase in the magnetic field.

In DNP, an important issue is the dependence of the enhancement on the microwave field strength. Figure 3.8 shows the dependence of the DNP enhancement on ω_1 for 400 and 800 MHz. In both cases, the DNP effect increases with ω_1 reaching saturation at the microwave field of approximately 2 MHz. These results are in qualitative agreement with those reported by Thurber and Tycko [25]; quantitative comparison here is not possible because we used considerably shorter T_{1e} times. In general, limited microwave field strength available in experiments can reduce the DNP-derived signal enhancement: a recent work by Kubicki et al. [46] shows that improvement of dielectric properties of solid DNP samples by adding solid particles can significantly amplify the microwave field in the sample and, consequently,

increase the DNP effect. Such ω_1 effects are expected when the electron spin system has not reached saturation, see Figure 3.8. In our calculations, ω_1 is 0.85 MHz in most cases, i.e., the saturation is not yet reached, therefore increasing ω_1 can be of importance for systems with parameters close to those taken in the calculation.

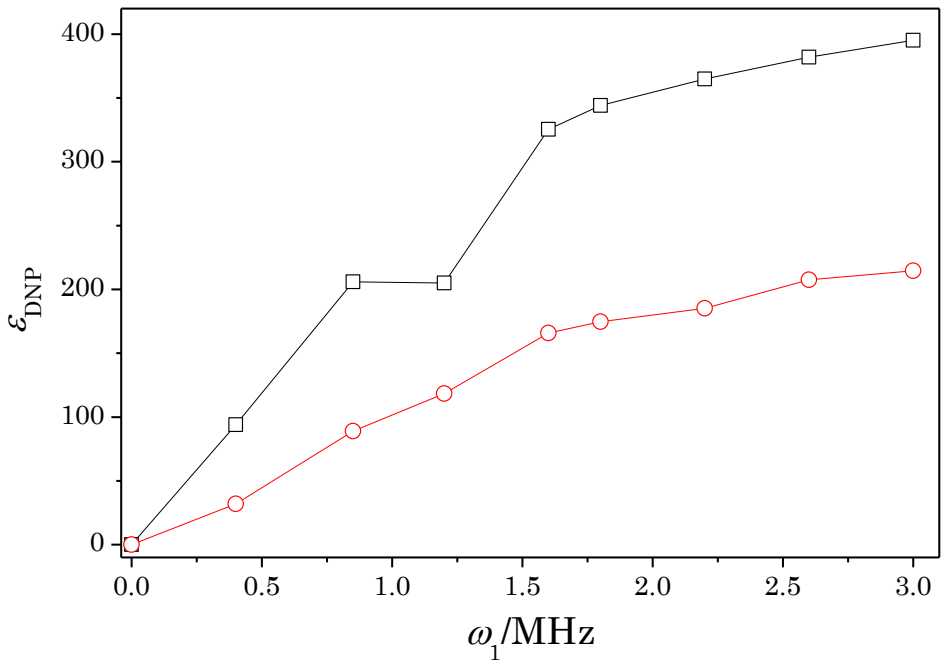

Figure 3.8. MAS-DNP dependence on the microwave field strength, ω_1, averaged over 125 orientations using a three spin model (e-e-n) with the following parameters: HFI is 0.08 MHz, D_{ab}=35 MHz, T_{1n}=2 s, T_{2n}=1 ms, T_{1e}=60 µs T_{2e}=0.77 µs. The results are shown for the 400 MHz (black squares) and 800 MHz (red circles) magnetic field.

Discussion

It is of interest to discuss the dependence of the DNP effect on various parameters. To do so, we will use the results of Thurber and Tycko who estimated [25] the spin mixing efficiency originating from LACs of each kind. Thus, the mixing efficiency for the LAC corresponding to the single-quantum EPR transition (when the microwave frequency matches the splitting of the EPR lines) is

$$P_e \approx \frac{\pi\omega_1^2}{2\frac{\partial\omega_e}{\partial t}} \tag{3.11}$$

The mixing efficiency at the three-spin LAC, which leads to polarization transfer to the nucleus, is

$$P_{triple} \approx \frac{\pi D_{ab}^2\left(A_{zx}^2 + A_{zy}^2\right)}{2\omega_n^2\frac{\partial(\omega_a - \omega_b)}{\partial t}} \tag{3.12}$$

The mixing efficiency, P_{ee}, for the third LAC is expected to be close to 1 for typical experimental parameters. In these equations the time derivatives are originating from the MAS dependence. Thus, one sees that P_e is inverse proportional to B_0, while P_{triple} is proportional to $1/B_0^3$ [25] because each of the quantities $\omega_a, \omega_b, \omega_n$ is proportional to the field. The values of P_e, P_{triple} and P_{ee} significantly affect the DNP build-up rate, R_{DNP}, and, consequently, the stationary DNP value. For high DNP efficiency, i.e., for the "core" nuclei, which are polarized efficiently over a very wide field range, the enhancement at $t \to \infty$ is close to $\pm\gamma_e/\gamma_n$ and the actual dependence of P_e and P_{triple} on the relevant parameters (HFI, electronic g-tensor anisotropy, D_{ab}, B_0 and ω_1) does not play a significant role for the resulting enhancement. However, for the bulk nuclei, as discussed about, the enhancement depends on the build-up rate, which, in turn, is strongly affected by these parameters. If we assume that spin mixing at the three-spin LAC is the bottleneck of the DNP process the rate R_{DNP} is given by the product of P_{triple} (the mixing efficiency per rotor cycle) and the MAS frequency (the frequency of passages through the LACs): $R_{DNP} \sim P_{triple} \times \omega_{MAS}$. The enhancement then can be estimated as:

$$\varepsilon_{DNP} \sim R_{DNP} T_{1n} \frac{\gamma_e}{\gamma_n} \sim P_{triple} \omega_{MAS} T_{1n} \frac{\gamma_e}{\gamma_n} \tag{3.13}$$

In this situation we obtain that that ε_{DNP} is proportional to $1/B_0^3$. In our calculation, the B_0 dependence decreases slower than $1/B_0^3$, approximately as $1/B_0^2$, see Figure 3.5b. There are two main reasons for this. First, in the above expression for ε_{DNP} we considered only P_{triple} whereas the DNP effect also depends on P_e, which decreases slower, only as $1/B_0$. Second, in this estimate we have neglected electron spin relaxation effects. As a result, the field dependence of ε_{DNP} is in between the $1/B_0$ and $1/B_0^3$ behaviours.

Now let us compare theoretical results with experimental data available for three experimental systems. We considered the amino-acid proline, the membrane-embedded ion channel KcsA [14, 47] and T4SScc embedded in the cellular envelope [19]. For these systems, DNP enhancements have been measured at 400 MHz and also at higher magnetic fields, namely, at 600 MHz for Proline and at 800 MHz for Proline (unpublished results), KcsA and T4SScc. The three systems are rather different in their properties (i.e., relaxation times), therefore to perform the comparison we show normalized DNP enhancements: henceforth, the enhancement measured at 400 MHz is set to one and the enhancement at higher magnetic field strength is normalized to that at 400 MHz, i.e., the value $\varepsilon_{DNP}(B_0)/\varepsilon_{DNP}(400\ \text{MHz})$ is plotted. The results are shown in Figure 3.8. The experimentally measured enhancement decreases with the field faster than $1/B_0$: the ratio $\varepsilon_{DNP}(800\ \text{MHz})/\varepsilon_{DNP}(400\ \text{MHz})$ is approximately equal to 0.3. One can readily see that taking a large HFI value in the calculation such a decrease of the enhancement cannot be reproduced. Thus, taking the HFI value of 3 MHz (corresponding to the electron-proton distance of 3 Å) and 0.63 MHz (corresponding to the electron-proton distance of 5 Å) one cannot simulate the experimentally observed field dependence of the MAS-DNP effect. This is because the large HFI values and smaller electron-proton distances correspond to the core nuclei, whereas in experiments NMR signals only of the bulk nuclei can be assessed. To analyze the enhancement for the bulk nuclei one has to reduce the HFI value so that it corresponds to larger electron-nuclear distances, approximately, of 10 Å (so that HFI is 0.08 MHz) or more. Figure 3.9 shows that this assumption provides good agreement between experimental and calculation results, see the calculation results with HFI of 0.08 MHz and 0.023 MHz.

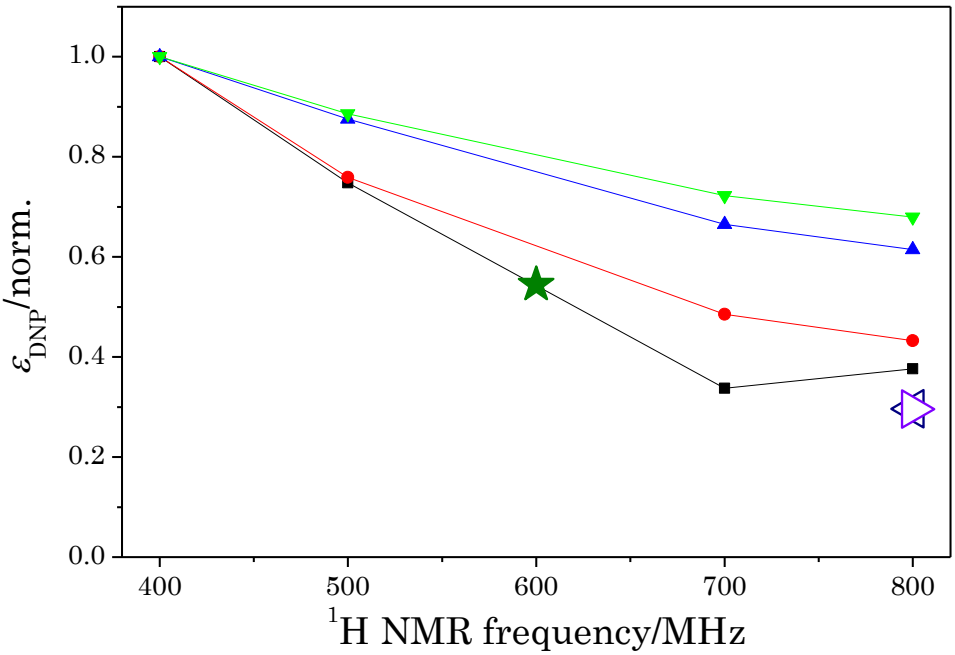

Figure 3.9. Comparison between calculations and experimental data. Experimental data are shown for Proline (enhancement from Ref. [20] is used), T4SS and KcsA that were recorded with both the 400 MHz and 800 MHz spectrometer at 100 K is shown. The theoretical enhancements at variable magnetic field are shown for different HFI values: 0.023 MHz (black squares), 0.08 MHz (red circles), 0.632 MHz (blue up-triangles) and 3 MHz (green down-triangles). Experimental enhancements are given for Proline (star), T4SS (left-triangle) and KscA (right-triangle). To enable comparison between theory and experiments for different systems the data are normalized to the enhancement at 400 MHz.

Indeed, taking lower HFI values one can reproduce the experimentally observed decrease in the enhancement upon increasing magnetic field. Thus, we believe that the key to explaining the field dependence of the MAS-DNP effect is to (i) clearly distinguish between the core and bulk nuclei and (ii) take into account the finite build-up time of the nuclear polarization by putting reasonable T_{1n} relaxation times in the calculation. Since the spin dynamics behind the MAS-DNP is complicated, a prerequisite for modelling experimental results is running rigorous quantum-mechanical calculations, which explicitly take into account the relevant magnetic interactions, spin relaxation and the effects of sample spinning.

Conclusions

In this work, we have performed a simulation of the field dependence of the MAS-DNP. Our calculation method follows closely the ones proposed earlier [24, 25] and it models the spin dynamics of a system of two electron spins and several nuclear spins in the presence of microwave pumping and sample spinning. The DNP study is supported by the first EPR investigation of the TOTAPOL and AMUPol biradicals at 9.4 T and measurement of their electronic spin relaxation times; thus, in the calculation, we have taken as many parameters known as it is possible. We have calculated the field dependence of the MAS-DNP effect systematically varying the HFI, electronic dipolar coupling and electronic T_1-relaxation time. In addition to the steady-state enhancement we have analyzed the build-up rate of the DNP effect and have found a correlation between the DNP enhancement and the DNP build-up rate. Furthermore, we have demonstrated the necessity of separating the core and bulk nuclei: only the enhancement of the latter should be analyzed and compared with experimental data on MAS-DNP. For the bulk nuclei, the DNP build-ups are considerably slower than for the core nuclei resulting in lower actual enhancement.

With these assumptions, the calculated DNP enhancements reasonably well reproduce the experimentally observed ones. In particular, the MAS-DNP effect rapidly decreases with the field, namely, faster than $1/B_0$, the law usually expected [1] for static DNP. This behaviour can be reproduced for the bulk nuclei by our calculation.

The analysis of the dependence of the MAS-DNP effect on various parameters shows that for increasing the enhancement it is desirable to work with biradicals with (i) slower electronic relaxation rates and (ii) stronger electronic dipolar coupling. Our calculations show that the longer T_{1e} is and the stronger D_{ab} is the larger is the enhancement. Moreover, for larger D_{ab} the decrease of the DNP effect with the magnetic field is slower. Thus, for improving the performance of MAS-DNP it is desirable to design and exploit biradical dopants with slow electronic relaxation rates and strong electronic dipolar coupling. In both aspects, AMUPol is a better radical than TOTAPOL; the higher DNP enhancements obtained with AMUPol are in accordance with this [30]. As far as optimizing the performance of high-field DNP is concerned, a promising direction to go would be using biradicals with hybrid structure, which have different relaxation rates for the two radical moieties. Calculations for the static case predict stronger DNP enhancement for such biradicals [48]; thus, it is of interest to examine theoretically and experimentally whether such paramagnetic dopants improve the performance of MAS-

DNP. In summary, we were able to reproduce theoretically the observed magnetic field dependence of the MAS-DNP effect and to model the decrease of the enhancement at high fields found experimentally. This work contributes to a systematic study of the influence of electron-electron, electron-nuclear and nuclear-nuclear polarization transfer in MAS-DNP experiments. We anticipate that such a study will enable elucidating the key parameters responsible for the DNP enhancement and, eventually, optimizing the performance of the DNP technique in solid-state NMR.

References

[1] T. Maly, G. T. Debelouchina, V. S. Bajaj, K.-N. Hu, C.-G. Joo, M. L. Mak-Jurkauskas, J. R. Sirigiri, P. C. A. van der Wel, J. Herzfeld, R. J. Temkin, and R. G. Griffin, J. Chem. Phys. **128**, 052211 (2008).

[2] C. Griesinger, M. Bennati, H.-M. Vieth, C. Luchinat, G. Parigi, P. Hofer, F. Engelke, S. J. Glaser, V. Denysenkov, and T. F. Prisner, Prog. Nucl. Magn. Reson. Spectr. **64**, 4 (2012).

[3] J. H. Ardenkjaer-Larsen, B. Fridlund, A. Gram, G. Hansson, L. Hansson, M. H. Lerche, R. Servin, M. Thaning, and K. Golman, Proc. Natl. Acad. Sci. U. S. A. **100**, 10158 (2003).

[4] F. A. Gallagher, M. I. Kettunen, S. E. Day, D.-E. Hu, J. H. Ardenkjaer-Larsen, R. in't Zandt, P. R. Jensen, M. Karlsson, K. Golman, M. H. Lerche, and K. M. Brindle, Nature **453**, 940 (2008).

[5] M. J. Duijvestijn, R. A. Wind, and J. Smidt, Physica B **138**, 147 (1986).

[6] R. A. Wind, M. J. Duijvestijn, C. van der Lugt, A. Manenschijn, and J. Vriend, Prog. Nucl. Magn. Reson. Spectrosc. **17**, 33 (1985).

[7] D. A. Hall, D. A. Maus, G. J. Gerfen, S. J. Inati, L. R. Beccera, F. W. Dahlquist, and R. G. Griffin, Science **276**, 930 (1997).

[8] A. J. Rossini, A. Zagdoun, M. Lelli, A. Lesage, C. Copéret, and L. Emsley, Acc. Chem. Res. **46**, 1942 (2013).

[9] Q. Z. Ni, E. Daviso, T. V. Can, E. Markhasin, S. K. Jawla, T. M. Swager, R. J. Temkin, J. Herzfeld, and R. G. Griffin, Acc. Chem. Res. **46**, 1933 (2013).

[10] E. Salnikov, M. Rosay, S. Pawsey, O. Ouari, P. Tordo, and B. Bechinger, J. Am. Chem. Soc. **132**, 5940 (2010).

[11] E. J. Koers, M. P. Lopez-Deber, M. Weingarth, D. Nand, D. T. Hickman, D. M. Ndao, P. Reis, A. Granet, A. Pfeifer, A. Muhs, and M. Baldus, Angew. Chem. Intl. Ed. **52**, 10905 (2013).

[12] L. Reggie, J. J. Lopez, I. Collinson, C. Glaubitz, and M. Lorch, J. Am. Chem. Soc. **133**, 19084 (2011).

[13] A. H. Linden, S. Lange, W. T. Franks, Ü. Akbey, E. Specker, B.-J. van Rossum, and H. Oschkinat, J. Am. Chem. Soc. **133**, 19266 (2011).

[14] E. J. Koers, E. A. W. van der Cruijsen, M. Rosay, M. Weingarth, A. Prokofyev, C. Sauvée, O. Ouari, J. van der Zwan, O. Pongs, P. Tordo, W. E. Maas, and M. Baldus, J. Biomol. NMR **60**, 157 (2014).

[15] V. S. Bajaj, M. L. Mak-Jurkauskas, M. Belenky, J. Herzfeld, and R. G. Griffin, Proc. Natl. Acad. Sci. U. S. A. **106**, 9244 (2009).

[16] H. Takahashi, I. Ayala, M. Bardet, G. De Paëpe, J.-P. Simorre, and S. Hediger, J. Am. Chem. Soc. **135**, 5105 (2013).

[17] T. Wang, Y. B. Park, M. A. Caporini, M. Rosay, L. Zhong, D. J. Cosgrove, and M. Hong, Proc. Natl. Acad. Sci. U. S. A. **110**, 16444 (2013).

[18] M. Renault, S. Pawsey, M. P. Bos, E. J. Koers, D. Nand, R. Tommassen-van Boxtel, M. Rosay, J. Tommassen, W. E. Maas, and M. Baldus, Angew. Chem. Intl. Ed. **51**, 2998 (2012).

[19] M. Kaplan, A. Cukkemane, G. C. P. van Zundert, S. Narasimhan, M. Daniëls, D. Mance, G. Waksman, A. M. J. J. Bonvin, R. Fronzes, G. E. Folkers, and M. Baldus, Nature Meth., **in press** (2015) 10.1038/nmeth.3406.

[20] Y. Matsuki, H. Takahashi, K. Ueda, T. Idehara, I. Ogawa, M. Toda, H. Akutsu, and T. Fujiwara, Phys. Chem. Chem. Phys. **12**, 5799 (2010).

[21] A. B. Barnes, E. Markhasin, E. Daviso, V. K. Michaelis, E. A. Nanni, S. K. Jawla, E. L. Mena, R. DeRocher, A. Thakkar, P. P. Woskov, J. Herzfeld, R. J. Temkin, and R. G. Griffin, J. Magn. Reson. **224**, 1 (2012).

[22] K. R. Thurber, and R. Tycko, Isr. J. Chem. **54**, 39 (2014).

[23] B. Corzilius, L. B. Andreas, A. A. Smith, Q. Z. Ni, and R. G. Griffin, J. Magn. Reson. **240**, 113 (2014).

[24] F. Mentink-Vigier, Ü. Akbey, Y. Hovav, S. Vega, H. Oschkinat, and A. Feintuch, J. Magn. Reson. **224**, 13 (2012).

[25] K. R. Thurber, and R. Tycko, J. Chem. Phys. **137**, 084508 (2012).

[26] K. L. Ivanov, A. N. Pravdivtsev, A. V. Yurkovskaya, H.-M. Vieth, and R. Kaptein, Prog. Nucl. Magn. Reson. Spectr. **81**, 1 (2014).

[27] A. N. Pravdivtsev, A. V. Yurkovskaya, N. N. Lukzen, H.-M. Vieth, and K. L. Ivanov, Phys. Chem. Chem. Phys. **16**, 18707 (2014).

[28] K. R. Thurber, and R. Tycko, J. Chem. Phys. **140**, 184201 (2014).

[29] C. Song, K.-N. Hu, C.-G. Joo, T. M. Swager, and R. G. Griffin, J. Am. Chem. Soc. **128**, 11385 (2006).

[30] C. Sauvée, M. Rosay, G. Casano, F. Aussenac, R. T. Weber, O. Ouari, and P. Tordo, Angew. Chem. Intl. Ed. **52**, 10858 (2013).

[32] H. Blok, J. A. J. M. Disselhorst, S. Orlinskii, and J. Schmidt, J. Magn. Reson. **166**, 92 (2004).

[33] G. Mathies, H. Blok, J. A. J. M. Disselhorst, P. Gast, H. van der Meer, D. M. Miedema, R. M. Almeida, J. J. G. Moura, W. R. Hagen, and E. J. J. Groenen, J. Magn. Reson. **210**, 126 (2011).

[34] J. A. J. M. Disselhorst, H. van der Meer, O. G. Poluektov, and J. Schmidt, J. Magn. Reson., Ser. A **115**, 183 (1995).

[35] M. Mehring, *Principles of High Resolution NMR in Solids* (Springer-Verlag, Berlin Heidelberg New York, 1983).

[36] K.-N. Hu, C. Song, H.-H. Yu, T. M. Swager, and R. G. Griffin, J. Chem. Phys. **128**, 052302 (2008).

[37] D. Suwelack, W. P. Rothwell, and J. S. Waught, J. Chem. Phys. **73**, 2559 (1980).

[38] A. Zagdoun, G. Casano, O. Ouari, M. Schwarzwälder, A. J. Rossini, F. Aussenac, M. Yulikov, G. Jeschke, C. Copéret, A. Lesage, P. Tordo, and L. Emsley, J. Am. Chem. Soc. **135**, 12790 (2013).

[39] C. Ramanathan, Appl. Magn. Reson. **34**, 409 (2008).

[40] J. P. Wolfe, Phys. Rev. Lett. **31**, 907 (1973).

[41] Y. Hovav, A. Feintuch, and S. Vega, J. Chem. Phys. **134**, 074509 (2011).

[42] A. Abragam, and M. Goldman, Rep. Prog. Phys. **41**, 395 (1978).

[43] Y. Hovav, I. Kaminker, D. Shimon, A. Feintuch, D. Goldfard, and S. Vega, Phys. Chem. Chem. Phys. **17**, 226 (2015).

[44] L. Lumata, M. E. Merritt, C. R. Malloy, A. D. Sherry, and Z. Kovacs, J. Phys. Chem. A **116**, 5129 (2012).

[45] S. Colombo Serra, M. Filibian, P. Carretta, A. Rosso, and F. Tedoldi, Phys. Chem. Chem. Phys. **16**, 753 (2014).

[46] D. J. Kubicki, A. J. Rossini, A. Purea, A. Zagdoun, O. Ouari, P. Tordo, F. Engelke, A. Lesage, and L. Emsley, J. Am. Chem. Soc. **136**, 15711 (2014).

[47] E. A. W. van der Cruijsen, E. J. Koers, C. Sauvée, R. E. Hulse, M. Weingarth, O. Ouari, E. Perozo, P. Tordo, and M. Baldus, **Chemistry,** revision submitted (2015).

[48] Y. Hovav, A. Feintuch, and S. Vega, J. Magn. Reson. **214**, 29 (2012).

CHAPTER 4

Aspects of high field Dynamic Nuclear Polarization

This chapter is adapted from the following publication:

D. Mance, M. Weingarth, and M. Baldus, "Solid-State NMR on Complex Biomolecules: Methods and Applications," in *Modern Magnetic Resonance*, Cham: Springer International Publishing, 2016, pp. 1–17.

Introduction

Solid-state NMR (ssNMR) has proven itself to be an important tool in providing structural information at a atomistic level. The main advantage of this technique is that there is in principle no limitation on sample heterogeneity, the molecular environment or size[1–3]. However as complexity of the sample increases, this leads to challenges regarding resolution and sensitivity. Spectral resolution can be improved by using fast magic angle spinning or by employing higher magnetic fields as this could allow for better dispersed signals even under low-temperature conditions[4,5]. As discussed in chapters 1 and 2 ^{1}H detection can help to improve ssNMR sensitivity. A more general method to increase sensitivity refers to Dynamic Nuclear Polarization (DNP). This is in particularly important as molecular size and complexity increase which leads to an effectively lower amount of NMR active sample. For example, this situation applies to studying a protein which is reconstituted in synthetic bilayers compared to the protein in a cellular environment. It is also interesting that various systems such as microcrystalline SH3, membrane protein KcsA and cellular samples (T4SScc and EGFR) that have been studied also gave variable DNP enhancements[5–8]. However although DNP provides an increase in sensitivity as the magnetic field is increased the enhancement provided by DNP tends to decrease. This decrease in enhancement as the magnetic field is increased can be described by simulations[9,10]. The simulations showed that the polarization in DNP is usually distributed by spin-diffusion processes among protons. This observation suggests that core protons near the biradical act as a "polarisation sink" since they do not contribute in the spin-diffusion process, but could still get polarized. Recently, this effect has been observed experimentally using various deuterated biradicals[11], where after deuteration of the core protons, a beneficial effect on the DNP enhancement was detected. This means that when the spin-diffusion is limited polarization will be mostly confined to the vicinity of the DNP radical. This aspect is important for studying surface species of functional materials since these typically exhibit a low concentration of molecular surface groups meaning that sensitivity is typically a critical issue in these samples. Furthermore by modelling the spin-diffusion process using "Fick's Law" additional information can be obtained such as crystal size[12,13]. As a result, the enhancements themselves can be used to obtain further information of the sample of interest. This is particularly interesting in the case of intact biosilica[13], which consist of different molecular layers from which each of these enhancements can be obtained. It will be

shown how these enhancements of each layer can be linked to the corresponding thickness of each layer.

Although DNP has proven itself to be an excellent tool for improving sensitivity, one of the major concerns to overcome is the resolution of DNP acquired spectra for, mainly, biomolecules. It has been shown that the observed line width under these low-temperature conditions are mainly due to the molecular dynamics [5]. Spectral resolution can be further improved by increasing the temperature or magnetic field strength at the cost of the sensitivity gain[4,5,14]. Alternatively, it is possible to circumvent this issue by reducing the number of signals present in the spectra. For protein studies, the use of amino-acid selective isotope labelling has been shown to lead to the simplification of DNP spectra[15,16]. Which is particularly interesting for large systems of which obtaining these specific signals was only possible due to the sensitivity gain by DNP[7,8].

Apart of incorporating soluble biradicals into a sample, it was also already shown that it is possible to apply spin-labels[17]. Typically nitroxide spin-labels (MTSL) are introduced in EPR at a location in a protein where a cysteine is either present or introduced allowing the spin-label to react with the sulfide group and covalently attach itself to the protein[18]. In EPR this strategy allows for distance measurements between spin-labels. However, in the case of DNP it is possible to adapt EPR principles by covalent attachment of biradicals at Cys residues. This idea would allow introducing DNP probes which enhance the sensitivity and would be localized to a specific site. These principles could be further exploited in enhancing the sensitivity and obtaining structural information.

Sample Preparation for DNP measurements

An important step required for DNP measurements is the addition of the biradical used (e.g. TOTAPOL or AMUPol) to the ssNMR sample. Depending on the type of sample this can be done in different mixtures and thus a suitable mixture should be chosen depending on the sample and radical. This is an important requirement for DNP in order to obtain uniformly distributed radical and DNP enhancements throughout the sample which, furthermore, contains a glass forming agent and -if required- additional protonated compounds. The biradical concentration is usually kept between 10-20mM.

(Bio)Material samples

For material type applications, the sample volume to start with should at least match the volume of the MAS rotor. The radical is incorporated into the sample by incipient wetness impregnation[19], where minimal amounts of radical solutions are used in order to wet the surface. However depending on the type of sample the usually used Glycerol:D_2O:H_2O mixture can limited DNP enhancements due to the poor viscosity. Therefore, a number of different solutions can potentially be used. For the case where the sample is compatible with H_2O, solvents such as 90:10 D_2O:H_2O or 78:14:8 DMSO:D_2O:H_2O can be used. In non-aqueous cases organic solvents can be employed. Here, various solvents such as 1,1,2,2-tetrachloroethane have been tested in literature with varying DNP performances and most likely some optimization is required on new samples of interest[20]. Coperet et al reported that the radical TEKPol[21] may be particularly well suited for such applications Nonetheless radicals such as TOTAPOL and AMUPOL can still provide significant enhancements under these conditions. After an appropriate solvent is selected, 10-20mM biradical and small amounts of this solvent are added to the material of interest until it becomes a wet paste. When a non-porous sample is wetted, the solvent/radical mixture will mainly remain on the surface. In the case of porous materials, the solvent and, depending on the pore-size, the radical may enter the pores. After the wetting procedure the sample can be packed in a rotor for measurement.

Biomolecular samples

For soluble biomolecules, water-soluble biradicals are preferred such as AMUPol or TOTAPOL. The desired (final) solvent solution used is 60:30:10 (vol:vol:vol) d_8-Glycerol:D_2O:H_2O with a radical concentration between 10-20mM for the measurements. Thus, depending on how the soluble biomolecule is prepared it can be used in the D_2O or H_2O fraction and mixed with the biradicals.

For membrane proteins and cellular preparations, sample preparation can be more difficult due to the inhomogeneous distribution of the radical throughout the sample. There are essentially two different sample preparations routes possible either with direct titration or with centrifugation. The centrifugation method seems to be more general applicable and is usually used. In the case of direct titration[22], it is important to know the total volume of the pellet. To the pellet, small aliquots of a stock radical solution are added and vortexed in order to obtain a homogeneous distribution of radical throughout the sample. Subsequently, D_2O is added to the

sample until a ratio of 3:1 D_2O:H_2O is achieved. Excess water can be removed afterwards by a brief lyophilisation step to reach a final hydration level of 40%. Finally, the samples are packed into the MAS rotor.

With the centrifugation method, a stock solution of approximately 100µl is prepared, typically containing 20:70:10 d_8-Glycerol:D_2O:H_2O and a 10-20mM radical concentration. Note that the d_8-glycerol content is reduced to approximately 20% due to the higher density of d_8-glycerol compared water to ensure proper formation of the pellet. Alternatively low amounts of DMSO[23] that has a density similar to water can also be added to overcome possible solubility issues. The protein pellet is re-suspended in ~50µl of the stock solution, depending on the amount of sample present. Subsequently, the sample is centrifuged at ~45000 rpm for 30min to up to an hour to form the desired pellet from which the supernatant is removed. The procedure is repeated once more in order to ensure consistency before packing the sample into the rotor.

Nuclear Spin-diffusion in DNP

For DNP measurements, typically soluble radical is incorporated into the sample of interest and usually leads to a well distributed radical throughout the sample. The efficiency of the initial polarization transfer step between the biradical and the sample under DNP conditions depends on various parameters such as the electron-nuclear hyperfine coupling, the electron relaxation times of the biradical and dipolar coupling between the electrons[9,10,24]. In order to describe the initial polarization transfer, one requires the need of quantum mechanical simulations which was shown in the previous chapter. However, after this initial electron-nuclear polarization transfer step, subsequent internuclear transfers to the bulk rely on ^{1}H spin diffusion which depends on dipolar couplings. It was shown for a peptide crystal[12] that by describing this spin diffusion process using a classical one- dimensional diffusion model it was possible to correlate the DNP enhancement with various properties such as the crystal size. For this description, it is assumed that there is a uniform polarization of the nuclei nearby the radical at the exterior/surface given by the DNP enhancement factor ε_0. Nuclear spin diffusion to the interior of sample can then be described according to a classical one- dimensional diffusion model using Fick's law[12,25]:

$$\frac{\partial P}{\partial t} = D\frac{\partial^2 P}{\partial x^2} - \frac{P}{T_{1n}} \tag{4.1}$$

In eq. (4.1) $P(x,t)$ represents the polarization that depends on time (t) and the distance (x). D is the diffusion constant and T_{1n} stands for the longitudinal nuclear relaxation time. In the steady-state, $\frac{\partial P}{\partial t} = 0$, eq. (4.1) only depends on the distance x and can be rewritten as:

$$D\frac{\partial^2 P}{\partial x^2} = \frac{P}{T_{1n}} \tag{4.2}$$

$P(0)$ represents the nuclei that are closest to the radical while $P(a)$ represents nuclei that are located at a larger distance *a* from the biradical which has the consequence that these nuclei do not experience any DNP enhancement. The corresponding boundary conditions hence read as:

$$P(0) = \varepsilon_0 P_0 \ , \ P(a) = 0 \tag{4.3}$$

Where ε_0 is the steady state enhancement factor and P_0 is the polarization at thermal equilibrium. Solving (4.2) with boundary conditions given in eq. (4.3) results in:

$$P(x) = \varepsilon_0 P_0 Csch\left[\frac{a}{\sqrt{DT_{1n}}}\right] Sinh\left[\frac{a-x}{\sqrt{DT_{1n}}}\right] \tag{4.4}$$

Averaging this result over the size of a layer (size w) gives:

$$\frac{1}{w}\int_0^w P(x)dx = \frac{\varepsilon_0 P_0 \sqrt{DT_{1n}}}{w}\left[Coth\left[\frac{a}{\sqrt{DT_{1n}}}\right] - Cosh\left[\frac{a-w}{\sqrt{DT_{1n}}}\right] Csch\left[\frac{a}{\sqrt{DT_{1n}}}\right]\right] \tag{4.5}$$

Thus, the enhancement (ε) can then be defined by:

$$\varepsilon = \frac{\varepsilon_0 \sqrt{DT_{1n}}}{w}\left[Coth\left[\frac{a}{\sqrt{DT_{1n}}}\right] - Cosh\left[\frac{a-w}{\sqrt{DT_{1n}}}\right] Csch\left[\frac{a}{\sqrt{DT_{1n}}}\right]\right] \quad (4.6)$$

Because the resulting DNP signal enhancement is dictated by spin diffusion processes, the relative DNP enhancement of locally separated molecular subsystems can report on supramolecular structure.

Intact Diatom Biosilica

Diatom Biosilica (see Figure 4.1) consist of different molecular layers, i.e., polysaccharides, peptides, polyamines and silica. The DNP biradical is incorporated into the sample by wetness impregnation and will thus be confined to the surface. As shown in Figure 4.1e, it was possible to acquire various 2D-NMR experiments on this intact sample allowing the identification of aspartic acid and glutamic acid and revealing that these amino acids are predominantly present in a β-sheet conformation. In addition to using the data for identifying the type and conformation of amino acids present, it is also possible to use the DNP enhancements themselves in order to learn more of the system. Since the radical is confined to the surface polarization transfer to the inner molecular layers can, as discussed above, be treated classically using Fick's Law. In this formalism, the longitudinal nuclear relaxation time (T_{1n}) and the diffusion constant (which depends on the average ^1H-^1H distance) will ultimately determine the local DNP enhancement. Since biosilica consist of different molecular layers (determined by specific diffusion constant and T_{1n} parameters) theoretical models can be compared to the measured enhancements to estimate the thickness of each layer (Figure 4.2). The molecular architecture of the organic material at the atomic and nanometer scale has so far remained unknown, in particular for intact biosilica. The combination of DNP experiments with microscopy, mass spectrometry (MS), and molecular dynamics (MD) simulations provides insight into the structural characterization of such system and by using this information it is possible to propose a model of this system as is shown in Figure 4.2c.

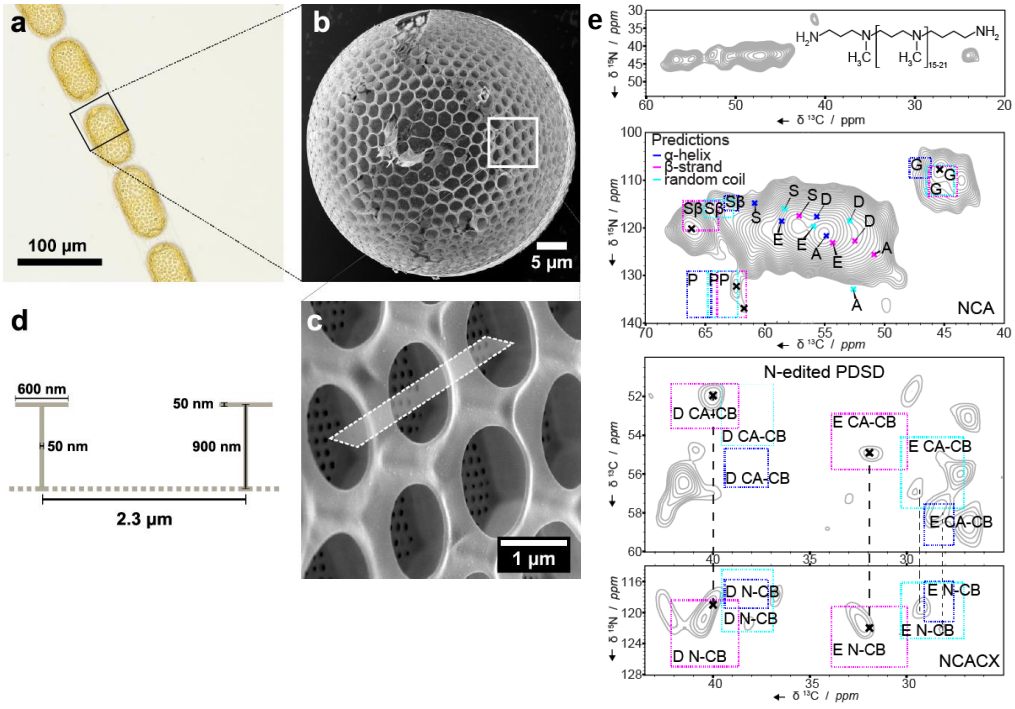

Figure 4.1. Biosilica - a micro- and nanopatterned hybrid material. a, Bright field microscopy image of *S. turris* (living cells). b and c, Helium ion microscopy images of *S. turris* biosilica extracted by treatment with SDS/ EDTA. The grey rectangle in c indicates a region for which a cut through the cell wall would reveal the characteristic profile schematically depicted in d) 2D ^{15}N-^{13}C correlation and a ^{15}N-edited ^{13}C-^{13}C correlation experiment measured using a 400 MHz DNP spectrometer with chemical shift predictions[26,27] for different secondary structures (pink: β-strand, cyan: random-coil, blue: α-helix). The size of the boxes reflects the standard deviation of the predictions. The spectra show aspartic (D) and glutamic (E) acid Cβ peaks predominantly in β-sheet conformation.

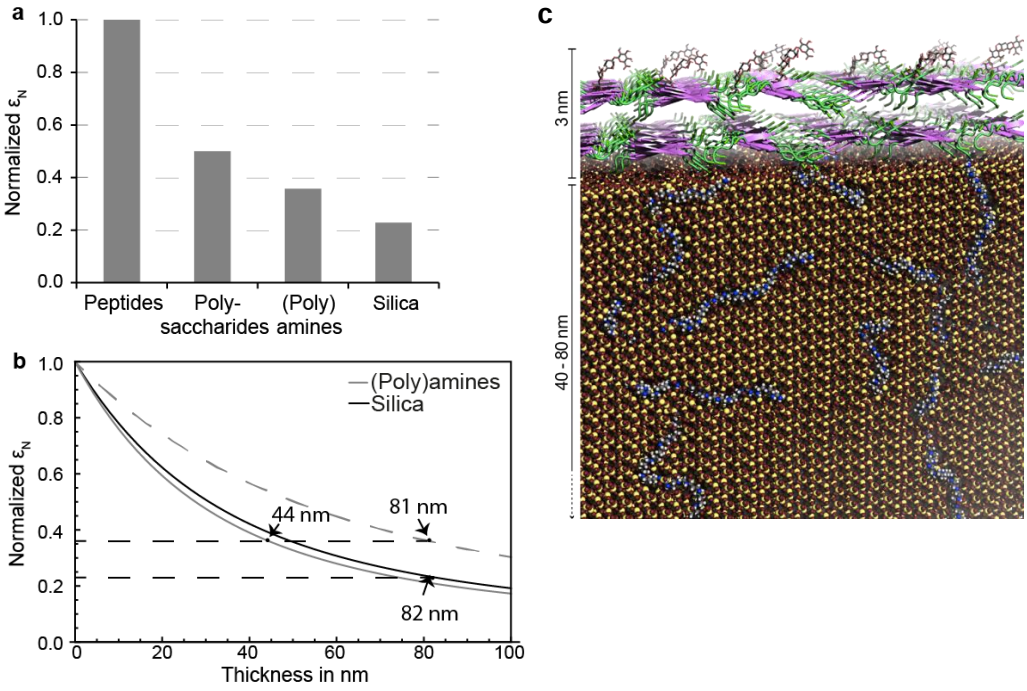

Figure 4.2. Structural analysis of DNP enhancement factors. a, Measured signal enhancement factors for biosilica-associated biomolecules normalized to DNP enhancements seen for peptide signals. b, Simulated DNP enhancement factors as a function of the thickness of a layer for polyamines and silica. Gray curves represent the normalized enhancement for a theoretically assumed polyamine layer based on a diffusion constant from the literature 300 nm^2/s (ref.[28]) and the dotted gray line 1000 nm^2/s (ref.[12]). The black curve represents the normalized enhancement for silica using a calculated diffusion constant of 62 nm^2/s based on a proton-proton distance of 5.5 Å. c shows a model for the supramolecular architecture of *S. turris* biosilica. An approximately 3nm layer containing carbohydrates and proteins covers the 40–80 nm silica phase (colored in red and yellow). The proteins show a tendency to form β-strand secondary structure, as revealed by 2D DNP-ssNMR spectroscopy. Low DNP signals enhancements (ε_N) compared to other detected organic species suggest a broad dispersion of LCPAs (colored in gray, blue and white) in the silica phase.

Such considerations can also be extended to predict the effect of variations in proton density on the resulting DNP enhancement for a wide range of molecular sizes[30]. In Figure 4.3A, a small protein with a dimension of approximately 5 nm dimension is compared to plasma membrane vesicles[8] (about 200 nm's, Figure 4.3B) and entire eukaryotic cells (Figure 3C, 15 micrometers). As visible in Figure 4.3 (lower panel), DNP enhancements are largely constant in small proteins, unless high levels of proton dilution (such as fractional deuteration as discussed in chapter 2 or per-deuteration) are used and, at the same time, short T_{1n} relaxation times are active. This situation significantly changes in the case of plasma membrane vesicles where only full protonation allows for relatively constant DNP enhancement factors across each vesicle. Finally, sizable DNP enhancements are largely confined to approximately a micrometer ring on the outside of mammalian cells when soluble DNP radicals are added. Thus, a non-uniform distribution of the polarization can be created by using larger molecular dimensions or by chemically modulating spin-diffusion as well as relaxation parameters.

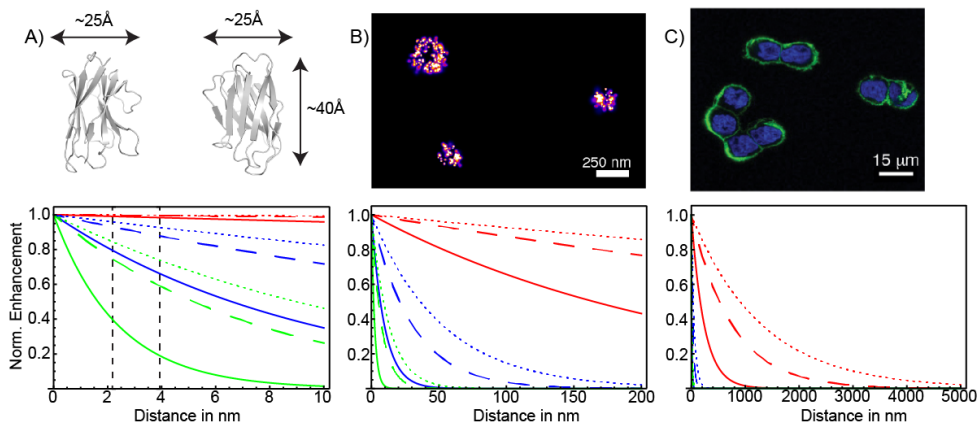

Figure 4.3. Model calculations assuming an initial creation of DNP-enhanced magnetic polarization that is transferred to the interior of molecules of different size via spin diffusion. In each case, polarization was computed for the indicated distance from the molecular surface for average ^{1}H-^{1}H distances of 1Å (red), 5Å (blue) and 10Å (green). In addition, we varied T_{1n} relaxation times from 1s (solid lines), 10s (dashed lines) and 30 s (dotted lines).

Studying large systems with selective isotope labelling

Solid-state NMR has been shown to track proteins in native membranes. Since there is no size limitation for solid-state NMR it becomes interesting to develop methods in order to be able to study larger complexes and even cellular samples. However, such applications pose additional challenges in terms of sensitivity and ssNMR data interpretation. An important tool for biomolecular solid-state NMR is the use of amino-acid selective isotope labelling. By incorporating certain isotopically enriched amino acids into the protein of interest, spectral overlap is reduced since signals of unlabelled amino acids are removed, allowing a more straightforward interpretation of the spectra[15,16]. The combination of carefully chosen $^{15}N/^{13}C$ labelled amino acids further reduces spectral ambiguity if, so called, NCOCX experiments that probe sequential correlations[31] are used (vide infra). Notably, an additional benefit of using tailored isotope labelling is the reduced contribution of line-broadening effects due to freezing out the various conformations of the protein at low-temperature DNP conditions.

Type IV secretion system core complex

An example in which the use of selective amino-acid labelling assisted in probing a large complex refers to the study performed on the bacterial type IV secretion system core complex (T4SScc) shown in Figure 4.4a comprising a size of approximately a megadalton. This complex contains a protein channel consisting of 14 copies of 3 proteins though which DNA and proteins can be transported. Due to the size of the system, sensitivity becomes one of the major issues and would complicate studying such systems by conventional solid-state NMR. Nonetheless with the sensitivity increase by DNP (~60 enhancement was measured on this sample with the AMUPol biradical) it is possible to greatly reduce the experimental time. Combination of DNP with with carefully labelling certain amino acids with ^{15}N or ^{13}C allowed the design of 2D and 3D experiments which probe the various domains of this large complex and allow these signals to be tentatively assigned in a cellular environment. The amino acids chosen to be isotopically enriched are picked in such a manner that residue i is ^{15}N-labelled and residue i-1 is ^{13}C labelled. By combining this labelling strategy with a NMR experiment such as NCO (which correlated ^{15}N from residue i with $^{13}C'$ from residue i-1), the resulting ssNMR spectrum will only contain signals from labelled protein pairs. Apart from providing just a couple of signals in such DNP-supported ssNMR experiments, the amino acid pairs chosen were also strategically distributed through this large complex. Figure 4.4a shows the location of the

isotopically enriched ^{15}N,^{13}C pairs as coloured spheres in T4SScc, Figure 4.4b shows the resulting NCOCX spectrum.

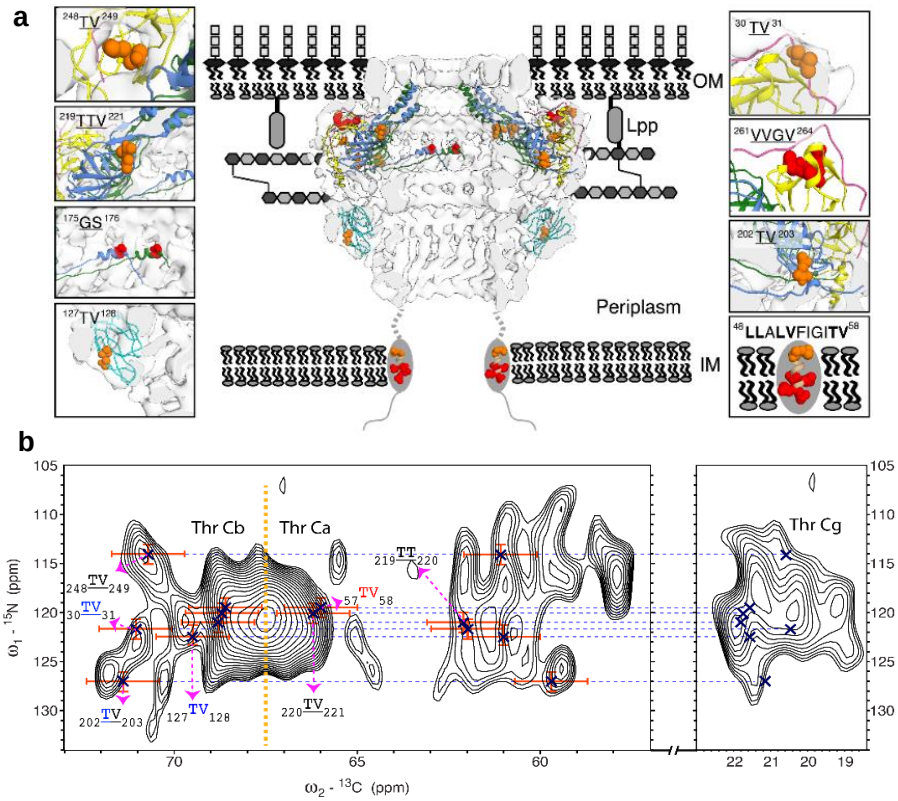

Figure 4.4. a) Residue-specific ssNMR probes and their location in reference to the cellular envelope including the T4SScc electron microscopy map with the outer membrane complex fitted inside (PDB 3JQO). Identified residues in our spectra are shown as orange balls for the TV-T4SScc and red balls for the GSLV-T4SScc. Boxes represent zoom-ins of the identified correlations. b) tentatively assigned residues shown on the 2D NCOCX spectrum.

Epidermal growth factor receptor

Other than probing various protein domains with DNP, it was also shown that binding of a ligand to a large system can also be studied in combination with DNP and selective amino acid labelling. These studies involved the Epidermal growth factor receptor (EGFR) which is involved in cell growth and embedded in the plasma membrane of mammial cells. Binding of EGF to EGFR is believed to cause structural changes, namely the inactive monomer form is converted into activated homodimer as shown in Figure 4.5a. So far however, structural information about this activation process was only obtained by X-ray and NMR studies of EGFR segments without the presence of the native cell environment, i.e., the plasma membrane.

The DNP signal enhancement measured on this sample was ~80 using the 400MHz/263GHz system. A similar strategy as in the T4SScc case was employed to obtain local information about EGFR. Again, we made use of incorporating isotopically labelled amino-acid pairs where residue i is ^{15}N and residue i-1 is ^{13}C labelled on specifically chosen locations. These NMR probes allowed us to track differences between the spectra of EGFR before and after binding of EGF. This experiment was only possible due to the sensitivity gain provided by DNP which enabled the recording of 3D NCOCx spectra on these samples. Due to protein dynamics, which leads to broadening in the spectra there is a minor benefit from the additional nitrogen dimension. However, by using an additional spin-diffusion step, a so called (NCO)CxCx spectrum (called N-edited CC in Figure 4.5b[32]) can be recorded. This spectrum benefits from still selecting the chosen amino acid pairs along with correlations between the aliphatic carbons which in general are better resolved allowing for a more straightforward identification of the amino-acid pairs in the different conformations.

Ultimately, the combination of these DNP experiments with conventional ssNMR experiments suggested that rather than a defined overall reorientations of specific receptor domains, activation of EFGR by EGF leads to a reduction of overall as well as local receptor dynamics. Thus, activation proceeds via a process of conformational selection[33].

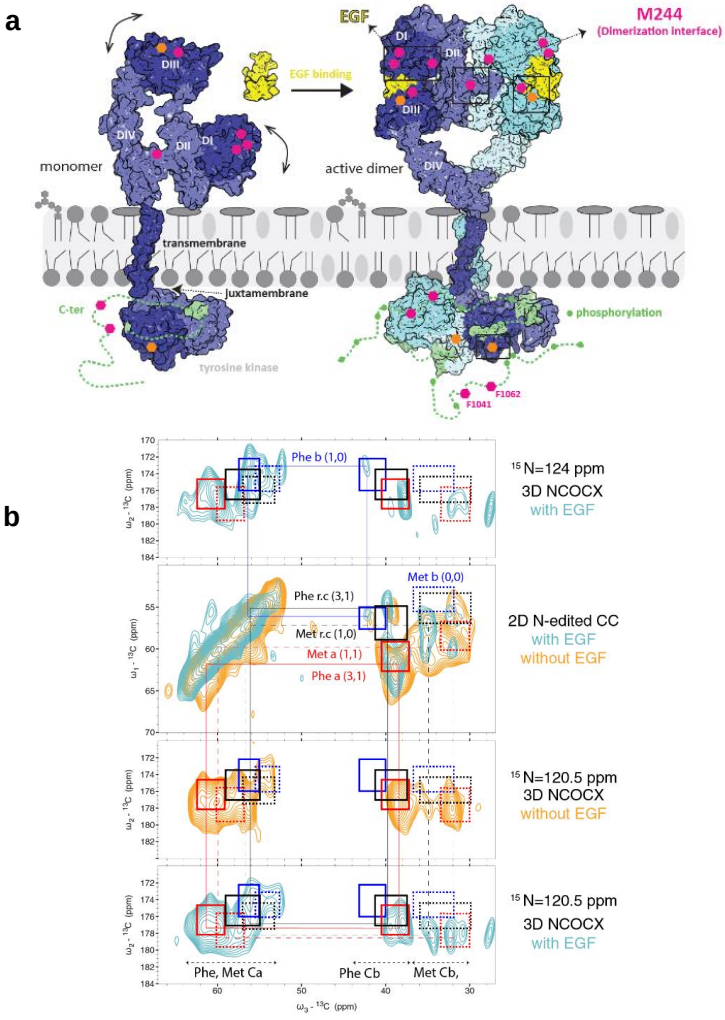

Figure 4.5. a) Model of EGFR Dynamics and Structural Changes in the Free and EGF-Bound Forms, coloured spheres indicated various isotope labelled unique sequential pairs. b) 2D NCO type experiment of MFTL-labeled A431 membrane vesicles with and without EGF performed on 400 MHz DNP field.

Site specific spin-labels

Apart of focussing on enhancing the ssNMR signal of the whole sample we also investigated the possibility to exploit the use of spin-labels as DNP sources. As described before typically the polarization is spread throughout the sample by spin-diffusion. In the case of soluble biradical this results in the need of adding additional protons in the form of water to assist in transferring the polarization from the biradical towards, in this case, a protein. However, this process will also lead to polarization of the solvent thus causing an effective loss of polarization. A method to circumvent this issue would be the use of spin-labels similar to how these are used in EPR, but using a biradical instead.

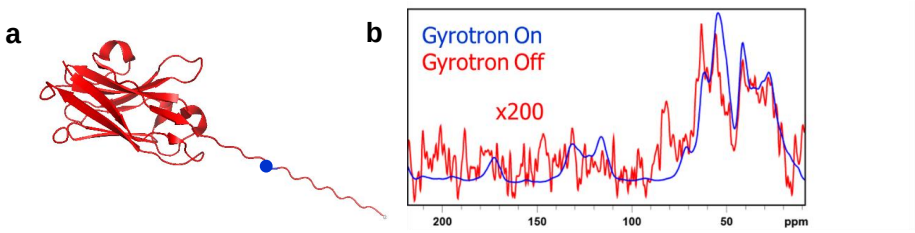

Figure 4.6. a) 7d12 nanobody from PDB: 4KRL, the blue sphere indicates a cysteine mutation with the biradical spin-label. b) 1d ^{13}C CP-MAS experiments at 400MHz under DNP conditions at a MAS rate of 8kHz with and without microwave irradiation.

Previous work has already shown the possibility in obtaining sizeable enhancements using such biradical spin labels[17,23], in particular when a more favourable buffer composition is used. These spin-labels have shown to predominantly transfer polarization towards the protein. We have therefore tagged a previous described AMUPol[17] spin-label to a nanobody which contains a cysteine mutation and used a fully deuterated buffer. This nanobody (7D12) has been shown to bind to domain 3 of EGFR[34].

The use of a fully deuterated buffer will prevent the polarization spreading to the buffer and will thus predominantly direct transfer towards the protein[23]. Measurements done on this sample at 400MHz/263GHz are shown in Figure 4.5, which shows a remarkable enhancement of 200. This can have interesting applications where a ligand of interest can be tagged with the

spin label and combining this with deuteration can confine the polarization to for example the binding interface. In the case of the nanobody this could potentially be done when binding to EGFR which prevents the binding of EGF.

Conclusions

We have shown how DNP can be used for systems where typically sensitivity plays an important role. Furthermore, being able to describe the polarization transfer itself by classical equations can link enhancements measured in DNP experiments with further ssNMR parameters to probe supramolecular structure such as the layer thicknesses in intact biosilica. Combining DNP with selective amino-acid isotope -labelling provides an interesting tool for investigating large complexes. By designing the ssNMR experiments to make use of the ^{13}C-^{15}N paired amino acids, DNP spectra can be greatly simplified, leading to a more straight forward interpretation of the data as has been shown for the case of EGFR and T4SS. Finally, the ongoing developments in radical synthesis allow for new experiments such as introducing biradical spin-labels which can increase the enhancement further by choosing a favourable buffer composition which allows a more efficient transfer towards the protein of interest.

References

[1] M. Weingarth, M. Baldus, *Acc. Chem. Res.* **2013**, *46*, 2037–46.

[2] M. Renault, R. Tommassen-van Boxtel, M. P. Bos, J. A. Post, J. Tommassen, M. Baldus, *Proc. Natl. Acad. Sci. U. S. A.* **2012**, *109*, 4863–8.

[3] M. Kaplan, C. Pinto, K. Houben, M. Baldus, *Q. Rev. Biophys.* **2016**, *49*, e15.

[4] P. Fricke, D. Mance, V. Chevelkov, K. Giller, S. Becker, M. Baldus, A. Lange, *J. Biomol. NMR* **2016**, *65*, 121–126.

[5] E. J. Koers, E. a. W. van der Cruijsen, M. Rosay, M. Weingarth, C. Prokofyev, Alexander Sauvée, O. Ouari, O. Pongs, P. Tordo, W. E. Maas, M. Baldus, *J. Biomol. NMR* **2014**, *60*, 157–168.

[6] T. Jacso, W. T. Franks, H. Rose, U. Fink, J. Broecker, S. Keller, H. Oschkinat, B. Reif, *Angew. Chemie Int. Ed.* **2012**, *51*, 432–435.

[7] M. Kaplan, A. Cukkemane, G. C. P. van Zundert, S. Narasimhan, M. Daniëls, D. Mance, G. Waksman, A. M. J. J. Bonvin, R. Fronzes, G. E. Folkers, et al., *Nat. Methods* **2015**, *12*, 5–9.

[8] M. Kaplan, S. Narasimhan, C. de Heus, D. Mance, S. van Doorn, K. Houben, D. Popov-Čeleketić, R. Damman, E. A. Katrukha, P. Jain, et al., *Cell* **2016**, *167*, 1241–1251.e11.

[9] F. Mentink-Vigier, Ü. Akbey, H. Oschkinat, S. Vega, A. Feintuch, *J. Magn. Reson.* **2015**, *258*, 102–120.

[10] D. Mance, P. Gast, M. Huber, M. Baldus, K. L. Ivanov, *J. Chem. Phys.* **2015**, *142*, 234201.

[11] F. A. Perras, R. R. Reinig, I. I. Slowing, A. D. Sadow, M. Pruski, *Phys. Chem. Chem. Phys.* **2016**, *18*, 65–9.

[12] P. C. A. Van Der Wel, K.-N. Hu, J. Z. Lewandowski, R. G. Griffin, *J. Am. Chem. Soc.* **2006**, *128*, 10840–10846.

[13] A. Jantschke, E. Koers, D. Mance, M. Weingarth, E. Brunner, M. Baldus, *Angew. Chemie - Int. Ed.* **2015**, *54*, 15069–15073.

[14] Ü. Akbey, H. Oschkinat, *J. Magn. Reson.* **2016**, *269*, 213–224.

[15] D. C. Muchmore, L. P. Mcintosh, C. B. Russell, D. E. Anderson, F. W. Dahlquist, *Methods Enzymol* **1989**, *177*, 44-73.

[16] K. I. Tong, M. Yamamoto, T. Tanaka, *J. Biomol. NMR* **2008**, *42*, 59–67.

[17] E. A. W. van der Cruijsen, E. J. Koers, C. Sauvée, R. E. Hulse, M. Weingarth, O. Ouari, E. Perozo, P. Tordo, M. Baldus, *Chem. - A Eur. J.* **2015**, *21*, 12971–12977.

[18] L. J. Berliner, H. Olga Hankovszky, *Anal. Biochem.* **1982**, *119*, 450–455.

[19] A. Lesage, M. Lelli, D. Gajan, M. A. Caporini, V. Vitzthum, P. Miéville, J. Alauzun, A. Roussey, C. Thieuleux, A. Mehdi, et al., *J. Am. Chem. Soc.* **2010**, *132*, 15459–15461.

[20] A. Zagdoun, A. J. Rossini, D. Gajan, A. Bourdolle, O. Ouari, M. Rosay, W. E. Maas, P. Tordo, M. Lelli, L. Emsley, et al., *Chem. Commun.* **2012**, *48*, 654–656.

[21] A. Zagdoun, G. Casano, O. Ouari, M. Schwarzwälder, A. J. Rossini, F. Aussenac, M. Yulikov, G. Jeschke, C. Copéret, A. Lesage, et al., *J. Am. Chem. Soc.* **2013**, *135*, 12790–12797.

[22] S. Y. Liao, M. Lee, T. Wang, I. V. Sergeyev, M. Hong, *J. Biomol. NMR* **2016**, *64*, 223–237.

[23] T. Viennet, A. Viegas, A. Kuepper, S. Arens, V. Gelev, O. Petrov, T. N. Grossmann, H. Heise, M. Etzkorn, *Angew. Chemie - Int. Ed.* **2016**, *55*, 10746–10750.

[24] K. R. Thurber, R. Tycko, *J. Chem. Phys.* **2012**, *137*, DOI 10.1063/1.4747449.

[25] I. J. Lowe, D. Tse, *Phys. Rev.* **1968**, *166*, 279–291.

[26] Y. Wang, O. Jardetzky, *Protein Sci.* **2002**, *11*, 852–61.

[27] K. Seidel, M. Etzkorn, R. Schneider, C. Ader, M. Baldus, *Solid State Nucl. Magn. Reson.* **2009**, *35*, 235–242.

[28] C. Ader, R. Schneider, K. Seidel, M. Etzkorn, S. Becker, M. Baldus, *J. Am. Chem. Soc.* **2009**, *131*, 170–176.

[29] Patrick C. A. van der Wel, Kan-Nian Hu, and Józef Lewandowski, R. G. Griffin*, **2006**, DOI 10.1021/JA0626685.

[30] D. Mance, M. Weingarth, M. Baldus, in *Mod. Magn. Reson.*, Springer International Publishing, Cham, **2016**, pp. 1–17.

[31] J. Pauli, M. Baldus, B. van Rossum, H. de Groot, H. Oschkinat, *ChemBioChem* **2001**, *2*, 272–281.

[32] L. A. Baker, M. Daniëls, E. A. W. van der Cruijsen, G. E. Folkers, M. Baldus, *J. Biomol. NMR* **2015**, *62*, 199–208.

[33] M. Kaplan, S. Narasimhan, C. de Heus, D. Mance, S. van Doorn, K. Houben, D. Popov-Čeleketić, R. Damman, E. A. Katrukha, P. Jain, et al., *Cell* **2016**, *167*, 1241–1251.e11.

[34] K. R. Schmitz, A. Bagchi, R. C. Roovers, P. M. P. van Bergen en Henegouwen, K. M. Ferguson, *Structure* **2013**, *21*, 1214–1224.

CHAPTER 5

A DNP-supported Solid-state NMR Study of Coke Species in Fluid Catalytic Cracking Catalysts

This chapter is based on the following publication:

D. Mance, J. van der Zwan, M. E. Z. Velthoen, F. Meirer, B. M. Weckhuysen, M. Baldus and E. T. C. Vogt, "A DNP-supported Solid-state NMR Study of Carbon Species in Fluid Catalytic Cracking Catalysts," *Chem. Commun.*, vol. 53, no. 28, pp. 3933–3936, 2017.

Introduction

Fluid Catalytic Cracking (FCC) is the main conversion technology used in oil refineries, converting heavy Vacuum Gas Oil (VGO) and residual feedstocks to valuable transportation fuels like gasoline, and petrochemical raw materials like propylene[1]. During commercial operation, FCC catalysts deactivate rapidly because of the deposition of carbon species. The harsh process conditions, with temperatures cycling between 720°C in oxidative environment in the regenerator and 520-550°C in reducing environment in the riser reactor, enhance the deactivation. Typical contact times in the riser reactor are in the order of seconds, after which the catalyst has to be regenerated to remove the coke species that block the surface and pore system. Deposition of metals like Iron, Nickel, and Vanadium during consecutive cycles may create (de-)hydrogenation activity, which further promotes coke formation[2]. Carbon deposition is not only a negative issue: regeneration of the catalyst by burning off the coke fuels the endothermic cracking reaction and the heat requirements for the process. The trick is thus to limit the amount of coke formed to the absolute minimum required for the thermal equilibrium of the process, also in order to limit the amount of CO_2 formed. However, in a quest to utilize as much of our fossil fuels as possible, heavier feedstocks, like vacuum resids, are more frequently employed. These heavier feedstocks contain more coke precursors, and will deposit more coke from the feedstock directly[3].

Carbon deposition in catalytic processes has been studied extensively[4,5] with bulk techniques like TPO/TGA[6], ^{13}C NMR[7–12], (FT-)IR [4,5], UV-Vis and confocal fluorescence microscopy [13,14], NEXAFS [15-17], EELS [18], EPR [5], PET [19,20], XPS [8], Supercritical Fluid extraction [8], and MALDI-TOF-MS [7, 21].

Various authors have studied the development of coke species over time [5,22,24-26]. Cerqueira et al. [27] describe mainly two types of coke in FCC catalysts, i.e. coke directly deposited from the feedstock, and coke formed on the catalyst surface as a (secondary) result of the cracking process. These different types include hydrocarbons adsorbed on the catalyst surface and within the catalyst pores. In another paper, Cerqueira et al. [28] describe the analysis of carbon deposited on FCC catalysts during cracking of resid feedstocks using a variety of techniques, including ^{13}C MAS (Magic Angle Spinning) NMR [29]. They observe spectra consisting of a large contribution in the aromatic coke range (around 130 ppm) and a smaller signal around 18-20 ppm which is typical for aliphatic carbons [12]. They find that 80-90% of the carbon is in aromatic rings, and the remainder is in aliphatic groups. Based on the low H/C ratio observed,

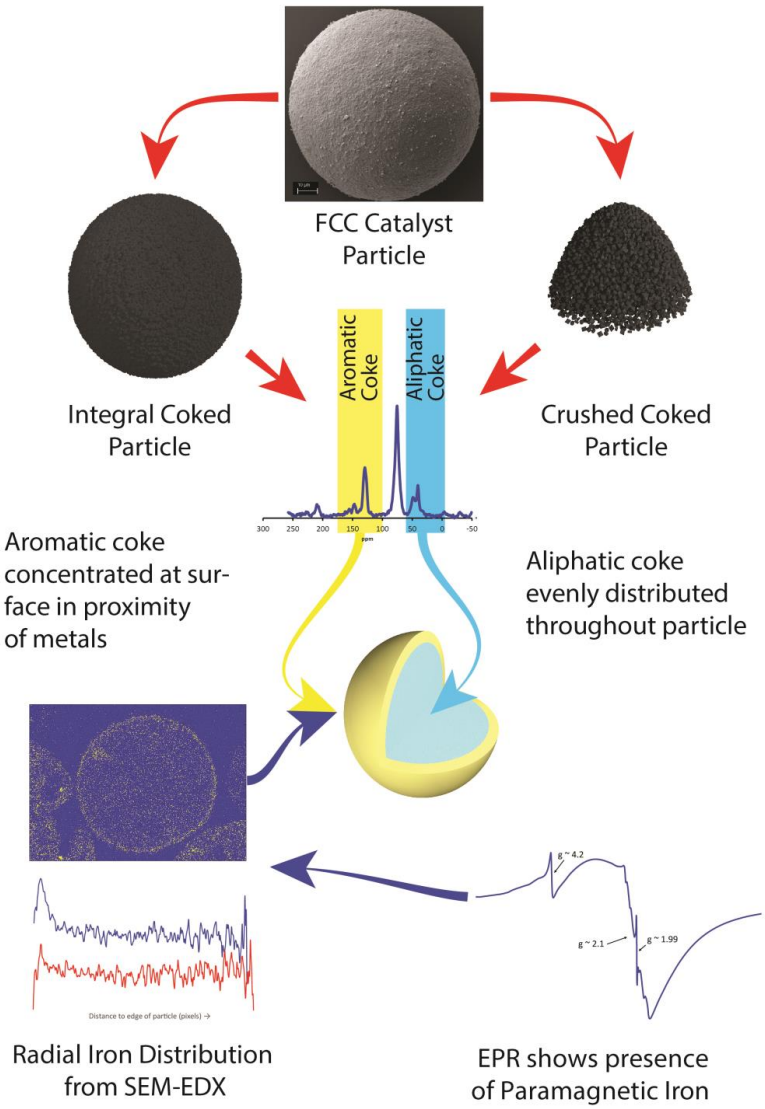

Figure 5.1. Outline of the study: Fluid Catalytic Cracking (FCC) equilibrium catalysts contain metal species deposited during cracking, and originating from the feedstock. SEM-EDX shows iron concentrates at the surface, while EPR confirms the presence of iron as the main paramagnetic species in the FCC catalyst. ^{13}C solid state NMR reveals that aromatic coke is found mostly in conjunction with the metals, whereas aliphatic coke is spread more evenly throughout the FCC catalyst particle.

they conclude the aromatic structures must be relatively large. Similar observations are reported by Barth et al. [7] and Qian et al. [8]. The work of Fonseca et al. on hydroprocessing catalysts [9] suggests young catalytic coke formed as a result of the cracking process is more aliphatic. The work of Snape et al. [12] suggests that coke deposited from heavy feedstocks is more aromatic. However, no direct data are currently available on the spatial distribution of the coke species within integral FCC catalyst particles.

Here we demonstrate the use of a dedicated solid-state NMR approach that involves the application of one- and two-dimensional MAS solid-state NMR experiments conducted at different temperatures in combination with Dynamic-Nuclear-Polarization (DNP)-supported solid-state NMR [30, 31] to examine the spatial distribution of coke species in a commercial equilibrium FCC catalyst containing 1.75 wt.% of coke, 0.65 wt. % Fe, 950 ppm Ni, and 70 ppm V. The catalyst was selected from a database of equilibrium FCC catalysts based on its high carbon content.

Material and Methods

Catalyst particles were sieved to obtain a sieve fraction of 38-76 μm. Crushed catalyst material was obtained by crushing the FCC particles in a mortar.

We conducted solid-state NMR experiments at room temperature (293 K) and under low temperature (100K) DNP conditions using 3.2 mm triple-resonance (^{1}H, ^{13}C, ^{15}N) magic-angle-spinning (MAS) probe heads in static magnetic fields of 9.4 and 18.8 T, corresponding to proton/electron resonance frequencies of 400 MHz/263 GHz and 800 MHz/527 GHz (Bruker BioSpin, [32]), respectively DNP samples were prepared by wetting [33,34] using a solution of 15mM Pypol [35] in tetrachloroethane.

For SEM measurements, the FCC particle was deposited on an aluminum stub and fixed by means of a carbon slab. Subsequently a thin Au/Pd layer of 15 nm thick was sputtered on the particle in order to prevent charging in the SEM. The image was measured using a secondary electron detector. Secondary electron images are especially suited for showing surface morphology. In order to be able to measure cross sections on the sample, a number of representative FCC particles were imbedded in resin, grinded/polished and coated with a carbon layer of about 5 nm thick.

EPR spectra were recorded on a Bruker EMX Plus, 6000 Gauss machine, with an ER 041 XG X-Band Microwave Bridge at 100 K with a frequency of 9.419 GHz, using quartz sample tubes.

Results

In Figure 5.2A, we compare DNP results obtained at 400 MHz for whole (Figure 5.2A, top lines) and crushed (Figure 5.2A, middle lines) FCC samples in reference to the free solvent. From the experimentally detected ^{13}C chemical shifts as well as from ^{1}H chemical shifts derived from an (^{1}H,^{13}C) FLSG-HETCOR [36] spectrum conducted under DNP conditions (Figure 5.2B), we concluded, in line with earlier work [7,8,28], that our ^{13}C spectra are dominated by aliphatic and aromatic ^{13}C moieties. Note that ^{13}C signals at about 150 ppm are missing in the HETCOR experiment that was recorded using a short Cross Polarization (CP) contact time, in line with the absence of quaternary carbons. As presented in Figure 5.1A, we observed relative DNP signal enhancements varying between 2.5 and 4.6, with higher enhancements generally observed for crushed FCC particles. While the relative signal enhancement for aromatic resonances only changed by about 13 % between both preparations, we observed a significant increase of about 43% for the aliphatic peaks around 40 ppm. Assuming that the DNP enhancement is largely confined to the surface of our preparations (due to the low proton density) [37-39], these results suggest that a significant portion of aliphatic carbon must be embedded within the FCC particle and only becomes DNP active, i.e., solvent exposed, after crushing. Barth et al. [7] and Qian et al. [8] assume that the aliphatic carbon and aromatic carbon are always constituent of the same molecules. Our results indicate that this is not necessarily the case.

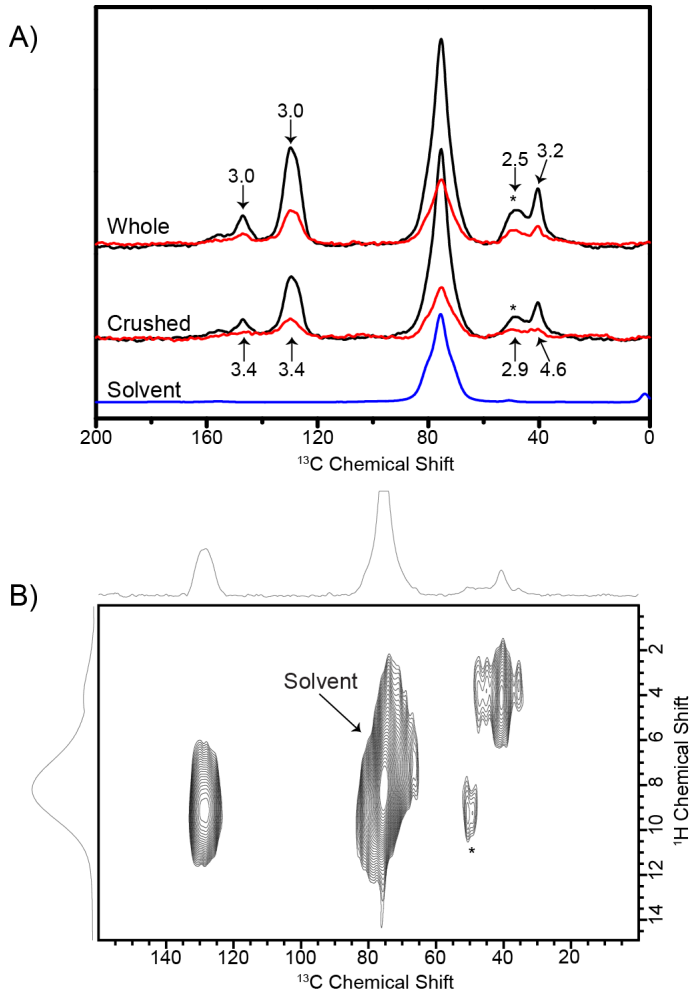

Figure 5.2. A) ^{13}C CP-MAS spectra (using a CP contact time of 2ms) measured on a 400 MHz DNP system (Bruker Biospin) at 100 K. Black represents spectra with irradiation of microwaves and red represents spectra without irradiation of microwaves. The top black and red lines are recorded on whole FCC particles, while the middle black and red spectra are recorded on crushed FCC particles. The blue spectrum is recorded on just the solvent used for wetting the sample. The number indicated represent the DNP-enhancements computed from the intensity ratios of on- and off-DNP experiments; B) FLSG-HETCOR spectrum [36] of whole FCC particles under DNP condition using a short CP contact time of 50 µs.

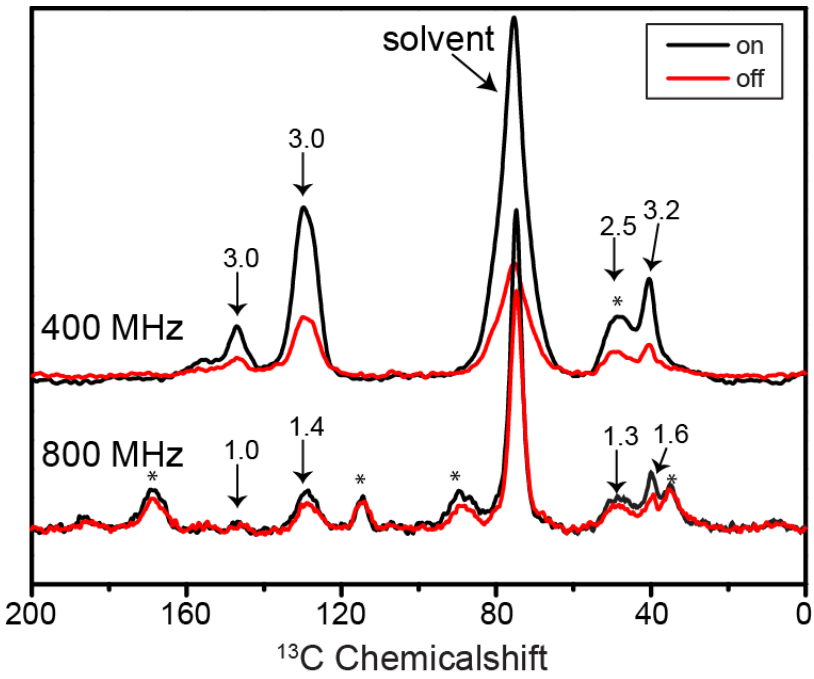

Figure 5.3. ^{13}C CP-MAS spectra measured with the 400 MHz (top spectra) and 800 MHz (bottom spectra) DNP system at 100 K. Black lines represent the spectra with irradiation of microwaves, red lines represent spectra without irradiation of microwaves. MAS sidebands are indicated by *.

Next, we examined whole FCC particles under 800 MHz/527 GHz DNP conditions and compared the results obtained to the 400 MHz DNP case. This is shown in Figure 5.3. Including MAS sideband intensities at higher B_0 field, the relative NMR signal intensity between the aromatic and aliphatic signals remained largely constant. As expected [40], DNP enhancements were reduced at 800 MHz compared to the data obtained at 400 MHz. In line with earlier results, the observed reduction was lower than that observed for AMUpol [35] which may be due to the smaller molecular size of Pypol leading to an, on average, stronger hyper fine coupling that determines the DNP transfer efficiency [40].

Finally, we examined the influence of the biradical itself on our solid-state NMR spectra for two different temperatures. The results are shown in Figure 5.4. In the absence of biradicals, the spectrum is dominated by aromatic signals both at high and lower temperatures and the relative increase in signal intensity is in line with thermodynamic predictions. Upon addition

of Pypol, signal intensities strongly increase at lower temperatures (factor 40 in Figure 5.4) and aliphatic contributions appeared that remained largely invisible in the absence of the biradical.

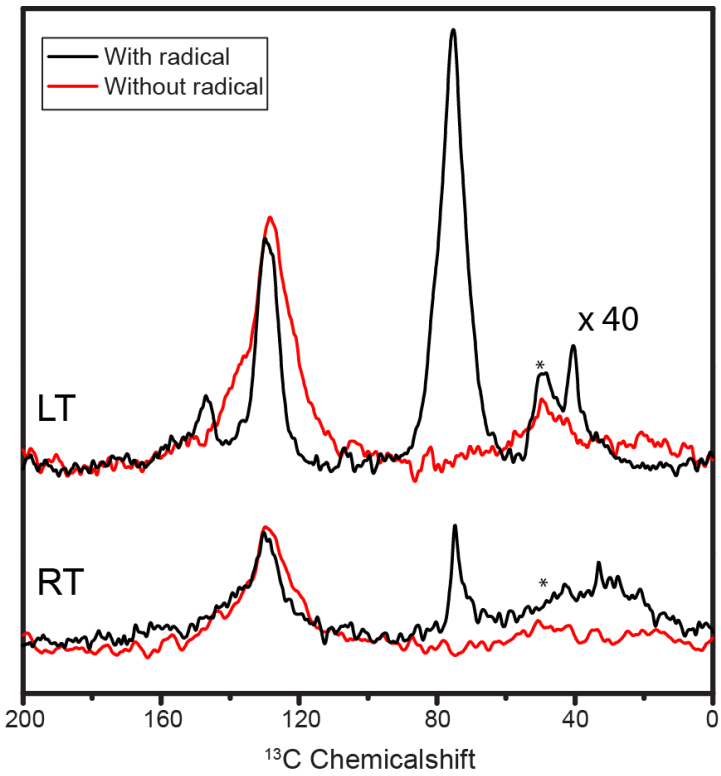

Figure 5.4: ^{13}C CP-MAS spectra of FCC particles measured with the 400 MHz DNP system without microwaves. Black lines represent the spectra of the sample with added radical and red lines represent spectra measured without radical. The top lines (LT) represent the spectra measured at 100 K, the bottom lines (RT) depict the spectra measured at 293 K. All spectra were recorded with 40960 scans except for the sample with radical and at 100 K where 1024 scans were used.

These results obtained in the absence of radical can be explained by (a) a dominant aromatic coke contribution compared to aliphatic species or (b) favourable relaxation properties for aromatic species possibly due to paramagnetic effects resulting from the proximity of e.g. metal(ion) species, such as Fe, V or Ni species. Upon addition of biradicals, surface species become dominant and they both contain aromatic and aliphatic ^{13}C moieties.

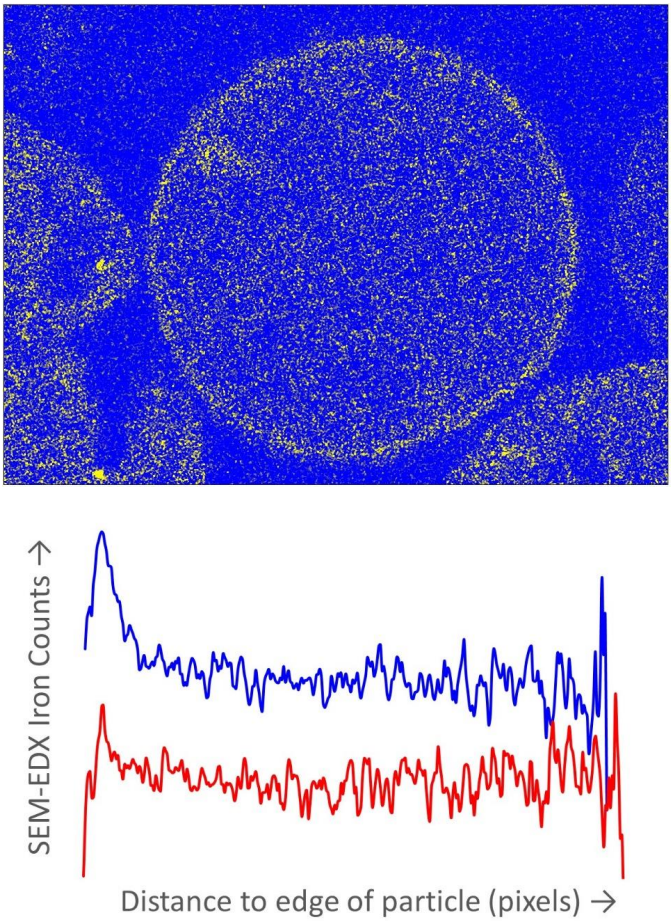

Figure 5.5. SEM-EDX analysis of iron distribution in FCC particles. The left panel shows an iron color-coded image. A relative concentration in the outer shell is obvious. The right image shows a radial distribution of iron as a function of distance to the edge of the particle (outer edge is to the left) for two different FCC particles.

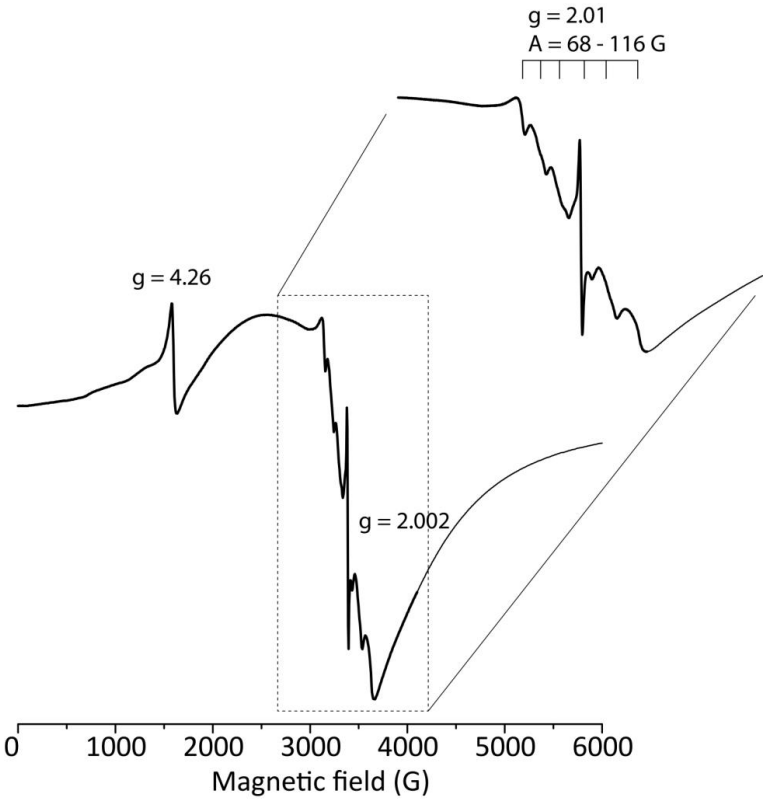

Figure 5.6. broad sweep X-band EPR spectrum of the catalyst sample recorded at 100 K. The bulk of the signal with features at g=4.26 and g=2.01 can be attributed to iron species. The fine structure on the signal around g=2.1 can be attributed to a small Mn(II) impurity, the sharp signal at g=2.002 is attributed to an organic radical in the coke.

Previous work using Transmission X-ray Microscopy (TXM), X-ray Fluorescence (XRF), Scanning Transmission X-ray Microscopy (STXM) and SEM has yielded strong evidence for the concentration of Fe and Ni in an outer shell of FCC equilibrium catalyst particles [24,42-48]. In order to corroborate these findings, we have conducted SEM-EDX analysis of the FCC catalyst material used in the NMR-studies. We find an increased concentration of iron in the outer shell with some variations between individual particles (see Figure 5.5). Since the sample is an equilibrium catalyst with an age-distribution, it is not unexpected that the intra-particle metal distribution and inter-particle concentrations vary between the FCC particles. In addition,

we have performed EPR experiments, which show that iron is the dominant paramagnetic species present in the FCC catalyst particles (see Figure 5.6). The EPR shows a minor contribution from Mn, which is confirmed by SEM-EDX. The DNP experiments indicate a concentration of aromatic coke at the outside of the FCC particles, while SEM-EDX and EPR indicate that paramagnetic iron species are also concentrated at the outside of the FCC particles. The combination of these two sets of observations suggests that the effect observed in Figure 5.4 can be explained mainly by paramagnetic relaxation effects.

Conclusions

We have described a tailored solid-state NMR approach, supported by EPR and SEM-EDX, that provides insight into the molecular environment of ^{13}C coke species: aromatic groups are largely surface exposed and contain a significant fraction that most likely is located close to paramagnetic species, such as Fe. Likewise, aliphatic coke species are located at the surface of the FCC particle but they can also be found in the interior of the FCC particle and are located more distant from paramagnetic species compared to aromatic species. These experimental observations support a model where large heteroaromatic carbon species are preferentially deposited on the outer surface of the catalyst, and catalytic coke, more aliphatic in nature, is formed inside the catalyst particle.

Our studies also showcase the beneficial effect of using DNP in the context of in-situ solid-state NMR material science studies providing the spectroscopic basis for further in-depth studies of FCC catalyst particles, for instance by studying the effect of catalyst age on carbon deposition and formation, as well as more detailed localization and speciation of the carbon inside the catalyst particles as a function of catalyst age.

References

[1] E. Vogt and B. Weckhuysen, "Fluid catalytic cracking: recent developments on the grand old lady of zeolite catalysis," *Chem. Soc Rev.*, vol. 44, pp. 7342-7370, 2015.

[2] Y. Mathieu, A. Corma, M. Echard and M. Bories, *Appl. Catal. A: General*, vol. 269, pp. 451-465, 2014.

[3] A. Corma, L. Sauvanaud, E. Doskocil and G. Yaluris, *J. Catal.*, vol. 279, pp. 183-195, 2011.

[4] H. Karge, "Coke Formation on Zeolites," *Stud. Surf. Sci. Catal.*, , vol. 137, pp. 707-746, 2001.

[5] M. Guisnet and P. Magnoux, "Coking and deactivation of zeolites - Influence of the pore structure," *Appl. Catal.*, vol. 54, pp. 1-27, 1989.

[6] O. Bayraktar and E. L. Kugler, "Characterization of coke on equilibrium fluid catalytic cracking catalysts by temperature-programmed oxidation," *Appl. Catal. A: General*, vol. 233, pp. 197-213, 2002.

[7] J.-O. Barth, A. Jentys and J. Lercher, *Ind. Eng. Chem. Res.*, vol. 43, pp. 2368-2375, 2004.

[8] K. Qian, D. Tomczak, E. Rakiewicz, R. Harding, G. Yaluris, W. Cheng, X. Zhao and A. Peters, *Energy Fuels*, vol. 11, pp. 596-601, 1997.

[9] A. Fonseca, P. Zeuthen and J. Nagy, *Fuel*, vol. 75, pp. 1413-1423, 1996.

[10] A. Fonseca, P. Zeuthen and J. Nagy, *Fuel*, vol. 75, pp. 1363-1376, 1996.

[11] A. Fonseca, P. Zeuthen and J. Nagy, *Fuel*, vol. 74, pp. 1267-1276, 1995.

[12] C. Snape, B. McGhee, J. Andresen, R. Hughes, C. Koon and C. Hutchings, *Appl. Catal.*, vol. 129, pp. 125-132, 1995.

[13] D. Mores, J. Kornatowksi, U. Olsbye and B. Weckhuysen, "Coke formation during the methanol-to-olefin conversion: In situ microspectroscopy on individual H-ZSM-5 crystals with different brønsted acidity," *Chem. Eur. J.*, vol. 17, pp. 2874-2884, 2011.

[14] D. Mores, E. Stavitski, M. Kox, J. Kornatowski, U. Olsbye and B. Weckhuysen, "Space- And time-resolved in-situ spectroscopy on the coke formation in molecular sieves: Methanol-to-olefin conversion over H-ZSM-5 and H-SAPO-34," Chem. Eur. J., vol. 14, pp. 11320-11327, 2008.

[15] H. Shimada, M. Imamura, N. Matsubayashi, T. Saito and T. Tanaka, "Characterization of coke deposited on catalysts by Carbon K-edge Near Edge X-ray Absorption Fine Structure (NEXAFS) spectroscopy," Top. Catal., vol. 10, pp. 265-271, 2000.

[16] M. Smith and R. Lobo, "The local and surface structure of ordered mesoporous carbons from nitrogen sorption, NEXAFS and synchrotron radaiation studies," Microporous Mesoprous Mater., vol. 92, pp. 81-93, 2006.

[17] S. Davis, Y. Zhou, M. Freeman, D. Fischer, G. Meitzner and J. Gland, J. Catal., vol. 139, pp. 322-325, 1992.

[18] P. Gallezot, C. Leclercq, J. Barbier and P. Marecot, J. Catal., vol. 116, pp. 164-170, 1989.

[19] N.-K. Bär, F. Bauer, D. Ruthven and B. Balcom, "Direct and indirect observation of coke deposits on H-ZSM-5 by 1H NMR imaging," J. Catal., vol. 208, pp. 224-228, 2002.

[20] B. Anderson, R. van Santen and L. van IJzendoorn, Appl. Catal. A: General, vol. 160, pp. 125-138, 1997.

[21] J. Barth, A. Jantys and J. Lercher, Ind. Eng.Chem. Res., vol. 43, pp. 3097-3104, 2004.

[22] M. Den Hollander, M. Makkee and J. Moulijn, "Coke Formation in Fluid Catalytic Cracking Studied with the Microriser," Catal. Today, vol. 46, pp. 27-35, 1998.

[23] M. Den Hollander, M. Makkee and J. Moulijn, "Coke Formation in Fluid Catalytic Cracking," Stud. Surf. Sci. Catal., vol. 111, pp. 295-302, 1997.

[24] X. Dupain, M. Makkee and J. Moulijn, "Optimal Conditions in Fluid Catalytic Cracking, A Mechanistic Approach," Appl. Catal., A: General, vol. 297, pp. 198-219, 2006.

[25] J. Hofmann, D. Mores, L. Aramburo, S. Teketel, M. Rohnke, J. Janek, U. Olsbye and B. Weckhuysen, "Large zeolite H-ZSM-5 crystals as models for the methanol-to-hydrocarbons process : bridging the gap between single-particle examination and bulk catalyst analysis," Chem. Eur. J., vol. 19, pp. 8533-8542, 2013.

[26] M. Callejas, M. B. T. Martínez and E. Sastre, "Coke characterisation in aged residue hydrotreating catalysts by solid-state 13C-NMR spectroscopy and temperature-programmed oxidation," Appl. Catal. A: General, vol. 218, pp. 181-188, 2001.

[27] H. Cerqueira, G. Caeiro, L. Costa and F. Ramôa Ribeiro, "Deactivation of FCC Catalysts," J. Mol. Catal. A, vol. 292, pp. 1-13, 2008.

[28] H. Cerqueira, C. Sievers, G. Joly, P. Magnoux and J. Lercher, Ind. Eng. Chem. Res., vol. 44, pp. 2069-2077, 2005.

[29] E. Andrew, A. Bradbury and R. Eades, Nature, vol. 182, p. 1659, 1958.

[30] A. Overhauser, Phys. Rev., vol. 92, pp. 411-415, 1953.

[31] N. Q.Z., E. Daviso, T. Can, J. Herzfeld and R. Griffin, Acc. Chem. Res., vol. 46, pp. 1933-1941, 2013.

[32] E. Koers, E. van der Cruyssen, M. Rosay, M. Weingarth, A. Prokofyev, C. Sauvee, O. Ouari, J. van der Zwan, O. Pongs, P. Tordo, W. Maas and M. Baldus, J. Biomol. NMR, vol. 60, pp. 157-168, 2014.

[33] J. Haber, J. Block and B. Delmon, Pure Appl. Chem., vol. 67, p. 1257, 1995.

[34] A. Lesage, M. Lelli, D. Gajan, M. Caporini, V. Vitztum, P. Miéville, J. Alauzin, A. Roussy, C. Thieuleux, A. Mehdi, G. Bodenhausen, C. Coperet and L. Emsley, J. Am. Chem. Soc., vol. 132, pp. 15459-15461, 2010.

[35] C. Sauvee, M. Rosay, G. Casano, F. Aussenac, R. Weber, O. Ouari and P. Tordo, Angew. Chem., Int. Ed., vol. 52, pp. 10858-10861, 2013.

[36] B.-J. Van Rossum, H. Förster and H. de Groot, Magn. Reson., vol. 124, pp. 516-519, 1997.

[37] P. van der Wel, K.-N. Hu, J. Lewandowski and R. Griffin, J. Am. Chem. Soc., vol. 128, pp. 10840-10846, 2006.

[38] A. Rossini, A. Zagdoun, M. Lelli, A. Lesage, C. Copéret and L. Emsley, Acc. Chem. Res., vol. 46, pp. 1942-1951, 2013.

[39] A. Jantschke, E. Koers, D. Mance, M. Weingarth, E. Brunner and M. Baldus, Angew. Chem., Int. Ed., vol. 54, pp. 15069-15073, 2015.

[40] D. Mance, P. Gast, M. Huber, M. Baldus and K. Ivanov, J. Chem. Phys., vol. 142, p. 234201, 2015.

[41] F. Meirer, S. Kalirai, D. Morris, S. Soparawalla, Y. Liu, G. Mesu, J. Andrews and B. Weckhuysen, "Life and death of a single catalytic cracking particle," Sci. Adv., vol. 1, p. e1400199, 2015.

[42] Y. Liu, F. Meirer, C. Krest, S. Webb and B. Weckhuysen, Nat. Commun., vol. 7, p. 12634, 2016.

[43] F. Meirer, S. Kalirai, J. N. Weker, Y. Liu, J. C. Andrews and B. M. Weckhuysen, "Agglutination of single catalyst particles during fluid catalytic cracking as observed by X-ray nanotomography," Chem. Commun., vol. 51, pp. 8097-8100, 2015.

[44] F. Meirer, D. Morris, S. Kalirai, Y. Liu, J. Andrews and B. Weckhuysen, J. Am. Chem. Soc., vol. 137, pp. 102-105, 2015.

[45] S. Kalirai, U. Boesenberg, G. Falkenberg, F. Meirer and B. Weckhuysen, "X-ray Fluorescence Tomography of Aged Fluid-Catalytic- Cracking Catalyst Particles Reveals Insight into Metal Deposition Processes," ChemCatChem, pp. 3674-3682, 2015.

[46] A. Wise, J. Weker, S. Kalirai, M. Farmand, D. Shapiro, F. Meirer and B. Weckhuysen, ACS Catal., vol. 6, pp. 2178-2181, 2016.

[47] S. Kalirai, P. Paalanan, J. Wang, F. Meirer and B. Weckhuysen, Angew. Chem., Int. Ed., vol. 55, pp. 11134-11138, 2016.

[48] E. Rautiainen and B. Nelissen, Hydrocarb. Eng., pp. 41-47, April 2013.

CHAPTER 6

Improving Cross-effect DNP efficiency at 800 MHz/527GHz using Trityl-Nitroxide biradicals

Introduction

Dynamic Nuclear Polarization (DNP) has become a valuable tool in enhancing the NMR sensitivity of the sample of interest in the context of both material- and life-science applications. Due to the size and complexity of certain (bio)molecules, sensitivity can become a serious limitation for conventional NMR experiments. However with the use of DNP, it is possible to overcome this obstacle, enabling structural insight to be obtained in systems previously inaccessible by NMR [1–7]. Although initially solid-effect DNP which can be established using mono-radicals[8] such as TEMPO or BDPA was used, it was later shown that using tethered TEMPO binitroxides such as TOTAPOL[9,10] that facilitate cross effect DNP, give a much higher enhancement under MAS conditions. Therefore, cross effect DNP has become the preferred mechanism for signal enhancement. This mechanism requires an EPR frequency separation between the 2 electron spins which should match the nuclear Larmor frequency of the proton, ω_{e1}-ω_{e2}= $\pm\omega_H$ (see also chapters 1 and 3). Optimizing the polarization transfer that can occur at this condition led to the development of AMUPol[11] and TEKPol[12] which have larger dipolar couplings between the electrons and longer relaxation times[13,14]. Simulations have shown that both factors influence the DNP enhancement[15–17]. However, despite the enhancement increase, these biradicals tend to have an unfavourable field dependence, since as the field is increased, the measured enhancement tends to decrease. The decrease in enhancement as the field is increased follows approximately $1/B_0^2$. For various applications, there is a preference in performing experiments at high magnetic fields where spectral resolution can be maximized[2,4,18]. Due to the unfavourable field dependence, the full potential of high-field DNP thus far could not be realized. Therefore, results obtained of a set of Trityls tethered with a Nitroxide radical were particularly interesting[10,19,20], since an increase in magnetic field strength did not decrease DNP enhancements for some of the radicals tested. Further studies of these trityl-nitroxide biradicals can hence be of significant importance for further developing high-field DNP radicals. Previous work has already shown that by combining parameters including spin-couplings and relaxation times obtained from EPR in combination with a quantum mechanical treatment based on solving the Liouville-von Neumann provides an accurate description of the field dependence in the case of AMUPol[16]. Here we will apply a similar approach to further examine the EPR properties of trityl-nitroxides and test new radicals with an improved water solubility allowing these radicals to also give a sizable enhancement with a 14kDa protein at high magnetic fields.

Material and Methods

NMR Samples were prepared using various trityl-nitroxides as DNP agents. A biradical concentration of 10 mM was used. As a solvent, we used a D_8-glycerol/D_2O/H_2O mixture with a volume ratio of 60/30/10. Solid-state NMR and DNP experiments were conducted using 3.2 mm triple-resonance (^1H, ^{13}C, ^{15}N) MAS probe heads at static magnetic fields of 18.8 T corresponding to the proton/electron resonance frequencies of 800 MHz/527 GHz (Bruker BioSpin). The EPR measurements were performed at 100 K, using a spectrometer operating at 275.7 GHz[21,22].

Results

In Figure 6.1a and Table 6.1 the molecular structures and results of DNP measurements at 800 MHz are shown for the previously reported[19] trityl-nitroxide radicals. Note the significant variation in measured DNP enhancements between the different radicals and magnetic fields, shown in Figure 6.2. At 211MHz these radicals do give a sizable enhancement up to ε=75 but compared to AMUPol these values are about a factor 3 lower. When moving to higher magnetic field a maximum of ε=87 is observed at 600MHz, which is closer to what is obtained for AMUPol (ε=128)[11]. Finally, comparing the performance of these radicals at 800MHz we see that they can provide higher enhancements (ε=65) compared to AMUPol (ε=40). It is therefore interesting to understand this peculiar field dependence of these biradicals, which will be investigated with simulations below. From previous considerations[17,23,24] it was shown that the three-spin mixing depends on the sum of the spin-spin interactions squared, $(D+J)^2$. These derivations would indicate that for an efficient mixing between the states the spin-spin interactions would need to be as large as possible. However, when comparing this notion to the J-couplings measured for the radicals (Table 6.1), it can be seen that this is not the case. A possible interpretation would be that as spin interactions increased beyond a certain value, the matching condition for cross effect $\omega_{e1}-\omega_{e2}= \pm\omega_H$ will no longer be fulfilled leading to a decrease in mixing efficiency. Correspondingly, different J-couplings would have an optimum DNP enhancement at a different magnetic field.

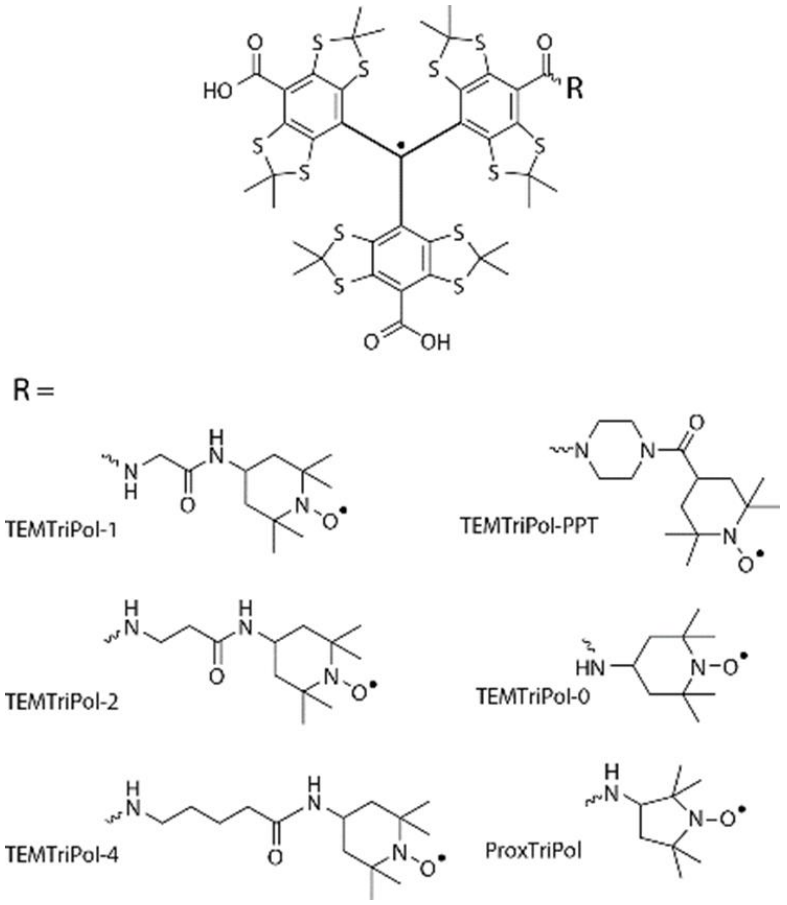

Figure 6.1. Molecular structures of the TEMTriPol biradicals tested (adapted from ref[19]) for cross-effect ^{1}H DNP.

Biradical	ε at 800MHz	ε at 600MHz	ε at 211MHz	J-couplingMHz
TEMTripol-0	6	-	7	441
TEMTripol-1 (GT)	65	87	50	73
TEMTripol-2	27	43	27	89
TEMTripol-4	12	23	35	46
TEMTripol-PPT	46	65	75	3,36
ProxTriPol	0	-	6	820

Table 6.1 Results of cross-effect DNP NMR experiments at 211, 600, and 800 MHz with the TEMTriPol biradicals shown in Figure 6.1 (adapted from ref[19]) DNP experiments were performed on samples containing 1M ^{13}C-urea in [D^8]-glycerol:D_2O:H_2O 60:30:10 v:v:v and 10 mM biradical.

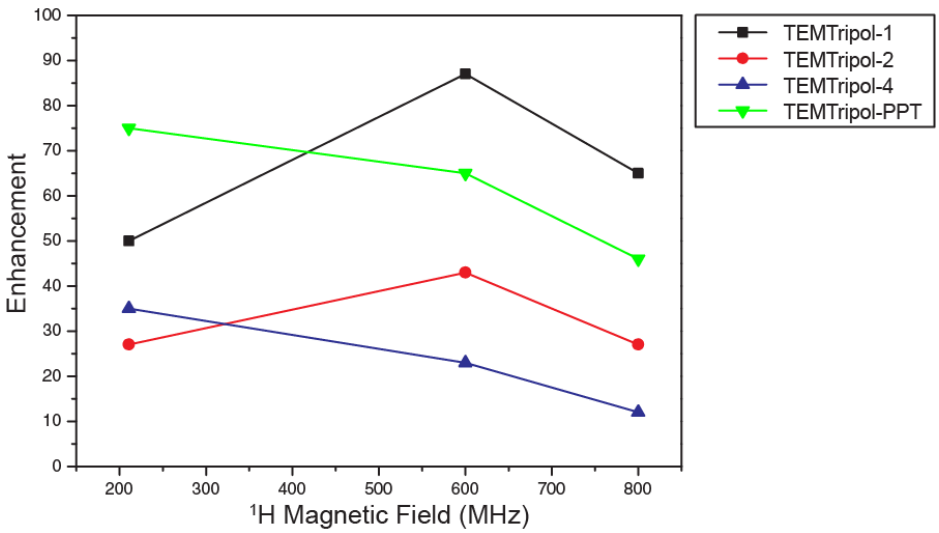

Figure 6.2. DNP Enhancement measured at different magnetic fields for the Trityl-Nitroxide radicals shown in Table 6.1 and Figure 6.1.

For testing the radicals shown in Figure 6.1 using a membrane protein (KcsA) requires reducing the glycerol content of the solution as is typically done for DNP experiments with membrane proteins. For the case of TEMTripol-1, this procedure led to solubility problems and an enhancement of 3 for this sample. Therefore, variants of these biradicals were synthesized by the group of Yangping Liu shown in Figure 6.3. with the aim to increase their solubility in water. The results of measurements done with these radicals at 800MHz are shown in Table 6.2. Using various substitutes on the linker between the nitroxide and trityl it was possible to increased water solubility of these radicals and obtain even higher enhancements compared to the radicals shown in Table 6.1 Also, it was possible to obtain sizable enhancements of ε=26 at 800 MHz on a protein (7d12 nanobody) using these radicals. Furthermore, Huber et al. determined EPR relaxation times at 275 GHz for 2 of these compounds (see Table 6.2) that were similar, suggesting that the electron relaxation time is not responsible for the observed variations in DNP enhancement.

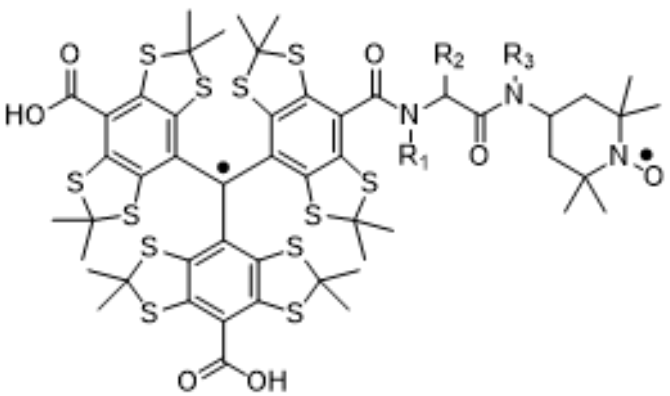

Figure 6.3. Trityl-nitroxide radicals synthesized by the group of Yangping Liu et al. with improved water solubility.

Biradical	ε at 800MHz	T_{1e} (Trityl)	T_{2e} (Trityl)
GT (TEMTripol-1)	57	300µs	650ns
GTM	66	300(65µs)	600ns
GTB	33		
GTNM	36		
GTNOH	87		
GTM with 7d12 nanobody	26		

Tabel 6.2 Results of cross effect DNP NMR experiments at 800 MHz (left columns) and EPR relaxation measurements (right 2 columns) for radical shown in Figure 6.3. DNP experiments were performed on samples containing 0.25 M ^{13}C-^{15}N-proline in [D^8]-glycerol:D_2O:H_2O 60:30:10 v:v:v and 10 mM biradical. Note that in general Urea samples give higher enhancements then proline samples due to improved glass formation.

Calculations of DNP enhancements

DNP simulations conducted in the context of the present study followed our earlier publication[16] with the exception that an additional term was added to the Hamiltonian representing the exchange coupling J_{ab} between electrons a and b, resulting the total time-dependent Hamiltonian

$$\begin{aligned}\hat{H}(t) = {} & \Delta\omega_a\hat{S}_{az} + \Delta\omega_b\hat{S}_{bz} + \omega_n\hat{I}_z + \omega_1\{\hat{S}_{ax}+\hat{S}_{bx}\} \\ & + D_{ab}\{2\hat{S}_{az}\hat{S}_{bz} - \hat{S}_{ax}\hat{S}_{bx} - \hat{S}_{ay}\hat{S}_{by}\} \\ & + A_{zz}\hat{S}_{az}\hat{I}_z + A_{zx}\hat{S}_{az}\hat{I}_x + A_{zy}\hat{S}_{az}\hat{I}_y \\ & + J_{ab}\{\hat{S}_{ax}\hat{S}_{bx} + \hat{S}_{ay}\hat{S}_{by} + \hat{S}_{az}\hat{S}_{bz}\}\end{aligned} \qquad (6.1)$$

$\Delta\omega_a$ and $\Delta\omega_b$ represent the electron-Zeeman interaction in the rotating frame (with $\Delta\omega_{a,b}=\omega_{a,b}-\omega_{mw}$ and ω_{mw} is equal to the microwave frequency). In addition, ω_n stands for the nuclear-Zeeman interaction, ω_1 is the field strength of the microwave, D_{ab} the dipolar electron-electron interaction and A_{zz}, A_{zx} and A_{zy} are the secular and pseudo-secular hyperfine interaction (HFI) terms. For each timestep of a single rotor period, we calculated the relaxation rates and

interactions after rotating from the principal axis system (PAS) to the laboratory frame. After a single rotor period was completed, an evolution super-operator can be defined which can be applied to the initial density matrix to calculate subsequent rotor-cycles.

As discussed before (see chapter 3), this approach enables us to determine the behavior of MAS-DNP at high magnetic fields and characterize the relative performance of the MAS-DNP polarizing agents. We attribute the observed dependence of the enhancement to electron nuclear polarization transfer occurring at CE level anti-crossings upon spinning of the sample. The transfer efficiency at such "rotor events" is proportional to the square of the electron-electron spin-spin interaction. The effect of this interaction is less pronounced at lower fields, where the DNP effect is higher (i.e., it tends to saturate at the value of ≈ 660, the ratio of the electron and proton gyromagnetic ratios) but manifest at higher fields (i.e., as the overall enhancements decreases).

Parameter	**Value**
Field	Varied from 200MHz to 800MHz
Microwave	263.45GHz
Microwave	0.85MHz
D_{ee}	18.5MHz
$J_{exchange}$	Varied from 0 to 280MHz
T_{1e} Trityl	300us
T_{1e} Nitroxide	60us
T_{2e} Trityl	600ns
T_{2e} Nitroxide	770ns
T_{1n}	2sec
T_{2n}	1msec
HFI	Varied from 0.023MHz (15A) to 3MHz (3A)

Tabel 6.3. Parameters used for simulations

Figure 6.3a shows simulations performed with the parameters available for the trityl-nitroxide biradical as shown in Table 6.3. It is seen that there appears to be an optimal J-coupling at each magnetic field and that, as the magnetic field increases, optimal DNP performance requires changes in the J-coupling. An explanation for this is that the J-coupling influences the matching conditions for cross-effect, $\omega_{e1}-\omega_{e2}= \pm\omega_H$. However, as the magnetic field is increased so do the relative electron frequencies. Thus, in order to fulfil the matching condition in an optimal manner the J-coupling should therefore also be increased further, this is in line with previous experimental work as shown in Table 6.1 where radicals with different J-couplings have various performances and field dependent profiles. In Figure 6.3b we see the field dependence assuming a J-coupling of 80MHz for various HFI's. Similar as in previous work simulating the field dependence of AMUPol[16] the relative performance of the biradicals under study is not reproduced by the calculation when considering a local nuclei with large hf-values, i.e. nuclei close to the unpaired electrons, as this leads to an overall enhancement which is close to saturation. However, we can reproduce the relative field dependence as was experimentally observed from Table 6.1, by considering relative weak HFI. As is clearly seen with for example TEMTripol-1 which has a similar J-coupling as the simulation that initially there is an increase in enhancement and as the magnetic field is increased and then as it further increases it starts to drop off. This effect is only observed when thus considering the weaker HFI.

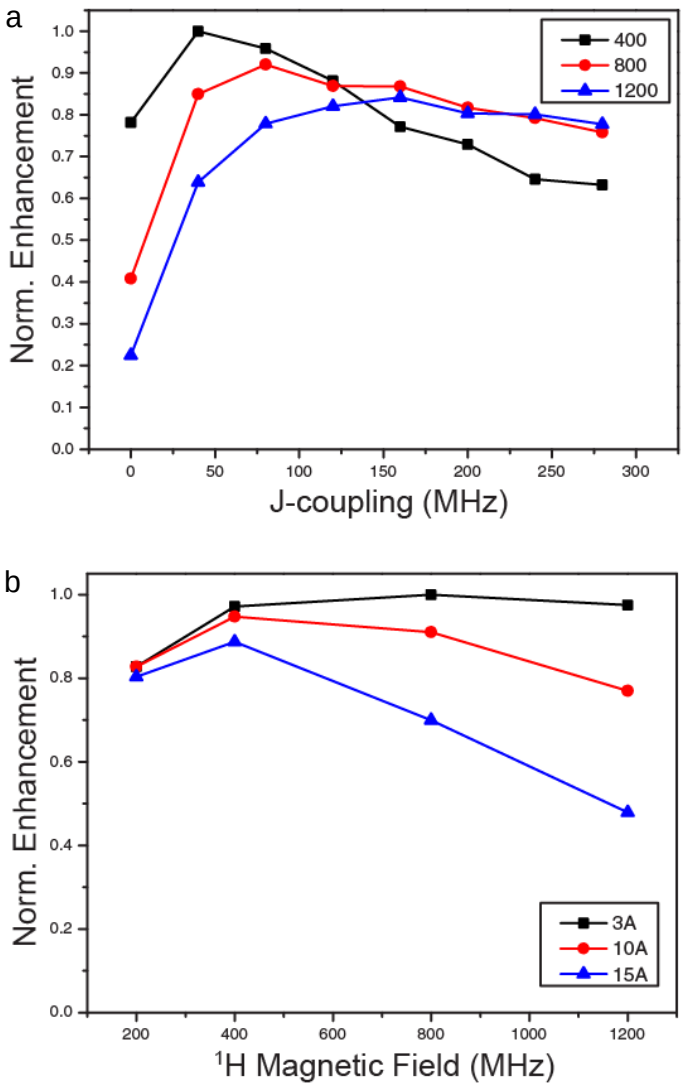

Figure 6.3: DNP simulations based on the parameters shown in Table 6.3 average over 343 orientations. a) Simulation was done for 3 different magnetic fields 400, 800 and 1200MHz with varying J-couplings using a hyperfine interaction of 0.08MHz. b) Simulations with varying HFI's corresponding to 3, 10 and 15Å distances with a J-coupling of 80MHz.

Conclusions

We have shown experimental observed enhancements on mixed radicals which are built from a tethered trityl and nitroxide. These compounds allow for overall better performance than the binitroxide radicals at higher magnetic fields. With the introduction of improved water soluble versions of these radicals it was possible to obtain sizable enhancements on a protein sample at the 800MHz DNP system. Furthermore, from simulations it is shown (Figure 6.3a) that for these radicals when only dipolar couplings (and thus J=0 MHz) are considered in the simulations a similar field dependence is obtained as for the case of binitroxides and it is only due to the sizable J-coupling (and weaker HFI's) which influences the matching condition for cross-effect that the field dependence has this particular behaviour. Especially concerning DNP experiments at even higher magnetic fields it would be expected that the performance of the binitroxides would further decrease and that at least for the cross-effect mechanism, biradicals with a sizable J-coupling such as the trityl-nitroxides would be the preferred choice.

References

[1] M. Kaplan, A. Cukkemane, G. C. P. van Zundert, S. Narasimhan, M. Daniëls, D. Mance, G. Waksman, A. M. J. J. Bonvin, R. Fronzes, G. E. Folkers, et al., *Nat. Methods* **2015**, *12*, 649–652.

[2] M. Kaplan, S. Narasimhan, C. de Heus, D. Mance, S. van Doorn, K. Houben, D. Popov-Čeleketić, R. Damman, E. A. Katrukha, P. Jain, et al., *Cell* **2016**, *167*, 1241–1251.e11.

[3] M. J. Bayro, G. T. Debelouchina, M. T. Eddy, N. R. Birkett, C. E. MacPhee, M. Rosay, W. E. Maas, C. M. Dobson, R. G. Griffin, *J. Am. Chem. Soc.* **2011**, *133*, 13967–13974.

[4] E. J. Koers, E. A. W. van der Cruijsen, M. Rosay, M. Weingarth, A. Prokofyev, C. Sauvée, O. Ouari, J. van der Zwan, O. Pongs, P. Tordo, et al., *J. Biomol. NMR* **2014**, *60*, 157–168.

[5] M. Lelli, D. Gajan, A. Lesage, M. A. Caporini, V. Vitzthum, P. Miéville, F. Héroguel, F. Rascón, A. Roussey, C. Thieuleux, et al., *J. Am. Chem. Soc.* **2011**, *133*, 2104–2107.

[6] A. J. Rossini, A. Zagdoun, M. Lelli, J. Canivet, S. Aguado, O. Ouari, P. Tordo, M. Rosay, W. E. Maas, C. Copéret, et al., *Angew. Chemie* **2012**, *124*, 127–131.

[7] M. Renault, S. Pawsey, M. P. Bos, E. J. Koers, D. Nand, R. Tommassen-van Boxtel, M. Rosay, J. Tommassen, W. E. Maas, M. Baldus, *Angew. Chemie Int. Ed.* **2012**, *51*, 2998–3001.

[8] L. R. Becerra, G. J. Gerfen, R. J. Temkin, D. J. Singel, R. G. Grisn, **1993**, *71*.

[9] C. Song, K.-N. Hu, C.-G. Joo, T. M. Swager, R. G. Griffin, *J. Am. Chem. Soc.* **2006**, *128*, 11385–90.

[10] K.-N. Hu, V. S. Bajaj, M. Rosay, R. G. Griffin, *J. Chem. Phys.* **2007**, *126*, 044512.

[11] C. Sauvée, M. Rosay, G. Casano, F. Aussenac, R. T. Weber, O. Ouari, P. Tordo, *Angew. Chemie Int. Ed.* **2013**, *52*, 10858–10861.

[12] A. Zagdoun, G. Casano, O. Ouari, M. Schwarzwä, A. J. Rossini, F. Aussenac, M. Yulikov, G. Jeschke, C. Copeet, A. Lesage, et al., *J. Am. Chem. Soc.* **2013**, *135*, 12790–12797.

[13] C. Sauvée, G. Casano, S. Abel, A. Rockenbauer, D. Akhmetzyanov, H. Karoui, D. Siri, F. Aussenac, W. Maas, R. T. Weber, et al., *Chem. - A Eur. J.* **2016**, *22*, 5598–5606.

[14] P. Gast, D. Mance, E. Zurlo, K. L. Ivanov, M. Baldus, M. Huber, *Phys. Chem. Chem. Phys.* **2017**, ***19***, 3777-3781.

[15] F. Mentink-Vigier, Ü. Akbey, Y. Hovav, S. Vega, H. Oschkinat, A. Feintuch, *J. Magn. Reson.* **2012**, *224*, 13–21.

[16] D. Mance, P. Gast, M. Huber, M. Baldus, K. L. Ivanov, *J. Chem. Phys.* **2015**, *142*, 234201.

[17] K. R. Thurber, R. Tycko, *J. Chem. Phys.* **2012**, *137*, 084508.

[18] P. Fricke, D. Mance, V. Chevelkov, K. Giller, S. Becker, M. Baldus, A. Lange, *J. Biomol. NMR* **2016**, *65*, 121–126.

[19] G. Mathies, M. A. Caporini, V. K. Michaelis, Y. Liu, K. N. Hu, D. Mance, J. L. Zweier, M. Rosay, M. Baldus, R. G. Griffin, *Angew. Chemie - Int. Ed.* **2015**, *54*, 11770–11774.

[20] Y. Liu, F. A. Villamena, A. Rockenbauer, Y. Song, J. L. Zweier, *J. Am. Chem. Soc.* **2013**, *135*, 2350–2356.

[21] H. Blok, J. A. J. M. Disselhorst, S. B. Orlinskii, J. Schmidt, *J. Magn. Reson.* **2004**, *166*, 92–99.

[22] G. Mathies, H. Blok, J. A. J. M. Disselhorst, P. Gast, H. van der Meer, D. M. Miedema, R. M. Almeida, J. J. G. Moura, W. R. Hagen, E. J. J. Groenen, *J. Magn. Reson.* **2011**, *210*, 126–132.

[23] T. V. Can, Q. Z. Ni, R. G. Griffin, *J. Magn. Reson.* **2015**, *253*, 23–35.

[24] S. Stoll, B. Epel, S. Vega, D. Goldfarb, *J. Chem. Phys.* **2007**, *127*, 164511.

CHAPTER 7

Summary and outlook

Summary and Outlook

In **chapter 2** it was shown how well resolved spectra with spectroscopic information about the side-chain can be obtained using ^{1}H-detection under fast MAS[1]. A typical requirement for ^{1}H-detected experiments under fast MAS is the need to reduce the ^{1}H-levels in a protein thereby suppressing the strong ^{1}H-dipolar-couplings. Such experiments are hence usually performed by per-deuterating the protein of interest and back exchanging exchangeable sites in the presence of water. This strategy results in only H^N signals being present in an ^{1}H ssNMR experiment and thus information about the side-chain is lost[2,3]. An alternative strategy shown in this chapter is modifying the growth medium which can lead to various amounts of incorporation of deuterium into the amino acids of a protein. In this chapter, it is shown how this method called fractional deuteration has allowed for detecting well resolved spectra comparable to per-deuteration for proteins while retaining side-chain protons, which can thus likewise be exploited in the experiments.

In **chapter 3** additional insight has been obtained into the cross effect mechanism being used for DNP. With DNP it is possible to increase sensitivity by several orders of magnitude. Under MAS, the prevalent mechanism so far involved in this process is the cross effect which requires the use of biradicals[4–7]. However, as the magnetic field is increased, the enhancements obtained decrease with approximately $1/B_0^2$[8–10]. The reason for this decrease was not well understood. Therefore, we conducted simulations that used a method similar to Mentink-Vigier and co-authors in Liouville space[7,11,12]. Our results were consistent with previous work and we specifically investigated the reason for the strong decrease in DNP efficiency when going to higher magnetic fields. For our calculations, we determined relaxation parameters by high field EPR 275GHz of the biradical using concentrations employed in our DNP experiments. Combining these parameters with the simulations revealed that weak electron-nuclei hyperfine interactions seem to be the main reason for the observed field dependence. We attribute this effect to the DNP enhancement depending on Level Anti Crossings (LACs)[7,11,12] which allows mixing between states and eventually leads to the observed enhancements. As the magnetic field is increased this leads to less efficient mixing conditions for these level anti-crossings resulting in an overall decrease in enhancement. When different hyperfine couplings were varied in the simulations it was shown that there was a strong dependence on this interaction. When strong hyperfine couplings were simulated the enhancements seemed to change only

slightly when changing the magnetic field. However, once weaker hyperfine interactions are considered, the simulated enhancements were in line with the experimentally observed enhancements. Therefore when considering the DNP mechanism, it is not the "core" nuclei that are important for the overall enhancement measured but the nuclei that are further away. The core nuclei still get polarized but are not involved in the spin-diffusion process which polarizes the whole sample. The presence of this spin-diffusion barrier was shown experimentally by the group of Pruski using various deuterated radicals[13].

Experimentally, DNP is widely applicable as shown in **chapter 4** but care has to be taken regarding the sample preparation. Firstly, looking at intact diatom biosilica[14] which consists of various molecular layers it was possible to identify the amino acids and to determine their backbone conformation in intact samples. Furthermore, by combining the measured enhancements with classical diffusion laws[15] it is possible to correlate the DNP enhancements measured from each layer with its thickness. Using such data, it is possible to suggest a supramolecular model of this system. Other large systems investigated were T4SScc[16] and EGFR[17], where in both cases a combination of selective amino acid isotope labelling and multi-dimensional (2D and 3D) ssNMR allow for probing such large systems and observing changes due to binding of a ligand in the case of EGFR. Finally, the potential of using site-directed spin-labels is shown[18,19], which allows the use of fully deuterated solvent[20] which prevents the polarization "leaking" to the solvent instead of the protein of interest, allowing in this case to obtain enhancements of ε=200 on a 14kDa protein.

In **chapter 5** we showed the application of DNP on a catalyst, namely Fluid Catalytic Cracking (FCC)[21]. FCC is used in oil refineries for the production of fuels like gasoline and petrochemical raw material such as propylene. During this process carbon species are deposited onto the FCC particle which deactivate the catalyst. By using DNP, it was shown that on this particle (which has a size between 38-76µm) it is possible to enhance the signal confirming that these species are mostly located on the surface[22]. However, comparing the results obtained using conventional and DNP NMR measurements along with differently prepared samples suggests that there are predominantly aliphatic carbon species present inside the particle as well. These results show the benefit of using DNP for in-situ solid-state NMR studies of materials allowing deposited carbon species to be detected as well as obtaining a better understanding regarding the localization of these species.

Finally, in **chapter 6** the importance of developing new radicals for high-field DNP was shown. Typically the DNP enhancements rapidly drop off as the magnetic field is increased when binitroxides such as AMUPol[6] or TOTAPOL[4] are used. However when testing new radicals consisting of a Trityl which gives a relative sharp line in the EPR spectrum and a Nitroxide which gives a much broader spectrum a more beneficial field dependence was observed[23]. These trityl-nitroxide biradicals tend to exhibit a sizable J-coupling which can be modified by chemically changing the connecting linker. When these radicals are tested at relative low field (211 MHz) their performance is inferior to the binitroxides mentioned above. However as the magnetic field is increased the enhancement tends to increase before dropping off again. The increase in enhancement is of particular interest since NMR measurements are preferably performed in high magnetic fields where the resolution is maximized. The combination of parameters from EPR measurements with simulations reveal that in particular the J-coupling is important and that the maximum enhancement obtained at each field has a different J-coupling. This observation can be attributed to the matching conditions required for cross-effect DNP[7].

As faster spinning rates become obtainable[24–26] the resolution in fully-protonated proteins spectra becomes comparable to the now used deuteration schemes with a decrease in requirement of sample quantity. This will allow for not only obtaining better resolved spectra, but will also benefit in obtaining side-chain information needed for assignments and obtaining contacts which is important for structure calculations. Apart of its application for biomolecules this could potentially have interesting applications for materials as well when investigating quadrupolar nuclei, since it would lead to a better averaging of the second-order quadrupolar interaction.

For DNP further development of radicals will be an important factor with the introduction of new biradicals for cross-effect DNP with an interesting dependence on the applied magnetic field. Apart of the cross-effect mechanism there have also been surprising results obtained with an alternative mechanism, namely Overhauser DNP. This mechanism showed an increase in enhancement as the magnetic field was increased[27]. However this mechanism so far is still less efficient than the enhancements obtained with cross effect DNP at 800MHz using binitroxides. Another aspect of DNP that will require further attention are the low temperatures which especially for protein samples can lead to broad ssNMR signals thereby complicating

the spectral analysis. Ongoing developments of a pulse microwave source could potentially provide ways to overcome the need of low-temperatures using the NOVEL scheme[28]. So far this has only been applied to low fields 0.35T. At this low-field significant enhancement can be obtained (>100) even at room-temperature and this mechanism is thought to be field independent and would thus be important for obtaining well resolved spectra of proteins. However, such pulsed DNP experiments will require the development of a (high power) pulsed microwave source at high-frequencies which have not been reported so far.

References

[1] D. Mance, T. Sinnige, M. Kaplan, S. Narasimhan, M. Daniëls, K. Houben, M. Baldus, M. Weingarth, *Angew. Chemie - Int. Ed.* **2015**, *54*, 15799–15803.

[2] R. Linser, M. Dasari, M. Hiller, V. Higman, U. Fink, J.-M. Lopez del Amo, S. Markovic, L. Handel, B. Kessler, P. Schmieder, et al., *Angew. Chemie Int. Ed.* **2011**, *50*, 4508–4512.

[3] V. Chevelkov, K. Rehbein, A. Diehl, B. Reif, *Angew. Chemie Int. Ed.* **2006**, *45*, 3878–3881.

[4] C. Song, K.-N. Hu, C.-G. Joo, T. M. Swager, R. G. Griffin, *J. Am. Chem. Soc.* **2006**, *128*, 11385–90.

[5] Y. Matsuki, T. Maly, O. Ouari, H. Karoui, F. Le Moigne, E. Rizzato, S. Lyubenova, J. Herzfeld, T. Prisner, P. Tordo, et al., *Angew. Chemie - Int. Ed.* **2009**, *48*, 4996–5000.

[6] C. Sauvée, M. Rosay, G. Casano, F. Aussenac, R. T. Weber, O. Ouari, P. Tordo, *Angew. Chemie Int. Ed.* **2013**, *52*, 10858–10861.

[7] K. R. Thurber, R. Tycko, *J. Chem. Phys.* **2012**, *137*, 1–14.

[8] E. J. Koers, E. a W. van der Cruijsen, M. Rosay, M. Weingarth, C. Prokofyev, Alexander Sauvée, O. Ouari, O. Pongs, P. Tordo, W. E. Maas, M. Baldus, *J. Biomol NMR* **2014**, *60*, 157–168.

[9] M. Kaplan, C. Pinto, K. Houben, M. Baldus, *Q. Rev. Biophys.* **2016**, *49*, DOI 10.1017/S003358351600010X.

[10] M. Kaplan, A. Cukkemane, G. C. P. van Zundert, S. Narasimhan, M. Daniëls, D. Mance, G. Waksman, A. M. J. J. Bonvin, R. Fronzes, G. E. Folkers, et al., *Nat. Methods* **2015**, *12*, 5–9.

[11] D. Mance, P. Gast, M. Huber, M. Baldus, K. L. Ivanov, *J. Chem. Phys.* **2015**, *142*, 234201.

[12] F. Mentink-Vigier, Ü. Akbey, Y. Hovav, S. Vega, H. Oschkinat, A. Feintuch, *J. Magn. Reson.* **2012**, *224*, 13–21.

[13] F. A. Perras, R. R. Reinig, I. I. Slowing, A. D. Sadow, M. Pruski, *Phys. Chem. Chem. Phys.* **2016**, *18*, 65–9.

[14] A. Jantschke, E. Koers, D. Mance, M. Weingarth, E. Brunner, M. Baldus, *Angew. Chemie - Int. Ed.* **2015**, *54*, 15069–15073.

[15] P. C. A. Van Der Wel, K.-N. Hu, J. Z. Lewandowski, R. G. Griffin, *J. Am. Chem. Soc.*

2006, *128*, 10840–10846.

[16] M. Kaplan, A. Cukkemane, G. C. P. van Zundert, S. Narasimhan, M. Daniëls, D. Mance, G. Waksman, A. M. J. J. Bonvin, R. Fronzes, G. E. Folkers, et al., *Nat. Methods* **2015**, *12*, 649–652.

[17] M. Kaplan, S. Narasimhan, C. de Heus, D. Mance, S. van Doorn, K. Houben, D. Popov-Čeleketić, R. Damman, E. A. Katrukha, P. Jain, et al., *Cell* **2016**, *167*, 1241–1251.e11.

[18] B. J. Wylie, B. G. Dzikovski, S. Pawsey, M. Caporini, M. Rosay, J. H. Freed, A. E. McDermott, *J. Biomol. NMR* **2015**, *61*, 361–7.

[19] E. A. W. van der Cruijsen, E. J. Koers, C. Sauvée, R. E. Hulse, M. Weingarth, O. Ouari, E. Perozo, P. Tordo, M. Baldus, *Chem. - A Eur. J.* **2015**, *21*, 12971–12977.

[20] T. Viennet, A. Viegas, A. Kuepper, S. Arens, V. Gelev, O. Petrov, T. N. Grossmann, H. Heise, M. Etzkorn, *Angew. Chemie - Int. Ed.* **2016**, *55*, 10746–10750.

[21] E. T. C. Vogt, B. M. Weckhuysen, *Chem. Soc. Rev.* **2015**, *44*, 7342–7370.

[22] A. Lesage, M. Lelli, D. Gajan, M. A. Caporini, V. Vitzthum, P. Miéville, J. Alauzun, A. Roussey, C. Thieuleux, A. Mehdi, et al., *J. Am. Chem. Soc.* **2010**, *132*, 15459–15461.

[23] G. Mathies, M. A. Caporini, V. K. Michaelis, Y. Liu, K. N. Hu, D. Mance, J. L. Zweier, M. Rosay, M. Baldus, R. G. Griffin, *Angew. Chemie - Int. Ed.* **2015**, *54*, 11770–11774.

[24] J. Stanek, L. B. Andreas, K. Jaudzems, D. Cala, D. Lalli, A. Bertarello, T. Schubeis, I. Akopjana, S. Kotelovica, K. Tars, et al., *Angew. Chemie Int. Ed.* **2016**, *55*, 15504–15509.

[25] S. Penzel, A. A. Smith, V. Agarwal, A. Hunkeler, M.-L. Org, A. Samoson, A. Böckmann, M. Ernst, B. H. Meier, *J. Biomol. NMR* **2015**, *63*, 165–186.

[26] A. Böckmann, M. Ernst, B. H. Meier, *J. Magn. Reson.* **2015**, *253*, 71–79.

[27] T. V. Can, Q. Z. Ni, R. G. Griffin, *J. Magn. Reson.* **2015**, *253*, 23–35.

[28] T. V. Can, J. J. Walish, T. M. Swager, R. G. Griffin, *J. Chem. Phys.* **2015**, *143*, 054201.

Samenvatting en perspectieven

In **hoofdstuk 2** werd aangetoond hoe goed spectra met spectroscopische informatie over de zijketen kan worden verkregen met ^{1}H-detectie in combinatie met fast MAS[1]. Een gebruikelijke voorwaarden voor ^{1}H-gedetecteerde experimenten met fast MAS is dat het noodzakelijk is om het ^{1}H-niveau in een eiwit te verminderen om zo de sterke ^{1}H-dipolaire-koppelingen te verzwakken. Daarom worden deze type experimenten meestal uitgevoerd door het eitwit volledig te deutereren en vervolgens weer te laten uitwisselen in aanwezigheid van geprotoneerd water waardoor alleen H^{N}-signalen aanwezig zullen zijn en gaat informatie over de zijketen verloren [2,3]. Een alternatieve strategie die wordt beschreven in dit hoofdstuk wijzigt het kweekmedium dat kan leiden tot verschillende hoeveelheden opname van deuterium in de aminozuren van een eiwit. In dit hoofdstuk wordt getoond hoe deze methode genaamd fractionele deuterering is toegepast voor het detecteren van spectra die vergelijkbaar is met volledig deutereren in termen van resolutie voor eiwitten, maar waarbij protonen van zijketens aanwezig zijn, die eveneens worden benut in de experimenten.

In **hoofdstuk 3** is inzicht verkregen in het cross effect mechanisme dat gebruikt wordt voor DNP. Met DNP is het mogelijk om de gevoeligheid te verhogen. Met MAS is het dusver heersende mechanisme bij dit proces het cross effect dat gebruik maakt van biradicalen [4-7]. Wanneer het magnetische veld toeneemt, neemt de signaal versterking af en volgens een trend van $1/ B_0^2$ [8-10]. Er was geen verklaarbare reden voor deze trend. Daarom voerden we simulaties uit met een methode vergelijkbaar als Mentink-Vigier en co-auteurs in Liouville-space [7,11,12]. Onze resultaten waren consistent met eerder werk en we onderzochten specifiek de oorzaak van de sterke afname van de DNP-efficiëntie wanneer het magneetveld wordt verhoogd. Voor onze simulaties werden er relaxatieparameters bepaald met hoog-veld EPR 275 GHz van de biradicaal en concentraties die gebruikt worden in onze DNP-experimenten. De combinatie van deze parameters met de simulaties bleek dat zwakke hyperfine interacties tussen een elektron en proton de belangrijkste reden zijn voor de waargenomen veldafhankelijkheid. De signaalversterking met DNP is afhankelijk van Level Anti Crossings (LACs) [7,11,12] die het mogelijk maakt verschillende energietoestanden met elkaar te mengen wat uiteindelijk leidt tot de waargenomen signaal versterking. Als het magnetische veld wordt verhoogd leidt dit tot minder efficiënte mengomstandigheden bij deze LACs waardoor de signaalversterking begint af te nemen. Wanneer verschillende hyperfine koppelingen in de simulaties werden

gesimuleerd werd aangetoond dat er een sterke veldafhankelijkheid is van deze interactie. Bij sterke hyperfine koppelingen werd gesimuleerd dat de signaalversterking vrijwel niet leek af te nemen wanneer het magnetisch veld toenam. Echter, wanneer zwakkere interacties gesimuleerd werden bleek dat dit beter in lijn was met de experimenteel waargenomen signaalversterking. Dus bij het DNP-mechanisme zijn het niet de "core" kernen die voor de algehele signaalversterking zorgen, maar de kernen die op een grotere afstand van het radicaal zijn. De “core” kernen worden wel gepolariseerd, maar zijn niet betrokken bij het spin-diffusie proces dat het gehele sample polariseert. De aanwezigheid van deze diffusiebarrière werd experimenteel aangetoond door de groep Pruski middels verschillende gedeutereerde versies van het radicaal [13].

DNP is experimenteel breed toepasbaar, zoals in **hoofdstuk 4** te zien is, door een toepasselijke voorbereiding van het sample kunnen verschillende systemen met deze techniek worden onderzocht. Allereerst kijkend naar intacte diatom biosilica [14] die bestaat uit verschillende moleculaire lagen daarbij was het mogelijk om de aminozuren te identificeren en hun conformatie te bepalen in intacte samples. Verder kon door het combineren van de gemeten signaalversterking met de klassieke diffusie wetten [15] de dikte van elke laag bepaald worden. Met het gebruik van dergelijke data is het mogelijk om een supramoleculaire model van dit systeem samen te stellen. Andere onderzochte systemen waren T4SScc [16] en EGFR [17], waarbij in beide gevallen een combinatie van selectieve aminozuur-isotopen en multi-dimensionale (2D en 3D) het mogelijk maakt met ssNMR deze “probes” te gebruiken om zulke grote systemen te bestuderen en veranderingen te observeren als gevolg van binding van een ligand bij EGFR. Tenslotte werd het potentieel van het gebruik van plaat gerichte spin-labels afgebeeld [18,19], waardoor het gebruik van volledig gedeutereerd oplosmiddel [20] mogelijk wordt zodat de polarisatie niet meer weg kan lekken naar het oplosmiddel in plaats van het eiwit, waardoor in dit geval een signaalverbeteringen van $\varepsilon = 200$ te verkrijgen was met een 14kDa eiwit.

In **hoofdstuk 5** werd DNP toegepast op een katalysator, namelijk Fluid Catalytic Cracking (FCC) [21]. FCC wordt gebruikt in olieraffinaderijen voor de productie van brandstoffen zoals benzine en petrochemische grondstoffen zoals propyleen. Daarbij worden koolstofdeeltjes afgezet op de FCC-deeltjes waardoor de katalysator deactiveert. Via DNP werd aangetoond dat het mogelijk was van deze deeltjes (met een grootte tussen 38-76μm is) een signaal te

verkrijgen dat bevestigt dat koolstofdeeltjes voornamelijk op het oppervlak [22] van de katalysator zitten. Uit een vergelijking van de resultaten verkregen met conventionele en DNP NMR-metingen met verschillende geprepareerde samples bleek dat er overgens ook alifatische koolstofsoorten aanwezig zijn binnen in het deeltje. Deze resultaten tonen het voordeel van DNP voor in-situ solid-state NMR-studies van materialen waardoor afgezette koolstofsoorten kunnen worden gedetecteerd waardoor informatie te verkrijgen is omtrent de lokalisatie van deze koolstofsoorten.

Tenslotte wordt in **hoofdstuk 6** de ontwikkeling van nieuwe radicalen voor hoog-veld DNP besproken. Typisch met de DNP neemt de signaalversterking af als het magnetische veld wordt verhoogd met binitroxides zoals AMUPol [6] of TOTAPOL [4]. Bij het testen van nieuwe radicalen, bestaande uit een Trityl die een relatieve scherpe lijn in het EPR-spectrum geeft en een nitroxide die een veel breder EPR spectrum geeft werd een gunstiger veld afhankelijkheid waargenomen [23]. Deze trityl-nitroxide biradicalen hebben een aanzienlijke J-koppeling die kan worden gemodificeerd door verandering van de linker tussen de radicalen. Wanneer deze worden gemeten bij relatief lage-veld (211 MHz) zijn hun prestaties lager dan de hiervoor genoemde binitroxides. Maar als het magnetische veld wordt verhoogd neemt de signaalversterking eerst toe voordat deze weer uit afzwakt. De toename van de signaalversterking is van bijzonder belang aangezien NMR-metingen bij voorkeur uitgevoerd worden in hoge magneetvelden waardoor de resolutie wordt verbeterd. Uit de combinatie van parameters verkregen van EPR-metingen met simulaties bleek dat met name de J-koppeling belangrijk is en dat de maximale versterking verkregen bij elk veld een andere J-koppeling vereist. Deze observatie kan worden toegeschreven aan de overeenkomstige voorwaarden voor cross-effect DNP [7].

Naarmate het mogelijk wordt samples steeds sneller te spinnen wordt [24-26] de spectrale resolutie met volledig geprotoneerde eiwitten vergelijkbaar met wat nu gebruikt wordt met de verschillende deuterering strategieën. Ook is er een afname van vereiste samplehoeveelheid. Dit maakt niet alleen het verkrijgen van betere spectra mogelijk, maar ook het verkrijgen van zijketen informatie die noodzakelijk is voor het maken van toewijzingen en verkrijgen van contacten tussen de kernen, wat belangrijk is voor structuurberekeningen. Afgezien van het onderzoeken van biomoleculen kan dit mogelijk ook interessante toepassingen hebben voor

materialen bij het onderzoeken van quadrupoolkernen, omdat het zou leiden tot een betere middeling van de tweede orde quadrupool-koppeling.

Voor DNP zal verdere ontwikkeling van radicalen een belangrijke factor zijn zoals de introductie van nieuwe biradicalen voor cross-effect DNP met interessante afhankelijkheid van het aangelegde magnetische veld.
Afgezien van het cross-effect mechanisme zijn er ook verrassende resultaten verkregen met een alternatief mechanisme, namelijk Overhauser DNP. Met dit mechanisme werd een toename in signaalversterking verkregen naarmate het magnetisch veld werd verhoogd [27]. Maar met dit mechanisme zijn tot nu toe geen sterkere signaalverbeteringen verkregen ten opzichte van cross effect DNP op 800 MHz met behulp van binitroxides. Een ander probleem met DNP zijn de lage temperaturen die in het bijzonder voor eiwit monsters kan leiden tot een brede ssNMR signalen die spectrale analyse bemoeilijken. Potentiële ontwikkeling van een puls-microgolfbron kan een manier zijn om niet meer naar lage temperaturen te moeten [28]. Tot nu toe is dit alleen toegepast op lage velden 0.35T. Bij deze lage magnetische velden was een aanzienlijke signaalversterking verkregen (> 100), zelfs bij kamertemperatuur en dit mechanisme zou veldonafhankelijk moeten zijn en zou dus belangrijk zijn voor het verkrijgen van hoge-resolutie spectra van eiwitten. Hiervoor zou echter een (hoogvermogen) gepulste microgolfbron bij hoge frequenties ontwikkeld moeten worden.

Referenties

[1] D. Mance, T. Sinnige, M. Kaplan, S. Narasimhan, M. Daniëls, K. Houben, M. Baldus, M. Weingarth, *Angew. Chemie - Int. Ed.* **2015**, *54*, 15799–15803.

[2] R. Linser, M. Dasari, M. Hiller, V. Higman, U. Fink, J.-M. Lopez del Amo, S. Markovic, L. Handel, B. Kessler, P. Schmieder, et al., *Angew. Chemie Int. Ed.* **2011**, *50*, 4508–4512.

[3] V. Chevelkov, K. Rehbein, A. Diehl, B. Reif, *Angew. Chemie Int. Ed.* **2006**, *45*, 3878–3881.

[4] C. Song, K.-N. Hu, C.-G. Joo, T. M. Swager, R. G. Griffin, *J. Am. Chem. Soc.* **2006**, *128*, 11385–90.

[5] Y. Matsuki, T. Maly, O. Ouari, H. Karoui, F. Le Moigne, E. Rizzato, S. Lyubenova, J. Herzfeld, T. Prisner, P. Tordo, et al., *Angew. Chemie - Int. Ed.* **2009**, *48*, 4996–5000.

[6] C. Sauvée, M. Rosay, G. Casano, F. Aussenac, R. T. Weber, O. Ouari, P. Tordo, *Angew. Chemie Int. Ed.* **2013**, *52*, 10858–10861.

[7] K. R. Thurber, R. Tycko, *J. Chem. Phys.* **2012**, *137*, 1–14.

[8] E. J. Koers, E. a W. van der Cruijsen, M. Rosay, M. Weingarth, C. Prokofyev, Alexander Sauvée, O. Ouari, O. Pongs, P. Tordo, W. E. Maas, M. Baldus, *J. Biomol NMR* **2014**, *60*, 157–168.

[9] M. Kaplan, C. Pinto, K. Houben, M. Baldus, *Q. Rev. Biophys.* **2016**, *49*, DOI 10.1017/S003358351600010X.

[10] M. Kaplan, A. Cukkemane, G. C. P. van Zundert, S. Narasimhan, M. Daniëls, D. Mance, G. Waksman, A. M. J. J. Bonvin, R. Fronzes, G. E. Folkers, et al., *Nat. Methods* **2015**, *12*, 5–9.

[11] D. Mance, P. Gast, M. Huber, M. Baldus, K. L. Ivanov, *J. Chem. Phys.* **2015**, *142*, 234201.

[12] F. Mentink-Vigier, Ü. Akbey, Y. Hovav, S. Vega, H. Oschkinat, A. Feintuch, *J. Magn. Reson.* **2012**, *224*, 13–21.

[13] F. A. Perras, R. R. Reinig, I. I. Slowing, A. D. Sadow, M. Pruski, *Phys. Chem. Chem. Phys.* **2016**, *18*, 65–9.

[14] A. Jantschke, E. Koers, D. Mance, M. Weingarth, E. Brunner, M. Baldus, *Angew. Chemie - Int. Ed.* **2015**, *54*, 15069–15073.

[15] P. C. A. Van Der Wel, K.-N. Hu, J. Z. Lewandowski, R. G. Griffin, *J. Am. Chem. Soc.*

2006, *128*, 10840–10846.

[16] M. Kaplan, A. Cukkemane, G. C. P. van Zundert, S. Narasimhan, M. Daniëls, D. Mance, G. Waksman, A. M. J. J. Bonvin, R. Fronzes, G. E. Folkers, et al., *Nat. Methods* **2015**, *12*, 649–652.

[17] M. Kaplan, S. Narasimhan, C. de Heus, D. Mance, S. van Doorn, K. Houben, D. Popov-Čeleketić, R. Damman, E. A. Katrukha, P. Jain, et al., *Cell* **2016**, *167*, 1241–1251.e11.

[18] B. J. Wylie, B. G. Dzikovski, S. Pawsey, M. Caporini, M. Rosay, J. H. Freed, A. E. McDermott, *J. Biomol. NMR* **2015**, *61*, 361–7.

[19] E. A. W. van der Cruijsen, E. J. Koers, C. Sauvée, R. E. Hulse, M. Weingarth, O. Ouari, E. Perozo, P. Tordo, M. Baldus, *Chem. - A Eur. J.* **2015**, *21*, 12971–12977.

[20] T. Viennet, A. Viegas, A. Kuepper, S. Arens, V. Gelev, O. Petrov, T. N. Grossmann, H. Heise, M. Etzkorn, *Angew. Chemie - Int. Ed.* **2016**, *55*, 10746–10750.

[21] E. T. C. Vogt, B. M. Weckhuysen, *Chem. Soc. Rev.* **2015**, *44*, 7342–7370.

[22] A. Lesage, M. Lelli, D. Gajan, M. A. Caporini, V. Vitzthum, P. Miéville, J. Alauzun, A. Roussey, C. Thieuleux, A. Mehdi, et al., *J. Am. Chem. Soc.* **2010**, *132*, 15459–15461.

[23] G. Mathies, M. A. Caporini, V. K. Michaelis, Y. Liu, K. N. Hu, D. Mance, J. L. Zweier, M. Rosay, M. Baldus, R. G. Griffin, *Angew. Chemie - Int. Ed.* **2015**, *54*, 11770–11774.

[24] J. Stanek, L. B. Andreas, K. Jaudzems, D. Cala, D. Lalli, A. Bertarello, T. Schubeis, I. Akopjana, S. Kotelovica, K. Tars, et al., *Angew. Chemie Int. Ed.* **2016**, *55*, 15504–15509.

[25] S. Penzel, A. A. Smith, V. Agarwal, A. Hunkeler, M.-L. Org, A. Samoson, A. Böckmann, M. Ernst, B. H. Meier, *J. Biomol. NMR* **2015**, *63*, 165–186.

[26] A. Böckmann, M. Ernst, B. H. Meier, *J. Magn. Reson.* **2015**, *253*, 71–79.

[27] T. V. Can, Q. Z. Ni, R. G. Griffin, *J. Magn. Reson.* **2015**, *253*, 23–35.

[28] T. V. Can, J. J. Walish, T. M. Swager, R. G. Griffin, *J. Chem. Phys.* **2015**, *143*, 054201.

List of publications

[1] **D. Mance**, J. van der Zwan, M. E. Z. Velthoen, F. Meirer, B. M. Weckhuysen, M. Baldus and E. T. C. Vogt, "A DNP-supported Solid-state NMR Study of Carbon Species in Fluid Catalytic Cracking Catalysts," *Chem. Commun.*, vol. 53, no. 28, pp. 3933–3936, 2017.

[2] **D. Mance,** M. Weingarth, and M. Baldus, "Solid-State NMR on Complex Biomolecules: Methods and Applications," in *Modern Magnetic Resonance*, Cham: Springer International Publishing, 2016, pp. 1–17.

[3] M. Pellach, S. Mondal, K. Harlos, **D. Mance**, M. Baldus, E. Gazit, and L. J. W. Shimon, "A two- tailed phosphopeptide crystallises to form a lamellar structure," *Angew. Chemie Int. Ed.*, accepted, Jan. 2017.

[4] P. Gast, **D. Mance**, E. Zurlo, K. L. Ivanov, M. Baldus, and M. Huber, "A tailored multi-frequency EPR approach to accurately determine the magnetic resonance parameters of dynamic nuclear polarization agents: application to AMUPol," *Phys. Chem. Chem. Phys*. Jan. 2017

[5] M. Kaplan, S. Narasimhan, C. de Heus, **D. Mance**, S. van Doorn, K. Houben, D. Popov-Čeleketić, R. Damman, E. A. Katrukha, P. Jain, W. J. C. Geerts, A. J. R. Heck, G. E. Folkers, L. C. Kapitein, S. Lemeer, P. M. P. van Bergen en Henegouwen, and M. Baldus, "EGFR Dynamics Change during Activation in Native Membranes as Revealed by NMR," *Cell*, vol. 167, no. 5, pp. 1241–1251.e11, 2016.

[6] J. Medeiros-Silva, **D. Mance**, M. Daniëls, S. Jekhmane, K. Houben, M. Baldus, and M. Weingarth, "^{1} H-Detected Solid-State NMR Studies of Water-Inaccessible Proteins In Vitro and In Situ," *Angew. Chemie Int. Ed.*, vol. 55, no. 43, pp. 13606–13610, Oct. 2016.

[7] P. Fricke, **D. Mance**, V. Chevelkov, K. Giller, S. Becker, M. Baldus, and A. Lange, "High resolution observed in 800MHz DNP spectra of extremely rigid type III secretion needles," *J. Biomol. NMR*, vol. 65, no. 3–4, pp. 121–126, Jun. 2016.

[8] **D. Mance**, T. Sinnige, M. Kaplan, S. Narasimhan, M. Daniëls, K. Houben, M. Baldus, and M. Weingarth, "An Efficient Labelling Approach to Harness Backbone and Side-Chain Protons in 1H-Detected Solid-State NMR Spectroscopy," *Angew. Chemie - Int. Ed.*, vol. 54, no. 52, pp. 15799–15803, Dec. 2015.

[9] A. Jantschke, E. Koers, **D. Mance**, M. Weingarth, E. Brunner, and M. Baldus, "Insight into the Supramolecular Architecture of Intact Diatom Biosilica from DNP-Supported Solid-State NMR Spectroscopy," *Angew. Chemie - Int. Ed.*, vol. 54, no. 50, pp. 15069–15073, Dec. 2015.

[10] G. Mathies, M. A. Caporini, V. K. Michaelis, Y. Liu, K. N. Hu, **D. Mance**, J. L. Zweier, M. Rosay, M. Baldus, and R. G. Griffin, "Efficient Dynamic Nuclear Polarization at 800 MHz/527 GHz with Trityl-Nitroxide Biradicals," *Angew. Chemie - Int. Ed.*, vol. 54, no. 40, pp. 11770–11774, Sep. 2015.

[11] **D. Mance**, P. Gast, M. Huber, M. Baldus, and K. L. Ivanov, "The magnetic field dependence of cross-effect dynamic nuclear polarization under magic angle spinning," *J. Chem. Phys.*, vol. 142, no. 23, p. 234201, Jun. 2015.

[12] M. Kaplan, A. Cukkemane, G. C. P. van Zundert, S. Narasimhan, M. Daniëls, **D. Mance**, G. Waksman, A. M. J. J. Bonvin, R. Fronzes, G. E. Folkers, and M. Baldus, "Probing a cell-embedded megadalton protein complex by DNP-supported solid-state NMR," *Nat. Methods*, vol. 12, no. 7, pp. 5–9, Jul. 2015.

[13] F. B. Gebretsadik, **D. Mance**, M. Baldus, P. Salagre, and Y. Cesteros, "Microwave synthesis of delaminated acid saponites using quaternary ammonium salt or polymer as template. Study of pH influence," *Appl. Clay Sci.*, vol. 114, pp. 20–30, 2015.

Acknowledgements

Firstly, I would like to express my gratitude to my supervisor Marc Baldus for giving me the opportunity to do my PhD in his group and for his enthusiasm and discussions during the work I was involved in. Being able to have been involved in such a variety of topics has made the past 4 years very interesting.

Besides my supervisor, I would like to thank Alexandre Bonvin for the nice discussions and allowing me to make use of the cluster, which never led to any issues. With that I would also like to thank Rolf Boelens and Rob Kaptein, for the interesting discussions about EPR and NMR theory. I would also like to express my gratitude to Eelco Vogt, one of the most enthusiastic and motivating persons I met with who I was able to experience research on catalysts.

Markus, it was always nice talking and working with you, thank you for all your help throughout these years and always making time. Klaartje, Gert and Hans thank you for the interesting discussions and comments.

Mark, thank you for the nice conversations, perhaps a bit unexpected how much we ended up discussing about the DNP experiments throughout the years.

Cecilia, it was a pleasure to have worked with you on the BAM project, during which we had plenty of fun discussions and thank you for your help and enthusiasm. Now on to the people I shared the office with: Sid, it was nice sharing the office with you and the many discussions and coffees we had, it was a pleasant time working with you. Ivan, it was nice having shared the office with you, I wish you all the best with your PhD. João, Miranda, Jon and Reinier thank you for being nice colleagues with who it was possible to have pleasant conversations and "borrels" on Friday.

Johan, thank you for the fantastic technical support. It was interesting being able to talk to you about technical and scientific related issues.

Barbara, thank you for all your help and support throughout these years, especially during the period I was finishing my PhD.

Those that I met in my final year, Shengqi and Meaghan thank you for the nice time and fun discussions, I wish you the best of luck. Alessandra all the best with taking over the DNP projects, I am sure everything will work out well.

To the members from the computational group: Li, Panos, Cunliang, Adrien, Anna, Zeynep, Jeaphianne, Jörg, and Mikael, thank you for a pleasant time and for the nice atmosphere in the

lab. Apart of the people in Utrecht, Kostya and Guoqing thank you for all your help; it was very nice working with you. Also thanks to the previous members of the group with who I had some overlap: Eline, Tessa, Mohammed, Lindsay, Elwin, Abishek, Guido, João and Maryam, I wish you all the best. Finally, I would want to thank my family for their support and encouraging me with their best wishes.

Curriculum Vitae

Deni Mance was born December 17, 1986 in Rotterdam, the Netherlands. He did his Bachelor (HLO) of Chemistry at the Hogeschool Rotterdam. Afterwards he went to Leiden to obtain his Masters in Chemistry in 2012, Main field of study: Theoretical and Physical Chemistry, at the Leiden University. His Masters graduation project was done under the supervision of Prof. Dr. Jörg Matysik at the Leiden University and was titled "^{15}N-Photo-CIDNP MAS NMR studies of heliobacteria". After graduating he worked as a PhD student in the solid-state NMR Group of Prof. Dr. Marc Baldus at the Bijvoet Center for Biomolecular Research at Utrecht University until July 2017. In the NMR Spectroscopy Research Group, he focused on developing methods for sensitivity enhanced solid-state NMR approaches and applying them to (bio)molecular systems.